Progress in Materials Science 137 (2023) 101131

Contents lists available at ScienceDirect

Progress in Materials Science

journal homepage: www.elsevier.com/locate/pmatsci

Seventy years of Hall-Petch, ninety years of superplasticity and a generalized approach to the effect of grain size on flow stress

Roberto B. Figueiredo [a,*], Megumi Kawasaki [b], Terence G. Langdon [c]

[a] Department of Metallurgical and Materials Engineering, Universidade Federal de Minas Gerais, Belo Horizonte, MG 31270-901, Brazil
[b] School of Mechanical, Industrial and Manufacturing Engineering, Oregon State University, Corvallis, OR 97331, USA
[c] Materials Research Group, Department of Mechanical Engineering, University of Southampton, Southampton SO17 1BJ, UK

ARTICLE INFO

Keywords:
Deformation mechanisms
Grain boundary sliding
Hall-Petch
Mechanical properties
Superplasticity

ABSTRACT

The grain size, and therefore the grain boundary density, is known to play a major role in the flow stress of metallic materials. A linear relationship to the inverse of the square root of the grain size was identified about 70 years ago giving rise to the well-established Hall-Petch grain refinement strengthening effect. Nevertheless, grain refinement softening is known to take place at high homologous temperatures and both effects have been given separate treatments. A recent model showed that a general relationship can explain both the Hall-Petch strengthening effect at low temperatures and superplasticity at high temperatures. The present review discusses recent advances in structural and mechanical characterization to provide an updated analysis of trends observed in the relationship between the grain size and the flow stress. The model of grain boundary sliding is evaluated using multiple sets of data in the literature and a general description is provided for the transition between grain refinement hardening and grain refinement softening. The analysis incorporate data from over 30 different metals and alloys with different grain sizes and after testing at different strain rates and temperatures. Data from molecular dynamic simulations are also included and show supporting evidence to the model of grain boundary sliding. The thermal contribution of the grain size strengthening and threshold

Abbreviations: *A*, constant for creep mechanism,; *b*, Burgers vector; *bcc*, body centered cubic; *BM*, ball milling; *D*, diffusion coefficient,; *d*, grain size; $D_{0,gb}$, pre-exponential for grain boundary diffusion; D_{gb}, grain boundary diffusion coefficient; D_l, lattice diffusion coefficient; d_l, linear intercept grain size; d_s, spatial grain size; *EBSD*, electron back scattered diffraction; ECAP, equal-channel angular pressing; *fcc*, face centered cubic; *G*, shear modulus; *GBS*, grain boundary sliding; *GND*, geometrical necessary dislocations; *h*, climb distance for dislocation; *hcp*, hexagonal close-packed; *HPT*, high-pressure torsion; *IGC*, inert gas condensation; *k*, Boltzmann's constant; *K*, Hall-Petch constant; K^l_{GBS}, Hall-Petch slope estimated from the GBS model considering linear intercept grain size; K^s_{GBS}, Hall-Petch slope estimated from the GBS model considering spatial grain size; *L*, length of a pile-up; $\bar{L}$, linear intercept length; *m*, strain rate sensitivity; *M*, Taylor factor; M_S, Sachs orientation factor; *MD*, molecular dynamics; *MS*, magnetron sputtering; *n*, stress exponent on creep equation; *p*, inverse grain size exponent on creep equation; Q_{gb}, activation energy for grain boundary diffusion; *R*, gas constant.; *SPD*, severe plastic deformation; *T*, absolute temperature; *TEM*, transmission electron microscopy; T_m, melting temperature; v_c, dislocation climb velocity; *XRD*, X ray diffraction; α, constant; β, function of the Poisson coefficient; ΔE, activation energy; $\Delta E(\sigma)$, activation energy which is a function of the applied stress; $\Delta L/L_0$, elongation in tension; δ, grain boundary width; ε, plastic deformation; $\dot{\varepsilon}$, deformation rate; $\dot{\varepsilon}_{Coble}$, Coble creep rate; $\dot{\varepsilon}_{NH}$, Nabarro-Herring creep rate; $\dot{\varepsilon_0}$, reference strain rate; ω, fitting parameter in the composite model; σ, flow stress; σ_0, single crystal flow stress; σ^*_0, zero temperature flow stress; σ_B, flow stress of the bulk in the core and mantle composite model; σ_{GB}, flow stress of the grain boundary in the core and mantle composite model; σ_p, stress at the tip of a dislocation pile-up; τ, shear stress acting on the slip plane; τ_c, shear stress on a locked dislocation at the tip of the pile-up.

* Corresponding author.
E-mail address: figueiredo@demet.ufmg.br (R.B. Figueiredo).

https://doi.org/10.1016/j.pmatsci.2023.101131
Received 2 December 2022; Received in revised form 7 April 2023; Accepted 13 April 2023
Available online 20 April 2023

stress is discussed including the trends observed in the strain rate sensitivity of fine-grained materials.

1. Introduction

The flow stress, or the stress at which metallic materials flow and display permanent deformation, is a key parameter in the evaluation of their mechanical behavior and it is a subject of great interest in any attempt to understand the role played by structural features within the materials. A common research procedure includes assessing the flow stress of pure metal single crystals with low densities of crystalline defects and then assessing the effect of defects such as impurities, dislocations, second phase particles and grain boundaries. These studies also generally include estimates of the effects of temperature and strain rate.

The influence of each crystalline defect, such as the type and amount of impurity atoms in solid solution, the dislocation density and size and the morphology and amount of second phase particles, are relatively well predicted and there are accepted phenomenological explanations for these predictions. However, an understanding of the effect of grain boundaries on the flow stress is less well developed. The main parameter associated with the grain boundaries may be the polycrystalline average grain size which provides the density of grain boundaries in the material. It is not easy to estimate the precise origins of research on this topic but major breakthroughs took place in the early 50s, about seventy years ago.

1.1. The Hall-Petch relationship or *"low temperature grain refinement hardening"*

Hall [1] published a paper in 1951 on the deformation of mild steels and made the following statement:

> "*It is known that if a dislocation in a matrix approaches a region, such as a grain-boundary film, which has a higher yield stress than the matrix itself, then this region constitutes an effective potential barrier for the passage of the dislocation, In other words, the dislocation will experience a repulsion near the grain boundary interface, and dislocations will pile up along the glide plane behind the grain boundary film, until the stress concentrations around the tip of the slip band cause the film to yield. Deformation is then transferred to the next grain*" [1].

Hall then suggested that the difference between the flow stress of a polycrystal, σ, and the flow stress of a single crystal, σ_0, is proportional to the inverse of the square root of the grain size, *d*, such that [1]

$$(\sigma - \sigma_0) \propto 1/d^{1/2} \tag{1}$$

This relationship was further expanded in 1953 by Petch [2] to account for the cleavage strength of polycrystals and Petch also introduced the assumption of a Frank-Read source in the center of a grain as in the following extract:

> "*The dislocations initially present within the crystal can probably begin to move at small stresses, lower than the conventional yield point, but they cannot pass beyond the confines of the grain boundary. On the glide planes that contain a Frank-Read source, there will be dislocation multiplication, and this will continue until the accumulation of the dislocations on the glide plane and the interaction between the dislocations within the accumulation stop the multiplication for that particular applied stress*" [2].

Petch suggested a quantitative explanation to the contribution of grain size to the cleavage strength, reported experimental data of the flow stress in agreement with Hall and then presented an equation that relates the flow stress and the grain size in the format which has become widely established within the materials science community:

$$\sigma = \sigma_0 + Kd^{-1/2} \tag{2}$$

where *K* is a constant which later became known as the Hall-Petch constant.

Thereafter, it has become common practice to plot experimental data of flow stress as a function of the inverse of the square root of the grain size and it is found that this relation is valid for most, if not all, metals, at least over a range of reasonable grain sizes. However, the original explanation for the relationship was based on the concept of dislocations emitted from a Frank-Read source in the center of a grain piling-up at the nearest grain boundary and activating slip in the neighboring grain and this does not agree with a broad set of data for many materials. Also, different slopes have been reported in the plots of σ vs $d^{-1/2}$ for different grain size ranges in different materials. Accordingly, many different mechanisms have been suggested to address these issues but to date there has been no acceptable prevailing model.

The lack of consensus on this topic appears to have various reasons but a detailed discussion on this topic is outside of the scope of this review. Nevertheless, it is important to note that a control of the grain size for experimental analysis may be more complicated than simply controlling the impurities, dislocation density and presence of second phase particles. Any production of samples with a broad range of grain sizes is not an easy task and the early studies on this subject made use of samples in which the minimum grain sizes were in the range of a few micrometers. The inherent limitation on grain refinement is of particular importance since the rule is based on the assumption that the flow stress is inversely proportional to the square root of the grain size and this means that large flow stresses, which are required for any accurate evaluation of trends, depend upon the presence of very small grain sizes. Therefore, it is reasonable to anticipate that the lower bound for grain size in these earlier studies will almost certainly affect the overall accuracy of

the predictions. Although there is the occasional early report of the production of nanocrystalline materials, such as a grain size of 12 nm in nickel in 1986 [3], the extent of available data for bulk samples having ultrafine grains has only increased significantly over the last two decades. This is illustrated in Fig. 1 where data for the flow stress, σ, of aluminum is plotted as a function of the inverse of the square root of the grain size, $d^{-1/2}$. These data were collected from multiple sources [4–25] and the data from papers published in the last century are highlighted. It is readily apparent that the range of grain sizes in experiments will play a significant role in determining the accuracy of any trend. Thus, early studies reported values for the Hall-Petch constant, K, in the range of 10 ~ 65 MPa $\mu m^{1/2}$ [26] whereas data reported in this century show this constant, as estimated from the slope of the plot in Fig. 1, is probably larger than ~ 100 MPa $\mu m^{1/2}$. In fact, there may be two stages in the σ vs $d^{-1/2}$ plots for aluminum so that coarse-grained samples display a lower slope and finer grains display a larger slope.

The development of methods to produce nanocrystalline materials led to a significant step forward in this research but the early experiments were limited to very small samples which may also contain other defects. As a consequence, there was a great deal of dispersion in both the data and the trends. It is only very recently that methods were developed to increase the size and homogeneity of samples with very small grain sizes, thereby providing the possibility of accurately evaluating the trends.

1.2. *High temperature grain refinement softening and "the inverse Hall-Petch behavior"*

If the low temperature grain refinement hardening predicted by Eq. (2) is widely known and accepted, it is also widely accepted that the opposite trend takes place at high temperatures. This means that smaller grain sizes produce lower flow stresses at high temperatures. At this point it is important to clarify that the notion of "high" temperature is not absolute and depends on the melting point of the material. In the interests of simplicity, the present work considers "low" temperatures as $T < 0.3\ T_m$, "moderate" temperatures as $0.3\ T_m < T < 0.5\ T_m$ and "high" temperatures as $T > 0.5\ T_m$, where T_m is the absolute melting temperature of the material.

High temperature mechanical behavior is usually described by using creep mechanisms for which there are well-established rate-controlling equations. The general creep equation can be written in the form [27].

$$\dot{\varepsilon} = \frac{ADGb}{kT}\left(\frac{\sigma}{G}\right)^n\left(\frac{b}{d}\right)^p \tag{3}$$

where $\dot{\varepsilon}$ is the deformation rate, A is a constant, D is the relevant diffusion coefficient, G is the shear modulus, b is the Burgers vector, k is the Boltzmann's constant, T is the absolute temperature and p and n are constants. The type of diffusion coefficient and the constants A, n and p vary depending on the creep mechanism. Although Eq. (3) is mostly considered in any analysis of high temperature deformation, for conditions of steady-state deformation a similar equation has been suggested [28] to explain the low temperature deformation of ultrafine grained (UFG) metals which do not display work-hardening and also deform under steady-state conditions. The suggested equation considered $n = 8$ and $p = -4$ which in practice predicts a Hall-Petch relationship. Some creep mechanisms such as dislocation viscous glide or dislocation climb occur intragranularly so that the exponent p is equal to zero and therefore the grain size has no effect on the creep rate or flow stress. But other mechanisms, such as Coble diffusion creep [29] and Nabarro-Herring diffusion creep [30,31] and grain boundary sliding [32], occur intergranularly and have a positive exponent p which means that, for constant temperature and strain rate, the flow stress decreases with decreasing grain size.

For example, the strain rate for superplasticity, which is controlled by grain boundary sliding, may be estimated from the relationship [33]

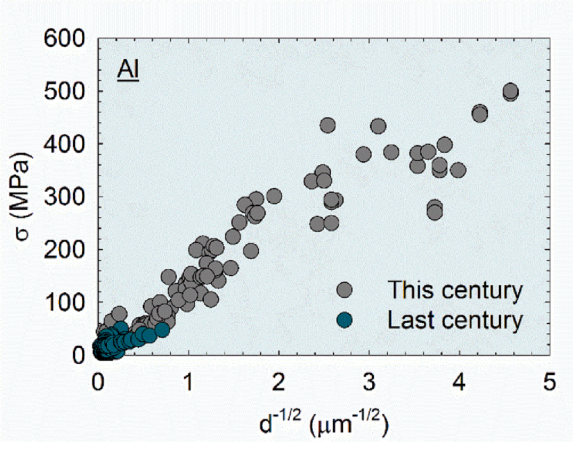

Fig. 1. Flow stress of aluminum [4–25] plotted as a function of the inverse of the square root of the grain size. The data reported in the last century are highlighted.

$$\dot{\varepsilon} = \frac{A\delta D_{gb} G}{kT}\left(\frac{\sigma}{G}\right)^2\left(\frac{b}{d}\right)^2 \tag{4}$$

where A is a constant equal to ~ 5, δ is the grain boundary width which is usually taken as $2b$ and D_{gb} is the coefficient for grain boundary diffusion. This equation can be rearranged to separate the flow stress and the grain size so that

$$\sigma\left(\frac{A\delta D_{gb}}{\dot{\varepsilon} G k T}\right)^{1/2} = \frac{d}{b} \tag{5}$$

The validity of this relationship is illustrated in Fig. 2 which shows the flow stress normalized by the strain rate and temperature plotted as a function of the grain size normalized by the Burgers vector for a magnesium alloy AZ31 for which there are multiple reports in the literature [34–43] on superplasticity and grain boundary sliding. It is apparent that the stress increases linearly with increasing grain size and the data agree fairly well with the prediction.

The first paper reporting a true superplastic behavior was published almost ninety years ago in 1934 [44]. The understanding of the deformation mechanism during superplasticity was developed later but it is now well established that grain boundary sliding is the rate-controlling mechanism [45]. Thus, the trends reported for low temperature flow (Hall-Petch) and for high temperature superplasticity are contrary and this is illustrated in Fig. 3 in which the flow stress and the grain size are plotted in arbitrary units using a logarithmic scale. At low temperatures the flow stress is proportional to $d^{-1/2}$ and at high temperatures the flow stress in fine-grained samples is proportional to d under conditions in which the material undergoes superplasticity.

It is interesting to note that the different mechanisms that were proposed [33,46,47] to explain high temperature grain boundary sliding consider the existence of dislocation pile-ups within the grains. Both Hall [1] and Petch [2] also considered the existence of dislocation pile-ups and made reference to a paper that had been recently published in 1951 on the equilibrium of linear arrays of dislocations [48]. Hall suggested that the pile-up would generate deformation in the neighboring grain and Petch suggested the pile-up could initiate fracture. Ball and Hutchison [46] attributed to Friedel [49] a suggestion that the climb of dislocations into and along grain boundaries could be caused by the concentrated stress at the head of dislocation pile-ups. Thus, both the low and the high temperature behavior of metals may be directly affected by dislocation pile-ups.

Although it may seem intuitively contradictory that similar assumptions will generate opposite trends in the relationship between flow stress and grain size, a recent report showed that a mechanism suggested for grain boundary sliding can explain both trends using a single rate-controlling equation based on the material fundamental properties and without the incorporation of any adjustable parameters [50]. By further developing this approach, the present review critically examines some models that were developed to explain the Hall-Petch behavior such as the structural features observed during the room temperature deformation of fine-grained samples and the overall dispersion in experimental data. This approach provides qualitative and quantitative analyses of the model of grain boundary sliding based on a large set of data from the literature and the results demonstrate that a single model can indeed predict both the low and high temperature effect of grain size on the flow stress for multiple sets of experimental conditions.

2. Background of the "Hall-Petch" relationship

It is important to note that the papers by Hall [1] and Petch [2] in the early 50 s are still widely cited in analyses of the relationship between grain size and flow stress. Since then, it is common to see the flow stress plotted as a function of the inverse of the square root of the grain size to display a linear trend for the data. Early reports [51–54] gave values of σ_0 and K based on experimental data for different metals and then discussed the phenomenology behind the various relationships. More recent reviews [55–58] incorporate

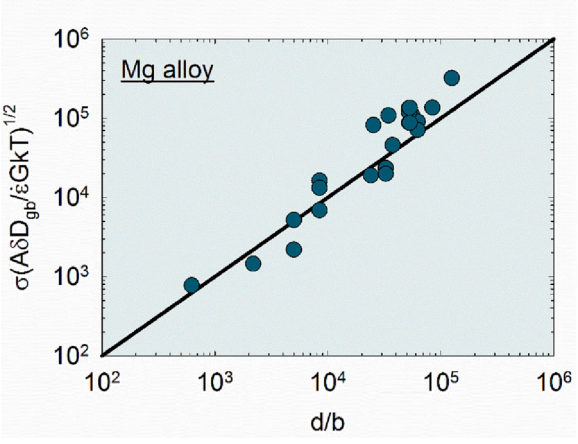

Fig. 2. Flow stress normalized by the strain rate and temperature plotted as a function of the grain size normalized by the Burgers vector. Data for magnesium alloy AZ31 taken from the literature [34–43].

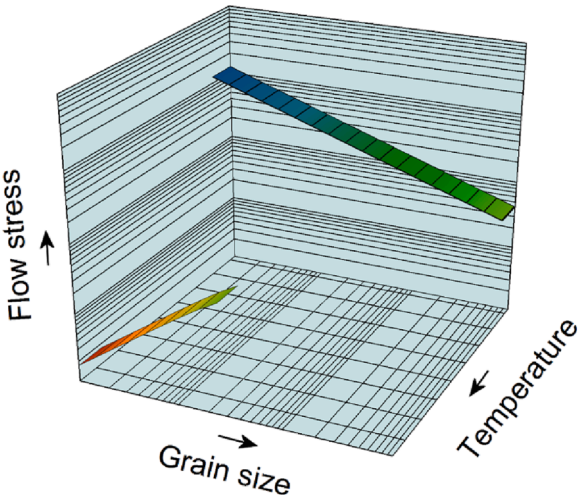

Fig. 3. Illustration of the different trends observed at low and at high temperatures between the flow stress and grain size.

data for true nanocrystalline materials and therefore they examine more extensive sets of results. Moreover, other properties such as the ductile to brittle transition, fatigue, fracture mechanics and strain rate sensitivity also display dependences on the inverse of the square root of the grain size [57]. It was recently suggested that even the corrosion rate may follow a similar dependence [59].

The relationship between the flow stress and the inverse of the square root of the grain size was initially attributed to dislocation pile-ups at grain boundaries which would activate slip across the boundary. The length of the pile-up was considered proportional to the grain size and therefore the smaller the grain size so the shorter the pile-up and therefore the lower the stress at its head. The stress required to activate slip across the grain boundary was considered constant which means that for smaller grain sizes a larger external stress was required to activate slip. Following this approach, and considering the stress required to activate slip across the grain boundary as a fraction of the shear modulus, it is possible to estimate the slope K in Eq. (2) and then reach the following relationship [60]:

$$\sigma = \sigma_0 + \alpha G\sqrt{b}/\sqrt{d} \tag{6}$$

where α may attain a value of ~ 0.1 [60]. It is possible to reach a similar relationship, with different value for α, considering an alternative theory in which the grain boundaries act as sources of dislocations [60]. An early report showed that the Hall-Petch effect can also hold after the beginning of plastic deformation. Thus, a constant slope between flow stress and the inverse of the grain size can be obtained after straining for materials displaying a yield point behavior or not [51].

Many theories were suggested over the years and they were described and critically reviewed elsewhere [55,56]. These theories are sometimes divided into groups based on their basic mechanisms such as dislocation pile up, work-hardening and composite models. Although the basic mechanisms in these models differ, they usually consider, at least for a range of grain sizes, a linear relationship between the flow stress and the inverse of the square root of the grain size so that this is in agreement with the original Hall-Petch data.

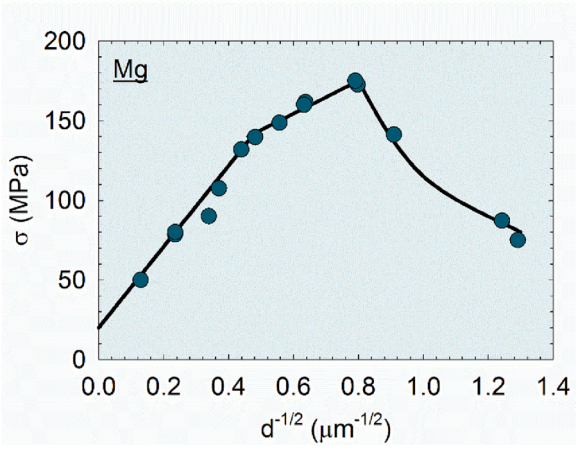

Fig. 4. Flow stress of pure magnesium plotted as a function of the inverse of the square root of the grain size. Data taken from the literature [64,66].

The next section discusses some of these models but it is important to point out that the continuous linearity in σ vs $d^{-1/2}$ plots has been questioned by experiments in recent decades.

The more recent ability to produce samples with smaller grain sizes has provided the opportunity to expand the σ vs $d^{-1/2}$ plots. Thus, while the continuous linear trend between flow stress and the inverse of the square root of the grain size was confirmed up to the nanometer range for some materials such as iron [61], different trends were observed at different grain size ranges for other materials and there are many reports of a decrease in the Hall-Petch slope in nanocrystalline materials [62]. For example, it is now known that magnesium and its alloys display a specific slope for the coarse-grained range and a lower slope in the fine and ultrafine-grained range [63–67]. The larger slope in the coarse-grained range is attributed to twinning-controlled deformation while the lower slope at finer grains is attributed to slip-controlled deformation [67,68]. Also, a decrease in the flow stress with decreasing grain size is observed at very small grain sizes. These different slopes are shown in Fig. 4 in which experimental data for pure magnesium [64,66], including samples with grain sizes smaller than 1 μm, are plotted as a function of $d^{-1/2}$. Thus, a higher slope is observed up to $d^{-1/2}$ of ~ 0.4 and this is followed by a reduced slope and then a negative slope at $d^{-1/2}$ larger than ~ 0.8.

The decrease in flow stress with decreasing grain size is also known as the inverse Hall-Petch effect or grain refinement softening. It is widely accepted that this effect takes place during high temperature deformation but it was also reported at room temperature in nanocrystalline materials. A recent review discusses this topic [56]. Although there is some doubt concerning the existence of the inverse Hall-Petch effect since defects introduced during sample preparation may interfere with the mechanical testing, there are now large numbers of reports of this effect. A summary of experimental data on the flow stress of nanocrystalline materials and a critical examination of different models for the deformation mechanism of these materials and the inverse Hall-Petch effect is available elsewhere [69].

It is important to note that, in addition to the reports for nanocrystalline materials, the inverse Hall-Petch effect is widely considered to take place at room temperature in materials having low melting points. For example, grain refinement softening was reported in Zn in 1969 [70]. Recent reports also show grain refinement softening in other materials such as high purity Al [71], Mg [63,64], Mg-Li [72], Al-Zn [73], Pb-Sn [74] and Bi-Sn [75] alloys. Thus, it is apparent that thermally-activated mechanisms, which should be enhanced in low melting point materials, play a major role in the relationship between flow stress and grain size. This will be further discussed in the next sections.

2.1. Some models for the "Hall-Petch" effect

As noted earlier, a model for the Hall-Petch effect based on dislocation pile-ups may predict that the slope between σ and $d^{-1/2}$ is given by $\alpha G b^{1/2}$. The value of the constant α depends on assumptions regarding the deformation and it is possible to reach a value of ~ 0.1 [60]. Nevertheless, this relationship does not agree with the experimental data for multiple materials. Comparisons between the experimental values of K and $\alpha G b^{1/2}$ suggest that the values of the constant α may vary by up to one order of magnitude [55].

Different dislocation pile-up models have been suggested and account for some of the disagreement with the experimental data. For example, different Hall-Petch slopes are predicted when considering concentric circular dislocation loops [76]. The Hall-Petch slope may also be affected by the number of slip systems and dislocation locking in different materials [51]. For instance, the Hall-Petch slope can be estimated using the following equation (7) on the basis of dislocation pile-ups [77]:

$$K_{disl.\ pile-up} = M\left(\frac{\pi M_S G b \tau_c}{2\beta}\right)^{1/2} \tag{7}$$

where M is the Taylor factor, M_S is the Sachs orientation factor, τ_c is the shear stress on a locked dislocation at the tip of the pile-up and β is a function of the Poisson coefficient with a value of ~ 0.8. Good agreement between the prediction from Eq. (7) and experimental data was reported in nanocrystalline Al, Cu and Ni [77].

Other models were developed to explain the Hall-Petch effect based on the effect of grain size on the dislocation density and work-hardening, including a model based on the non-homogeneous deformation of materials [78]. This model considers gradients in the plastic deformation of metals caused by the microstructure. Specifically, it considers that geometrically-necessary dislocations (GND) are created to maintain deformation compatibility and the density of these dislocations contribute to the strength of the material. The relationship between the flow stress and the grain size for this mechanism is then given by [78]:

$$\sigma = \sigma_0 + CG\sqrt{b\varepsilon/d} \tag{8}$$

where C is a constant and ε is the amount of plastic deformation. It follows that the slope in the σ vs $d^{-1/2}$ plots is then given by $CG(b\varepsilon)^{1/2}$ which means that it will increase with increasing plastic strain. Other models [79–81] also consider that the grain size affects the dislocation density and the flow stress. Many studies evaluate the changes in slope between σ and $d^{-1/2}$ with increasing strain and a recent review [55] showed that some of these studies reveal an increase in slope as predicted by Eq. (8) so that this model is the most consistent with observations of dislocation structure in deformed coarse-grained polycrystals. It is worth noting that most of the studies which reported an increase in the Hall-Petch slope K with increasing strain were based on coarse-grained samples that display strain hardening behavior. It is now well known that ultrafine and nanocrystalline materials display negligible strain hardening. Accordingly, this will affect the validity of Eq. (8) as now examined.

A rule of thumb to estimate the minimum grain size at which the material continues to display strain hardening is to place it equal to the size of the stable sub-grain size. The stable sub-grain size, λ, is a function of the applied stress and the following relationship in

Eq. (9) is valid for a broad range of materials including metals, ceramics and geological materials [27,82–84]:

$$\frac{\lambda}{b} = \zeta\left(\frac{G}{\sigma}\right) \tag{9}$$

where ζ is a constant equal to ~ 20. Thus, it is necessary to estimate the relationship between the flow stress and the grain size in order to determine the minimum grain size at which strain hardening behavior is expected. The flow stress of pure aluminum predicted by a recent model and validated by experimental data [50] and the predictions of the stable sub-grain size from Eq. (9) for pure aluminum are shown in Fig. 5a. The intersection between the curves reveals that a grain size of ~ 0.8 μm is equal to the sub-grain size in aluminum at room temperature so that strain hardening is expected for grains larger than this value and steady-state deformation is expected for smaller grains. Thus, the stress vs strain curves obtained in tensile tests for pure aluminum with different grain sizes [14] are shown in Fig. 5b for comparison. It is readily apparent that samples with grain sizes smaller than 0.8 μm do not display any hardening while samples with coarser grain structures display strain hardening and this is in agreement with the assumption that no hardening is expected when the grain size is smaller than the sub-grain size.

A direct consequence of this lack of strain hardening in ultrafine and nanocrystalline materials is that there is a fundamental disagreement with the model of non-homogeneous deformation of materials [78] as given by Eq. (8) which predicts an increase in slope with increasing strain. As the increase in strain increases the flow stress of coarse-grained materials but does not affect the flow stress of ultrafine-grained materials, the slope in the σ vs $d^{-1/2}$ plots can only decrease with increasing strain if a broad range of grain sizes is considered.

It is now well established that the linearity of the relationship between the flow stress and the inverse of the square root of the grain size is not constant for many materials over a broad range of grain sizes. Thus, the variations in the slope can be treated as a consequence of different deformation mechanisms [85,86]. The change in slope has also been attributed to a decrease in the number of dislocations in the pile-up with decreasing grain size [87].

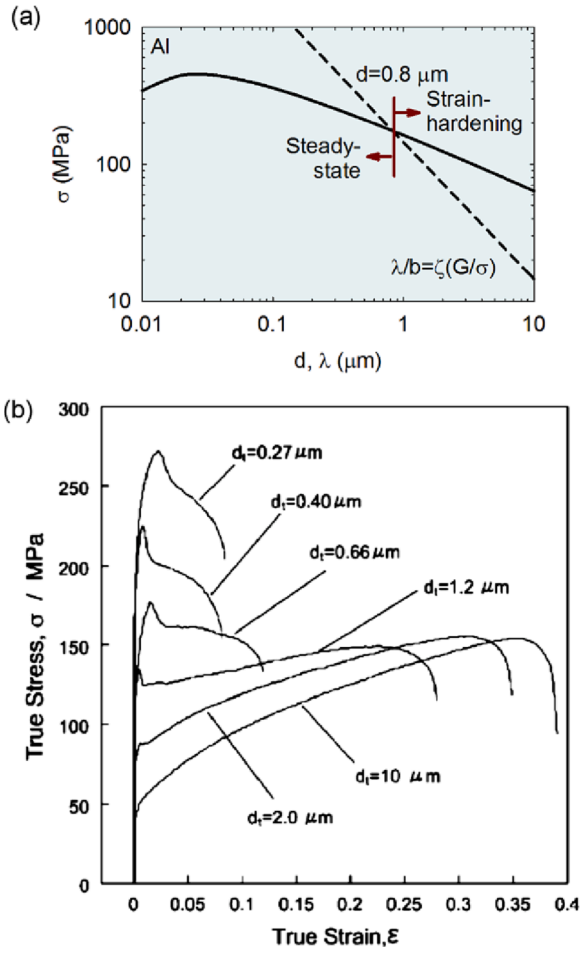

Fig. 5. (a) Flow stress for pure aluminum predicted by the model [50] plotted as a function of the grain size together with the predicted relation between applied stress and subgrain size and (b) experimental stress strain curves for pure aluminum with different grain sizes [14].

There are also some models that consider the structure as a composite in which the grain boundary region displays a different behavior than the grain interior [81,88–90] and these models predict a decrease in slope in the fine grain region as a consequence of the increase in volume fraction of the grain boundary phase. One of the models [81] considers that elastic stress incompatibilities between different grains raise the stresses in the vicinity of the grain boundaries and thereby generate dislocations. The dislocation density becomes larger near the grain boundaries and this increases the flow stress in these regions. The material behaves as a composite in which the bulk material has a flow stress of σ_B and the grain boundaries have a flow stress equal to σ_{GB} ($\sigma_{GB} > \sigma_B$). Considering the fraction of the grain boundary volume is proportional to $d^{1/2}$ it is possible to reach the following relationship for the polycrystalline flow stress:

$$\sigma = \sigma_B + 8\omega(\sigma_{GB} - \sigma_B)d^{-1/2} - 16\omega^2(\sigma_{GB} - \sigma_B)d^{-1} \tag{10}$$

where ω is an appropriate fitting parameter. Thus, this model predicts a Hall-Petch relationship with the flow stress proportional to $d^{-1/2}$ in the coarse-grained regime and a decrease in slope at very small grain sizes. Theses composite models have shown good

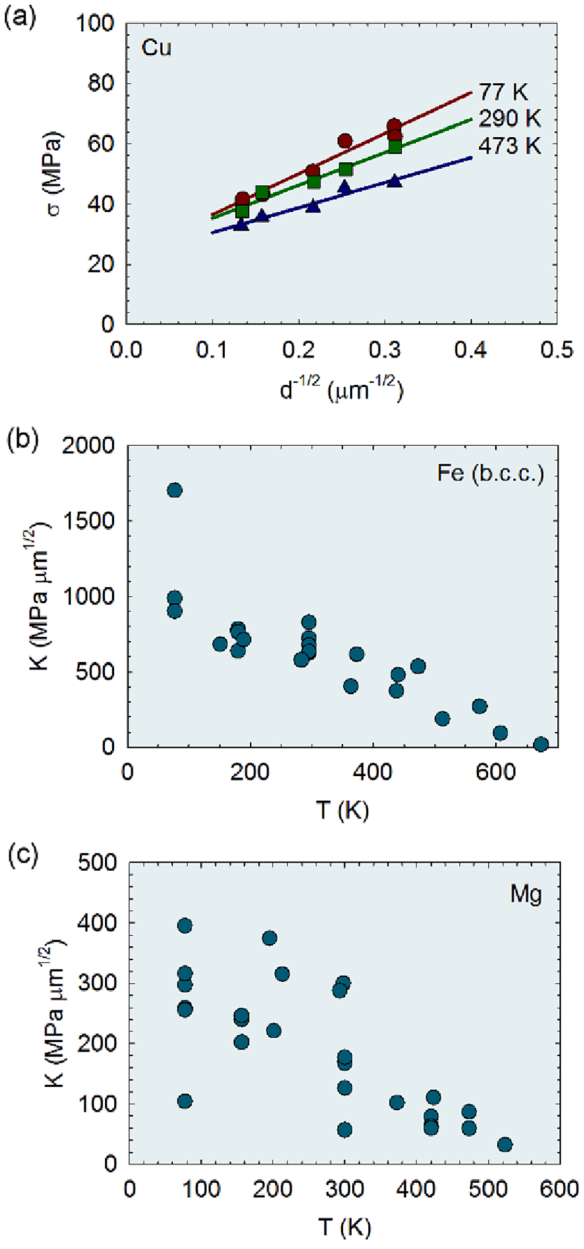

Fig. 6. (a) Flow stress at different temperatures for copper plotted as a function of the inverse of the square root of the grain size (data taken from the literature [95]), Hall-Petch slope *K* plotted as a function of the temperature for (b) Fe [96,98,99,102–104] and (c) Mg [105,109–112].

agreement with experimental results and reviews [56,62] on the Hall-Petch effect, focused on nanocrystalline materials, suggest they provide the best description of the behavior in the grain size range between 100 nm and 1 μm.

2.2. The thermal contribution

It is important to point out that some of the models available in the literature do not consider a thermal contribution to the Hall-Petch slope and this means that the temperature and the strain rate should not affect the trends. Nevertheless, some models consider the thermal contribution. For example, a composite model considers separate effects from the grain interior and the grain boundary volumes where the behavior of the material in the grain boundaries is thermally-activated [88–90]. This assumption enables the model to predict an inverse Hall-Petch effect at very small grain sizes and differences in behavior at different temperatures and strain rates. Three separate grain size regimes were suggested elsewhere [85] and different deformation mechanisms were proposed for each regime including the prediction of grain refinement softening at very small grain sizes. The Hall-Petch slope, as given by Eq. (7) for a dislocation pile-up model, depends on τ_c which is the resistance against dislocation nucleation. It is expected that this parameter will depend on the temperature [77]. These latter models [77,85] show good agreement with the experimental data of activation volumes reported in the literature for ultrafine-grained materials. The storage and annihilation of dislocations at grain boundaries was considered in a different model and compared to data for ultrafine-grained Cu and nanocrystalline Ni [28].

Thermally-activated mechanisms are usually included in analyses of the deformation mechanism of nanocrystalline materials considering that the deformation mechanism changes in these materials. For example, the Coble creep mechanism [29] was considered as the source of grain refinement softening in an early report of this effect [91]. A mechanisms in which the deformation rate is controlled by the absorption of dislocations at grain boundaries was suggested to explain the transition between conventional Hall-Petch behavior in coarse-grained materials and the inverse Hall-Petch effect in their nanocrystalline counterparts [92]. A good fit to the experimental data for the inverse Hall-Petch effect in nanocrystalline materials was observed when considering a model for dislocation-accommodated boundary sliding [93,94].

Experimental evidence is available showing that the temperature affects the behavior of metallic materials not only in the nanocrystalline range but also in coarse-grained samples. The thermal contribution may be small in materials with high melting points and therefore experiments carried out over narrow temperature ranges cannot detect a clear effect. Experiments over wide-ranging temperatures reveal a slight decrease in the slope in σ vs $d^{-1/2}$ plots with increasing temperature in Cu [95], Fe [96–99] and Ti [100,101]. Fig. 6a shows an example of these plots for copper tested at 77 K, 290 K and 473 K where a decrease in slope is evident with increasing temperature [95]. The slopes, K, for iron were estimated from data in the literature [96,98,99,102–104] and are plotted as a function of temperature in Fig. 6b where there is a clear trend of decreasing K with increasing temperature.

The change in slope is more pronounced and more easily revealed in experiments in lower melting point materials such as Al [23], Mg [68,105,106] and Pb [107]. Fig. 6c shows a summary of the slopes reported in the literature for pure magnesium plotted as a function of the testing temperature. A trend of a decrease in the value of K with increasing temperature is also noted. It was also reported that the relationship between flow stress and grain size for magnesium depends on the strain rate [63]. Many authors [98,99,102,105,108] report that the experimental observations of decreasing K with increasing temperature support the dislocation pile-up model with a slope given by Eq. (7)[51]. The thermal contribution in this case is associated with the parameter τ_c which is considered a function of the temperature and strain rate.

One point to note in any analysis of the theories and models for the Hall-Petch effect is that the amount of data, materials and testing conditions considered in the validation process is invariably very limited. In practice, any comparison with a broad range of data from multiple materials is generally difficult due to considerations of parameters other than the material fundamental properties and the grain size. A recent report [113] evaluated different theories and models, including pile-up, work-hardening and composite models, and concluded that the data do not support any of them. This analysis included data fitting and Bayesian *meta*-analysis and the authors questioned the exponent of $-1/2$ in the Hall-Petch model and suggested instead that the general size effect could explain the relationship between grain size and strength.

It is important to remember that the amount of experimental data in studies concerning the effect of grain size on the flow stress is large and diverse. The level of flow stress and the trends vary significantly for the same "material" in isolated studies and this dispersion in data is discussed in a separate section. Thus, the disagreement between a model and sets of data must be considered with care, as well as any apparent agreement. Different trends reported in flow stress vs grain size plots, in different materials and in different testing conditions may be attributed to different deformation mechanisms operating under specific conditions. Therefore any disagreement with an isolated set of experiments should not rule out any model or theory.

A model proposed recently [50], based on the mechanism of grain boundary sliding, attempts to address these deficiencies by considering a thermally-activated mechanism to estimate the flow stress for a broad range of grain sizes and testing conditions and by then providing a large amount of supporting evidence based on results available in the literature. It was later shown that this model provides good agreement with experimental data for 26 pure metals processed by severe plastic deformation (SPD) [114] and for magnesium alloys [67,115]. It was also shown that the model predicts the room temperature relationship between flow stress and grain size for 16 different metals and there is also good agreement with experimental data for the strain rate sensitivity of ultrafine-grained metals [116]. Finally, a recent paper confirmed that the model also predicts, in good agreement with the available experimental data, the flow stress, strain rate sensitivity and apparent activation volume of a multi component high-entropy alloy having different grain sizes, strain rates and temperatures by making use of a description of the thermal contribution of the threshold stress [117]. The next sections describe this mechanism and provide a more comprehensive critical evaluation by considering a broader range of materials and testing conditions.

3. A unified model for the effect of grain size at low and high temperatures based on grain boundary sliding

Grain boundary sliding is widely known to take place during high temperature flow and its direct contribution to the deformation rate depends on the grain size, strain rate and temperature. An early report [33] describes this mechanism and provides the rate equations for situations in which the grain size is either smaller or larger than the stable sub-grain size. It was recently shown that a simplification considered in the early study, which was based on the low stresses and high diffusion rates of high temperature deformation, is not valid for lower temperatures and therefore a different equation, without any simplification, was developed [50]. It was then suggested that the relationship between the flow stress and the grain size can be predicted for a broad range of materials, temperatures and strain rates by essentially considering the model for grain boundary sliding [50].

The phenomenological principles of the model consider that extrinsic dislocations glide at grain boundaries causing grain boundary sliding and building up stresses at triple junctions. These high stresses activate slip in the neighboring grain so that dislocations are emitted from the grain boundary, glide through the grain and pile up at the opposite boundary. The dislocations are then absorbed by the opposite boundary through climb which is assisted by the high stresses developed by the dislocation pile-up. The mechanism is effectively illustrated in Fig. 7.

The stress at the head of the pile up, σ_p, is given by Eq. (11), the climb velocity, v_c, is given by Eq. (12) and the overall sliding rate, $\dot{\varepsilon}$, is then given by Eq. (13) considering the time required for a dislocation to climb a distance h is $t = h/v_c$ and the sliding rate is b/t [50]:

$$\sigma_p \cong \frac{2L\tau^2}{Gb} \tag{11}$$

$$v_c = \frac{D}{h}\left[exp\left(\frac{\sigma_p b^3}{kT}\right) - 1\right] \tag{12}$$

and

$$\dot{\varepsilon} = \frac{bv_c}{\sqrt{3}hd} \tag{13}$$

where L is the length of the pile-up, τ is the shear stress acting on the slip plane, D is the relevant diffusion coefficient which is considered equal to the grain boundary diffusion coefficient, D_{gb}, and d is the spatial grain size. The length of the pile-up and the distance a dislocation climbs depends on the grain size and it was considered that $L \approx \overline{L}$, $h \approx 0.3\,\overline{L}$ and $d \approx 1.7\,\overline{L}$, where $\overline{L}$ is the mean linear intercept grain length. It follows that the grain size affects the deformation in opposing ways. Decreasing the grain size decreases the climb distance and increases the contribution of grain boundary sliding to the overall deformation rate.

These effects are expected to decrease the stress required for flow which contradicts the Hall-Petch relationship. Nevertheless, decreasing the grain size shortens the pile-up length and increases the stress required for flow which is consistent with the Hall-Petch relationship. Thus, the mechanism has the capability of predicting, depending on the precise experimental conditions, either grain refinement hardening or grain refinement softening. A detailed description of the assumptions and an estimation of the rate-controlling mechanism is available elsewhere [50] where the fundamental equation for flow is given as follows:

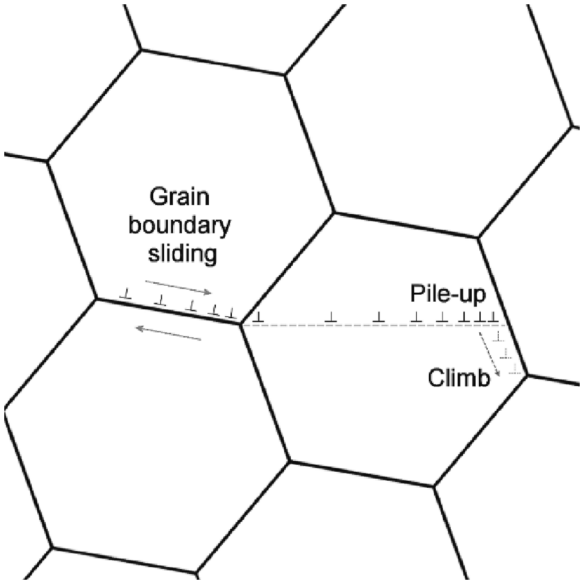

Fig. 7. Illustration of the basic principle of the mechanism of grain boundary sliding [50].

$$\dot{\varepsilon} \approx \frac{10\delta D_{gb}}{d_s^{\,3}}\left[exp\left(\frac{2d_s\sigma^2 b^2}{3GkT}\right)-1\right] \tag{14}$$

where d_s is the spatial grain size. Although the behavior in creep is usually calculated in terms of a rate-controlling mechanism, it is important to isolate the stress, σ, to provide a direct comparison with the low temperature data. Thus, Eq. (15) provides a prediction for the stress which is given by [50]:

$$\sigma \approx \sqrt{\frac{3GkT}{2d_s b^2} ln\left(\frac{\dot{\varepsilon} d_s^{\,3}}{10\delta D_{gb}}+1\right)} \tag{15}$$

Equations (14) and (15) incorporate the spatial grain size which is a usual practice in high temperature analyses. However, many studies consider the mean linear intercept length, d_l, as the grain size in low temperature experiments. It is important to consider this difference and thus Eq. (16) provides an estimate of the flow stress considering the conventional relationship of $d_l = d_s/1.74$ [118]:

$$\sigma \approx \sqrt{\frac{\sqrt{3}GkT}{2d_l b^2} ln\left(\frac{\dot{\varepsilon} d_l^{\,3}}{2\delta D_{gb}}+1\right)} \tag{16}$$

The contribution of the grain size to the flow stress depends on the fundamental properties of the material, such as the values of *G, b* and δD_{gb}, and the precise testing conditions in terms of *T* and $\dot{\varepsilon}$. In practice, the value within the logarithm function, $ln\left(\dot{\varepsilon} d_s^{\,3}/10\delta D_{gb}+1\right)$ in Eq. (15), dictates whether superplasticity or Hall-Petch behavior may be expected and this situation is now examined.

In conditions in which the grain boundary diffusion coefficient is large and the strain rate and grain size are small, the values within the logarithmic function decrease. An approximation of $\ln(x+1) \approx x$ can be made for very small *x* and then Eq. (15) becomes Eq. (4) which is the model for high temperature grain boundary sliding and the flow stress decreases with grain refinement. This condition is often observed in the high temperature testing of fine-grained materials and superplasticity may be observed in these situations.

By contrast, under conditions in which the value within the logarithmic function is large such as with a low grain boundary diffusion coefficient, a high strain rate and/or coarse grain structures, an approximation can be made such that small variations in the grain size are considered to not affect significantly its outcome. This means that under these conditions Eq. (15) and Eq. (16) predict a Hall-Petch type of behavior given by Eq. (2) with the slopes given by the following Eqs. (17) and (18) for a spatial grain size and a linear intercept grain size, respectively. This condition is often observed in the low temperature testing of coarse-grained materials.

$$K_{GBS}^{s} \approx \sqrt{\frac{3GkT}{2b^2} ln\left(\frac{\dot{\varepsilon} d_s^{\,3}}{10\delta D_{gb}}+1\right)} \tag{17}$$

$$K_{GBS}^{l} \approx \sqrt{\frac{\sqrt{3}GkT}{2b^2} ln\left(\frac{\dot{\varepsilon} d_l^{\,3}}{2\delta D_{gb}}+1\right)} \tag{18}$$

It is interesting to note that the grain size remains present within the equation of the slope and this means that the slope depends on the grain size range. A slight decrease in slope is then predicted for ultrafine and nanocrystalline materials compared with their coarse-grained counterparts.

In addition to the mathematical description of these distinct regimes, it is important to discuss the phenomenology behind the low- and high-temperature deformation. The mechanism of grain boundary sliding is based on the assumption that the climb of dislocations at the tip of the pile-up plays a significant role in controlling the deformation rate. At high temperatures and low strain rates the thermal contribution to vacancy diffusion along grain boundaries is expected to maintain equilibrium in the vacancy concentration. However, with decreasing temperatures and increasing strain rates the thermal contribution cannot sustain the rate of diffusion and the stress then plays an increasing role. The non-conservative climb of jogged dislocations is expected to create a supersaturation of vacancies [50]. In practice, the flow stress increases and the strain rate sensitivity decreases with decreasing temperature and increasing strain rate.

It is important to note that Eqs. (14)–(18) are based on the fundamental properties of the materials and there are no additional adjustable parameters. This demonstrates that the relationship between the flow stress and the grain size should not vary for different crystalline structures but rather it should be similar in pure metals and dilute alloys provided the alloying elements introduce no significant change in the fundamental properties of the pure material. Supporting evidence for the overall effectiveness of the predictions from this model are readily available in the literature [50,114,116,117] and will now be reviewed.

4. Structural features observed during deformation

The mechanism of grain boundary sliding introduced in the previous section involves the assumption of the glide of dislocations unimpeded through the grain towards the opposite grain boundary. This condition is only satisfied in recrystallized samples or in materials having grain sizes smaller than the stable sub-grain size which can be estimated using Eq. (8) in Section 2.1. Dislocation accumulation and dislocation cells may develop in coarse-grained materials during deformation, or twin boundaries may form to impede dislocation movement as was reported in the first experimental investigation of the role of matrix dislocations in superplasticity [119], and this will prevent the dislocations from moving freely throughout the grain interior. Therefore, Eqs. (10) and (11)

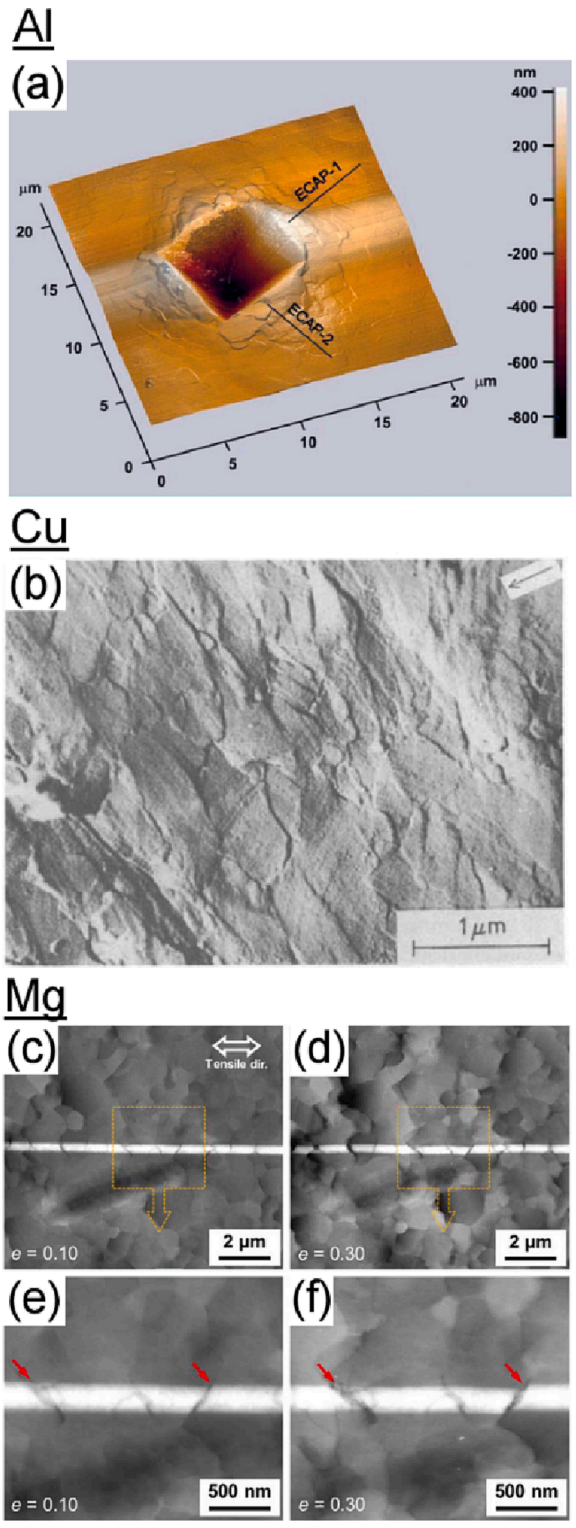

Fig. 8. Examples of grain boundary offsets reported in ultrafine-grainede (a) Al [120], (b) Cu [121] and (c-f) Mg [64] and attributed to grain boundary sliding.

can only predict the initial flow stress of coarse-grained materials but may predict the steady-state flow stress of ultrafine-grained materials. It is therefore important to examine any reports of structural features observed during the deformation of ultrafine and nanocrystalline materials.

It is expected that the grain boundaries undergo a large amount of shearing due to the glide of extrinsic dislocations and this will lead to the formation of surface steps in these regions during deformation. This is a well-known feature observed in samples which undergo high temperature grain boundary sliding. Surface steps along grain boundaries have also been widely reported in ultrafine-grained materials tested at room temperature. Fig. 8 shows examples of grain boundary offsets reported in ultrafine-grained samples of (a) Al subjected to indentation [120], (b) Cu subjected to compression [121] and (c-f) Mg subjected to tensile deformation [64] which were attributed to grain boundary sliding. Other reports are available for pure Mg [63,122] and Mg-8 % Li [72], Mg-0.3 % Bi [123], Mg-0.65 % Mn [124], Al-30 % Zn [73,125] and Bi-42 % Sn [75] alloys.

In addition to the reports of grain boundary offsets, dislocation mediated displacements between grains along grain boundaries was observed during *in situ* straining of nanocrystalline platinum [126]. High-resolution transmission electron microscopy (TEM) images of the same area taken at different stages of deformation revealed grain rotations assisted by dislocation climb along grain boundaries. Fig. 9 shows a sequence of images from one region of the sample at different strain levels. The grains are numbered in Fig. 9b and the angles between the grains 1 and 2, 1 and 3 and 3 and 4 before and after deformation are reported in Fig. 9a and 9f, respectively. It was reported that a decrease in dislocation density between grains 1 and 3 through dislocation climb caused a rotation of the grain and a decrease in the angle between these grains [126].

Another assumption from the model is the emission of dislocations from grain boundaries to accommodate the grain boundary sliding process. This is supported by multiple sources including TEM observations during *in situ* deformation of ultrafine-grained IF steel [127] which revealed a continuous emission of dislocations from grain boundaries. Fig. 10 shows a sequence of images in which the dislocation source is identified as "2R" in Fig. 10a and it was reported there were multiple dislocations emitted from the same

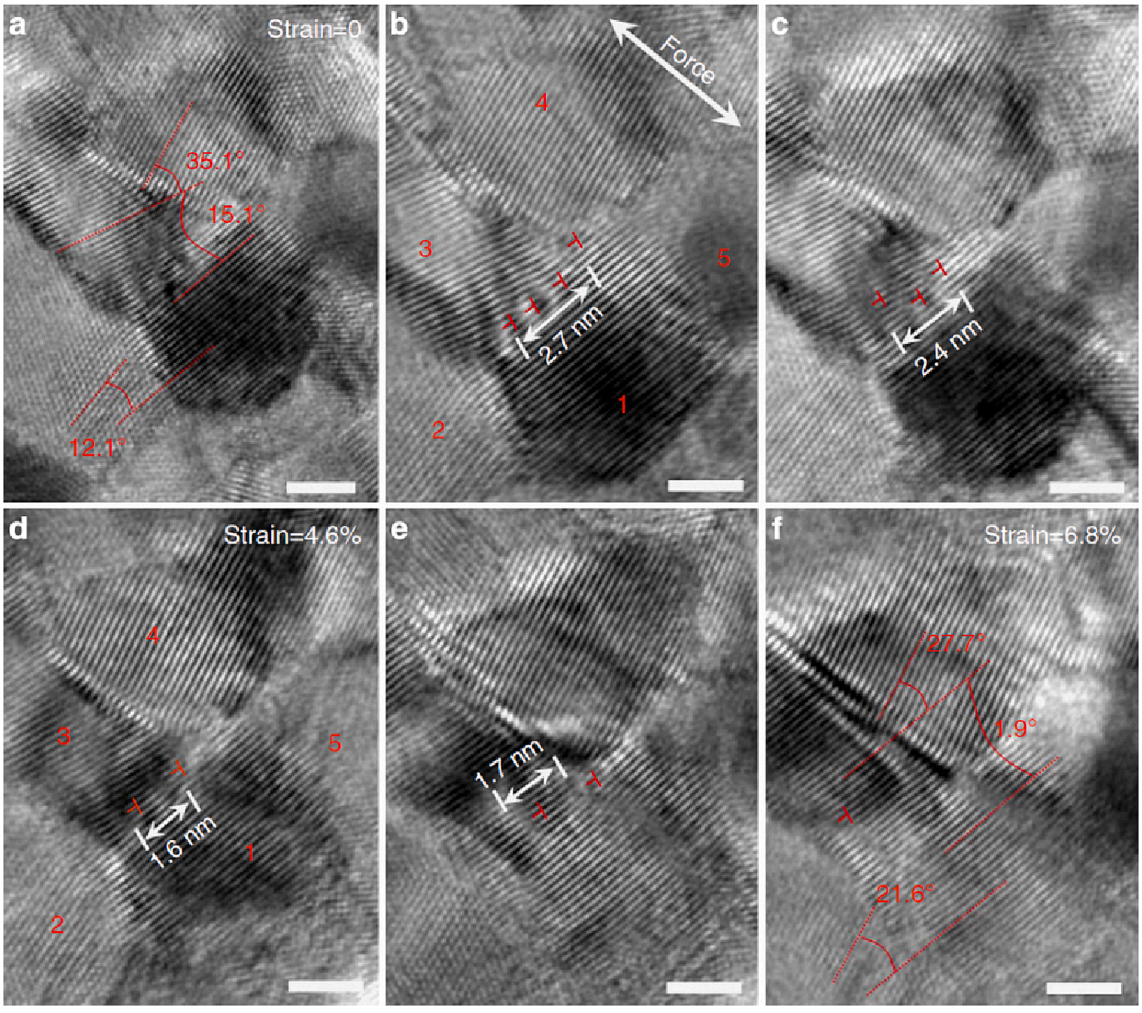

Fig. 9. High resolution TEM images of the same area at different strain levels during *in situ* deformation. The grains are numbered in (b) and the angles between some of the grains before and after deformation are reported in (a) and (f) respectively. The scale bar is 2 nm [126].

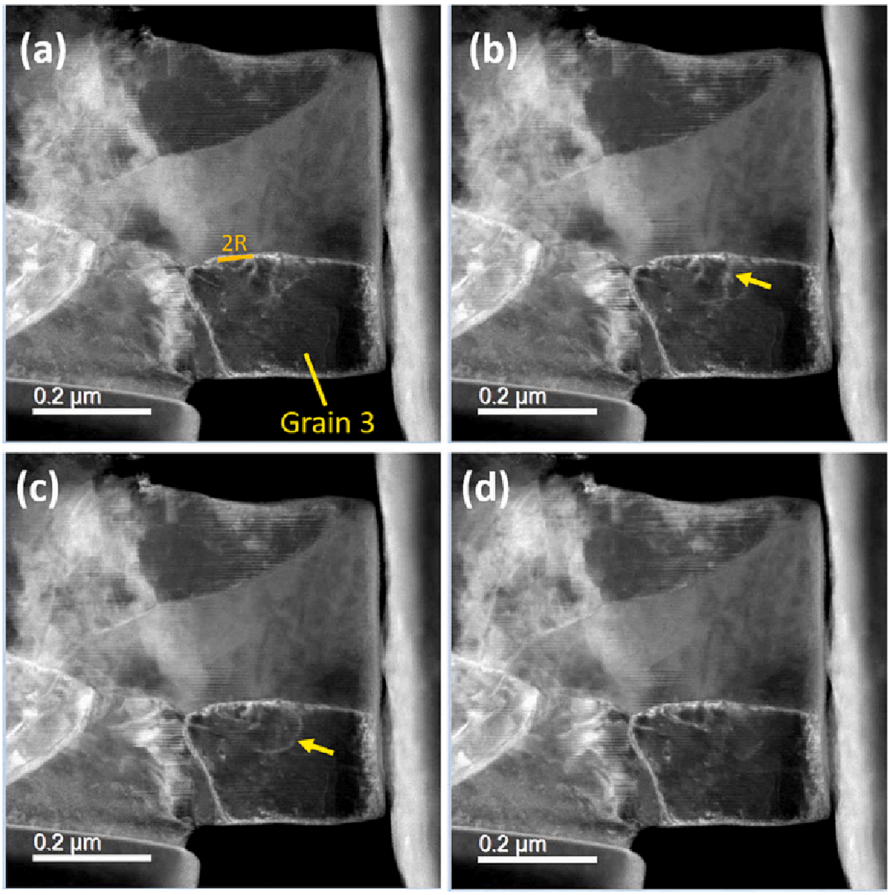

Fig. 10. Sequence of TEM images obtained during *in situ* compression of ultrafine-grained IF steel showing dislocation emission from a grain boundary [127].

source during deformation [127]. Dislocation emission from grain boundaries has been reported also during *in situ* deformation of nanocrystalline copper [128] and nickel [129].

Dislocation pile-ups are widely known features observed in many coarse-grained materials. Nevertheless, there is skepticism concerning whether dislocation pile-ups take place in ultrafine and nanocrystalline materials due to the shorter available length scales in these materials. However, *in situ* deformation of nanocrystalline copper revealed the development of a pile-up in a grain as small as 20 nm [128]. Fig. 11 shows a sequence of images of deformation ahead of a propagating crack and the dislocation pile-up is highlighted using white arrows.

Although the process of dislocation climb is difficult to observe during *in situ* experiments, it was reported during deformation of nanocrystalline platinum and, as shown earlier, played an important role in grain rotation [126]. It is worthwhile noting that the non-conservative climb of jogged dislocations is expected to generate point defects within the crystalline structure of the material. Therefore, the large plastic deformation of ultrafine-grained materials, in which the climb process is active, is expected to produce an enhanced concentration of point defects such as vacancies which will cause an excess volume. In fact, excess free volumes and vacancies have been widely reported in ultrafine-grained materials subjected to processing by SPD [130–135].

This excess of free volume can be estimated directly using dilatometry. The principle of this technique is depicted in Fig. 12a where the variation in length during heating of a specimen of material processed by SPD is illustrated by a continuous line and an undeformed specimen by a dashed line. A deviation is observed in the material processed by SPD in which the rate of length change is reduced at a certain temperature. This effect is attributed to the annealing of an excess volume in the processed material and it is depicted in Fig. 12b where the undeformed sample is illustrated in white while the processed material is illustrated in gray shade. The ultrafine-grained material processed by SPD displays an excess volume which is annealed out at a certain temperature leading to a decrease in the sample length [133]. An example is shown in Fig. 12c for iron processed by high-pressure torsion where the processed material is depicted by a continuous line and an undeformed material is shown as a dashed line. A clear change in volume, attributed to annealing of an excess volume, is observed in the first cycle of heating of the processed material [136]. The occurrence of excess vacancies in ultrafine-grained metals processed by SPD was also confirmed using a positron annihilation technique [137].

Molecular dynamics simulations have been an important tool to understand the deformation mechanism of materials with small grain sizes. Despite the limitations of sample volume and the exceptionally high strain rates of over $\sim 10^8\ s^{-1}$, these studies allow the

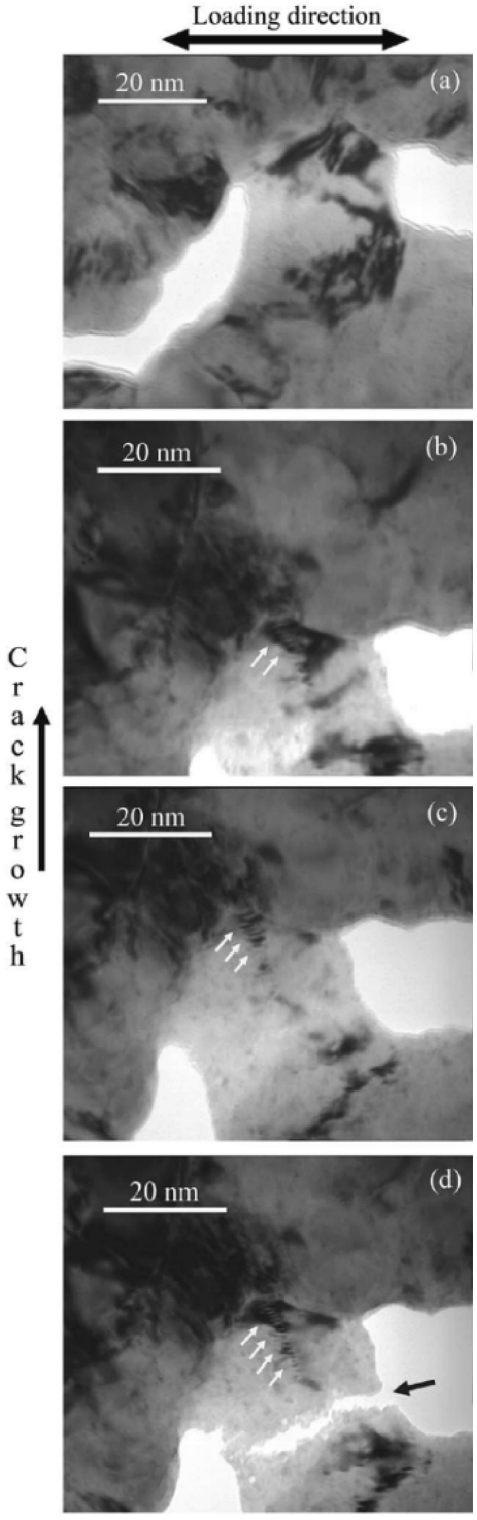

Fig. 11. Evidence for the formation of a dislocation pile-up during *in situ* deformation of nanocrystalline copper [128].

identification, tracking and visualization of various deformation features. There are reports that confirm some of the features which were observed during *in situ* experiments such as the emission of dislocations from grain boundaries [138,139]. Simulations in nanocrystalline aluminum revealed that partial dislocations are emitted from ledges at grain boundaries during deformation and the

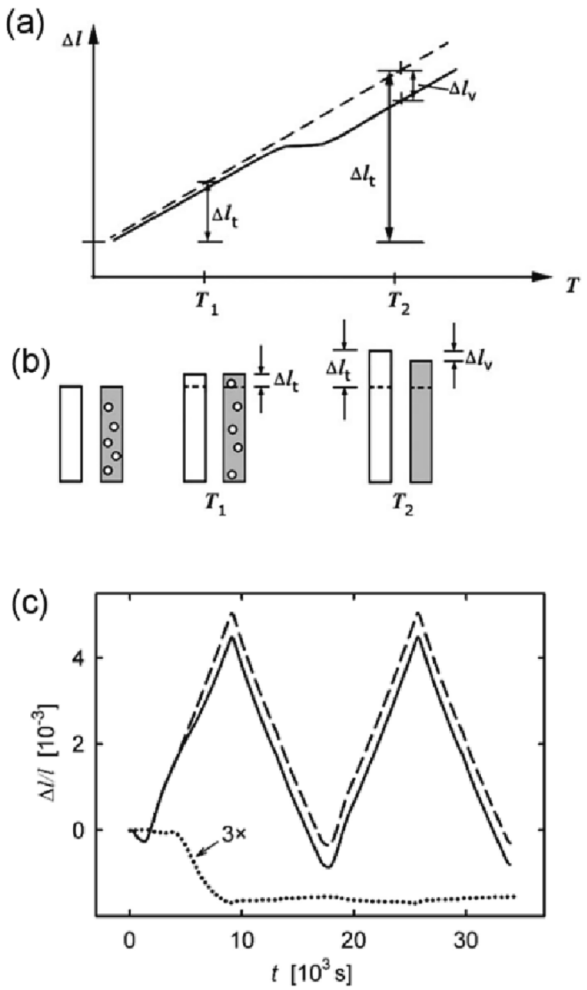

Fig. 12. (a) and (b) Illustration of the principle of the dilatometry technique for the evaluation of annealing of excess volume [133] and (c) an example of an experiment on iron processed by high-pressure torsion [136].

source of the partials can be located in different areas of the grain boundary or even at different grain boundaries [140]. Fig. 13 shows a 3D image of a step in the simulation in which the leading partial dislocation has glided through a significant area and the trailing partial is emitted. The stacking fault between the partials is illustrated with atoms highlighted in red, the source of the leading partial is labeled with "LP" and the source of the trailing partial is labeled with "TP" [140]. The region where these partial dislocations were emitted is close to a grain triple junction so that this image looks similar to the schematic illustration of the grain boundary sliding model as depicted in Fig. 7.

Many of the deformation features suggested by the grain boundary sliding model were also observed during deformation of nanocrystalline copper using molecular dynamics simulations [141]. Thus, simulations were conducted considering samples with different grain sizes ranging from 5 to 50 nm and this revealed a maximum in the flow stress for grains in the range of 10 ~ 15 nm. It follows that, while deformation was mainly concentrated along the grain boundaries in the finest grain size range, dislocation emission from grain boundaries, dislocations pile-ups and dislocations absorbed at grain boundaries were also observed in the coarser grain range [141]. Fig. 14 shows a 3D image of a step during deformation where a dislocation that split into partials is labeled with "A" and pile-ups are labeled with "B" and "C". It was reported that the pile-up labeled "B" is 35 to 40 nm in length and consists of five to six dislocations which is in agreement with the expectations from a stress of 2 GPa [141].

Other interesting observations from molecular dynamics simulation include grain boundary migration [142] and a report of diffusion-assisted creep mechanisms [143]. There are also reports that significant portions of the deformation is accommodated at grain boundaries in nanocrystalline materials [144–146]. In addition, simulations in Cu and Ni [147] in which the grain sizes were in the range of a few nanometers revealed significant deformation along grain boundaries and the emission of partial dislocations from grain boundaries at triple junction. It was concluded that "*Atomic displacement analysis shows that deformation starts at triple points, with GB sliding followed by the creation of intragrain Shockley partial dislocations which glide on slip systems that are not necessarily those favored by the Schmid factor*" [147]. This conclusion is very similar to the description of the mechanism proposed for grain boundary sliding

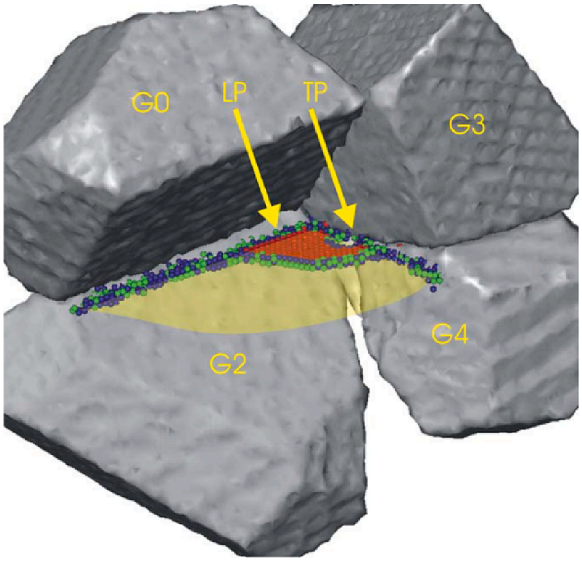

Fig. 13. Three dimensional illustration of the process of partial dislocations being emitted from grain boundaries in a molecular dynamics simulation of the deformation of nanocrystalline aluminum [140].

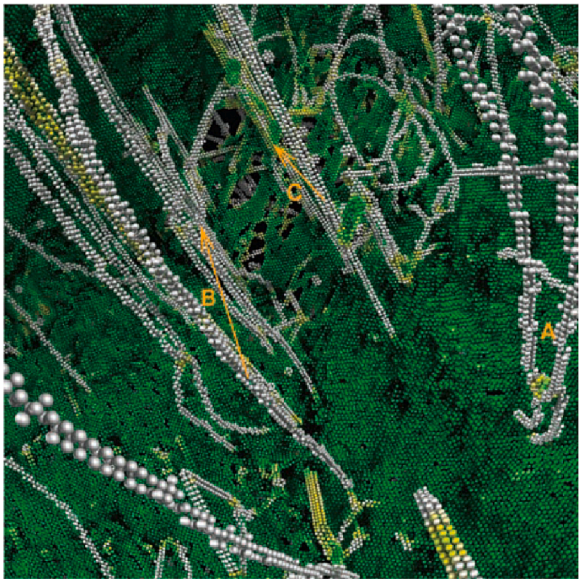

Fig. 14. 3D image of a molecular dynamics simulation of deformation of nanocrystalline copper. The atoms at grain boundaries are darker and the atoms at dislocation cores are lighter. Dislocation pile-ups are labeled "B" and "C" in the image [141].

[50].

Accordingly, it is concluded that *ex situ* and *in situ* experiments and molecular dynamics simulations provide significant supporting evidence for all phenomena that are incorporated into the mechanism for grain boundary sliding [50]. Nevertheless, this does not prevent other mechanisms from operating together with sliding or under specific conditions. Thus, the existence of a rate-controlling mechanism does not prevent other mechanisms from operating but rather it allows an estimation of the strain rate or the flow stress required for the overall deformation. The best procedure for evaluating the effectiveness of a model as the rate-controlling mechanism is therefore to compare its prediction to a broad set of experimental data. This comparison is provided in the following sections but a first critical discussion is needed on the significance of the dispersion in the relevant experimental data. These details are given in the following section.

5. Dispersion in the experimental data

As the numbers of results available in the literature increase, researchers typically try to correlate data for one material obtained from multiple sources. This procedure allows the evaluation of trends for a broader range of grain sizes and testing conditions. It also introduces a spread in the data. One of the difficulties in evaluating the relationship between flow stress and grain size is the disparity between experimental data and the trends reported in isolated studies.

Thus, the method used to produce the samples is one of the main sources of dispersion, particularly for nanocrystalline materials. Fig. 15 shows data for the flow stress plotted as a function of $d^{-1/2}$ for Cu and Cu alloys produced using different methods and each symbol corresponds to a different set of experiments. Following Tabor s rule [148], the values of hardness were divided by 3 to correlate with the flow stress. Different trends are reported in different sets of experiments and in materials produced using different techniques. It is apparent that materials produced using bottom-up techniques (gray symbols in Fig. 15), in which the sample is built from very small pieces and then consolidated as in inert gas condensation (IGC), display lower values of strength. This can be directly attributed to defects that are introduced during the fabrication of these samples such as porosity. Moreover, significant grain coarsening was observed below the tip of an indenter in pure nanocrystalline copper produced by IGC [149]. Grain growth was even more significant at cryogenic temperatures and in samples with higher purity and it was concluded that stress-driven grain growth could invalidate the results of some mechanical tests in nanocrystalline metals [149]. A close inspection of Fig. 15 reveals that one of the sets of experiments depicted in samples produced using the IGC method, where the grain sizes were coarser [150], suggest a higher slope compared to the others. Also, a set of experiments in which impurities were added to copper during ball milling [151] also suggests a higher Hall-Petch slope compared to other bottom-up techniques. These sets are depicted using dark gray symbols.

The data from materials processed using SPD [152] (red symbols in Fig. 15) such as equal-channel angular pressing (ECAP) and high-pressure torsion (HPT) exhibit a higher slope which is in agreement with the higher slope predicted from two set of experiments from samples produced using a bottom-up technique which are depicted using darker gray symbols. These data include the results from tests in bulk samples with recrystallized grain structures covering a wide range of grain sizes [153]. The SPD techniques are known as top-down since the grain refinement is introduced in a bulk sample and therefore porosity is avoided. It is worthwhile noting that the minimum grain size achieved using SPD is significantly smaller than achieved using conventional thermo-mechanical operations but nevertheless it is larger than when using bottom-up techniques. The grain size introduced through SPD can be reduced by the addition of second phase particles [154] and some impurity elements [155] which prevent grain growth during processing. An analysis of the data shows that these defects, which are introduced to pin grain boundaries, do not alter the trends observed in the σ vs $d^{-1/2}$ plots. Finally, it is important to note that the data in Fig. 15 include the results obtained from the consolidation of particles using HPT [154] and these data display a high slope which is similar to that obtained in bulk samples. This suggests that plastic deformation is an effective way to consolidate particles and may reduce the numbers of defects in the finished product. Additional supporting evidence for the effectiveness of plastic deformation in the consolidation of particles is the higher strength, in the range of ~ 1300 MPa, observed in samples produced by the hot extrusion of particles subjected to ball milling [151]. Thus, in order to minimize the dispersion in the collected data it is important to critically examine the method used to produce the samples and to avoid considering data that may display lower strengths due to the defects introduced during the preparation.

A recent review provided a large collection of data from different materials and it included a description of the purity level in the material, the fabrication method, the procedure used for estimating the grain size and the type and conditions of mechanical testing for each set of data [51]. A few sources of scattering in the data were identified. It is reported that the purity level in each alloy can affect significantly the data and an example is given for Nb where a dispersion of roughly 2 × is observed in the flow stress for similar grain sizes in different reports [55]. Fig. 16 shows another example where the flow stress of titanium with different purity levels is plotted as a function of $d^{-1/2}$ [100]. These data reveal a difference of over 2 × in the flow stress for similar grain sizes depending on the amount of

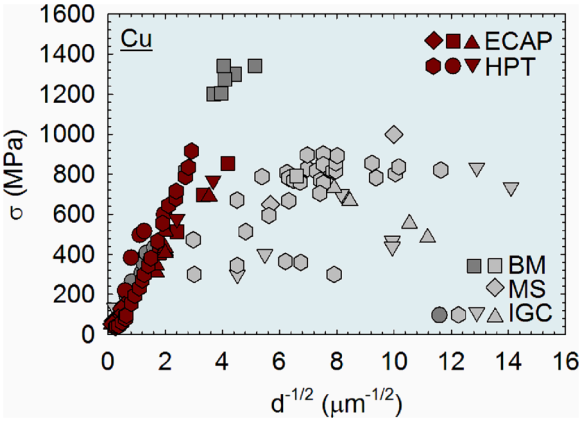

Fig. 15. Flow stress of copper plotted as a function of the inverse of the square root of the grain size. The data were collected from the literature and include materials processed by equal-channel angular pressing (ECAP) [156–158], high pressure torsion (HPT) [153,154,159], ball milling (BM) [128,151] magnetron sputtering (MS) [160] and inert gas condensation (IGC) [91,150,161,162].

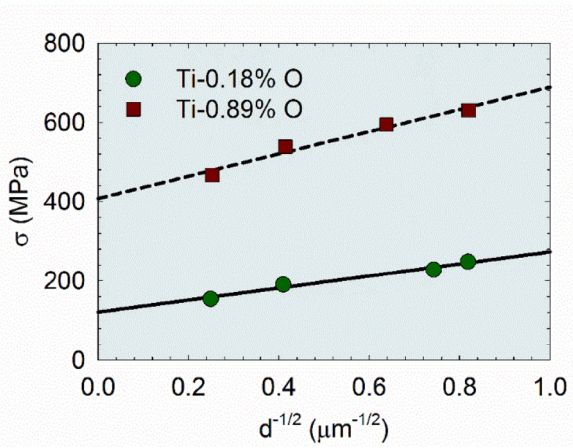

Fig. 16. Flow stress of titanium with different purity levels. Data taken from the literature [100].

oxygen incorporated as impurities. In practice, this difference is expected to be larger in coarse-grained samples due to the larger contribution of the threshold stress to the overall flow stress in this range.

The σ vs $d^{-1/2}$ relationship can also be affected by texture and this is more significant in h.c.p. metals. For example, the constants σ_0 and K in Eq. (1) depend on processing and the loading directions in magnesium and its alloys. A summary of values reported for the constant K is available [163] and differences over 2 × are reported. Experiments in which the loading direction was varied in hot-rolled magnesium alloy revealed that σ_0 varies up to ~ 4 × and K varies over 2 × for the same material depending on the loading direction [164]. A procedure was recently developed to estimate the values for these constants as a function of the texture parameters [165]. Examples of variations of over 2 × in the value of K for pure magnesium were depicted earlier in Fig. 6c.

5.1. *The estimation of the flow stress*

Multiple sources of dispersion in data for different sets of experiments fall within the estimation of the flow stress. The transition from the elastic to the plastic regime can be hard to identify in many materials and this is especially true for coarse-grained samples. The use of a precision extensometer increases the accuracy of the measurements but it remains necessary to decide upon an appropriate yield criterion. The most common criterion is to consider the flow stress as equal to the stress at a plastic strain of 0.002 or 0.2 %. However, some authors report the stress at different levels of strain and many studies rely on mechanical testing without the use of precision strain measurement devices and this causes differences in the reported trends and a dispersion in the data collected from multiple sources.

Fig. 17 shows data for σ vs $d^{-1/2}$ at different levels of strain, ε, for Cu-30 % Zn brass [166] and it is apparent that the stress levels and the intercept with the stress axis, σ_0, increase with increasing strain. This effect is noticeable in coarse-grained materials that display significant strain hardening and may play a major role in any comparison of data obtained from hardness measurements and uniaxial loading mechanical testing. For example, a plastic deformation in the range of ~ 8 % is introduced in the material when making hardness indentations [167] so that, in practice, hardness testing evaluates the strength of an area which was subjected to plastic

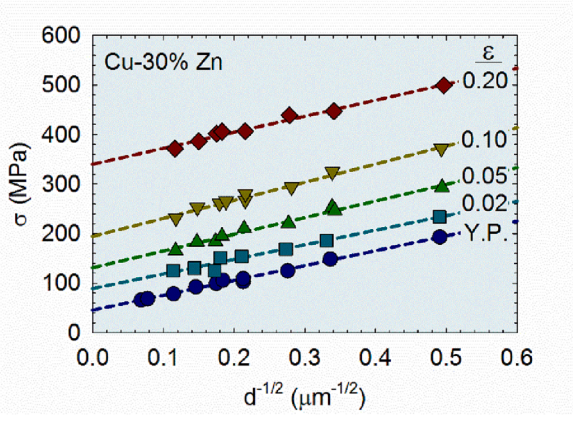

Fig. 17. Flow stress at different strain levels plotted as a function of the grain size for Cu-30% Zn [166]. Y.P. denotes the yield point.

deformation and if the material displays strain hardening the hardness measurements will overestimate the stress required for plastic deformation of the material. The strain hardening has a larger effect on the constant σ_0 than on the slope K as observed in an example for the Cu-30 % Zn alloy shown in Fig. 17. The disagreement between the constant σ_0 reported in experiments based on tensile tests and hardness tests in niobium was clearly illustrated elsewhere [55].

Many of the techniques used to produce materials with grain sizes below 1 μm are limited to small samples. Even though there have been many advances in scaling up the production of nanocrystalline materials, most of the results in the literature for these materials were obtained from small samples. This situation puts a challenge on mechanical testing and, as a consequence, many reports are based on hardness testing. As noted earlier, hardness tests can overestimate the strength of strain hardening materials. However, ultrafine-grained materials usually do not display any significant strain hardening ability and the Tabor rule [148] relating the flow stress to the hardness divided by 3 has been found to stand for ultrafine-grained materials [168].

The relationship between hardness and flow stress is not straight forward for situations in which the indentation is too small as in nanoindentation. The indentation size effect is known as an increase in hardness with decreasing indentation size [169]. In practice, the values of the hardness measured with microhardness and conventional hardness testing tend to display good correlations with the flow stress of ultrafine-grained materials while nanoindentation experiments tend to overestimate the strength. The size effect can also affect compression tests in nano- and micro-pillars. For example, a difference of ~ 2 times was observed in the flow stress of ultrafine grained magnesium tested using miniature tensile specimens and micro-pillars [122].

In addition to hardness tests, some studies on ultrafine and nanocrystalline materials make use of mechanical testing using miniature specimens. These tests provide important additional information about the mechanical behavior of these materials although they may display less accuracy than conventional tensile testing. There are no standard specimen geometries for these tests and many experiments are carried out without using accurate strain measurement devices. Machining and spark erosion are common methods employed to produce these miniature specimens and special apparatus is then needed to attach them to the testing machine. The sources of inaccuracies, therefore, will probably include the load cell range, the strain measurements, loose parts in the special apparatus for testing and an overall poor finishing of the specimens. These inaccuracies play a significant role in any determination of the transition between the elastic and plastic regime. As ultrafine and nanocrystalline materials usually fail to display any significant hardening, one way to reduce the dispersion of results is to consider the flow stress in these materials as the stress after a few percent of deformation. Also, the absence of a well-defined standard for the specimen dimensions can increase the dispersion in the elongation measurements. However, it is important to note that the use of digital image correlation techniques can improve significantly the accuracy of the mechanical testing of miniature samples [170,171]. Other methods to evaluate the mechanical properties of small samples include the use of shear punch tests [172] and plane strain compression tests [173,174].

5.2. Grain size measurements

The grain size estimates are another major source of dispersion in data in the literature. Different techniques are used to reveal the grain boundaries including the etching of polished surfaces and observations on optical or scanning electron microscopes (SEM), determinations of crystalline orientations usings electron back scattered diffraction (EBSD) and observations of transparent lamella using TEM. These techniques enable the observation of a 2-dimensional section of the grain structure of the material whereas the true grains are space-filling polyhedrons [175]. It is possible to estimate the true spatial grain size from 2-dimensional sections if some assumptions are considered regarding the grain shape. As noted earlier, a relationship between the mean linear intercept length, $\overline{L}$, and the spatial grain size, d_s, is given by $d_s = 1.74 \times \overline{L}$ [118]. This difference in grain size measurement techniques clearly affects the slope, K, of the σ vs $d^{-1/2}$ plots. Other methods are also used to determine the grain size including measurements of the distance between boundaries of individual grains followed by a calculation of the average value which may be calculated from the arithmetic average of each count or by considering the area fraction of the grains. The estimate of grain size from TEM images is not easy since the boundaries are not always clearly resolved and it may be difficult to differentiate sub-grain boundaries from grain boundaries.

The aspect ratio of the grains is also an important parameter which sometimes is not considered in any estimate of the grain size. Elongated grains with large aspect ratios contain different distances between boundaries which can affect the strength of the material. Also, the estimated grain size will depend on the orientation at which the grain structure is observed.

The grain size can be estimated also from X-ray diffraction (XRD) patterns. Specifically, the grain boundaries affect the peak broadening and there are direct methods for estimating the grain size. Although some reports show good correlations between the grain sizes estimated from XRD patterns and TEM observations, in general it is found that the former underestimates the grain dimensions. Finally, grain growth may occur during the experiments and this is well-established in high temperature testing but there are also studies revealing room temperature grain growth during deformation of nanocrystalline Al [176,177] and Ni [178] and ultrafine-grained Mg [122].

Finally, it is important to note that materials with similar average grain sizes can display different properties and the grain boundary character is expected to play a significant role in the mechanical behavior. For instance, it has been reported that the fraction of high-angle boundaries affects the stress and strain rate for superplastic flow in aluminum alloys [179–181]. It was also reported that grain boundary relaxation can increase the stability of the grain structure [182,183]. The grain boundary stability was found to play a significant role in the strength of a nanocrystalline Ni alloy [178]. Moreover, the grain size distribution can vary significantly in different samples. In fact, it has been reported that the use of a volume-weighted average grain size, instead of an average grain size, provides a better description of the Hall-Petch relationship [184]. It is therefore essential to remember that a spreading from different sources will be always present when considering experimental data from multiple sources.

6. Relationship between flow stress and grain size at room temperature

A large set of experimental data was collected from the literature for different materials and care was employed to avoid using data from nanoindentation experiments or data in which the grain size was estimated solely by XRD. The collected results were aimed to cover a broad range of grain sizes to enable a valid estimation of trends and the data were then compared to the model discussed earlier for grain boundary sliding [50].

In order to evaluate the predictions from the model, it is necessary to also include the contributions of any other hardening mechanisms to the flow stress. These other sources include the flow stress for the material single crystal and may include the contribution from solid solutions in metallic alloys where, in practice, these contributions are incorporated within the parameter σ_0. The overall flow stress is then given by the following Eq. (19) which considers the spatial grain size and Eq. (20) which considers the mean linear intercept grain size:

$$\sigma = \sigma_0 + \sqrt{\frac{3GkT}{2d_s b^2} ln\left(\frac{\dot{\varepsilon} {d_s}^3}{10\delta D_{gb}} + 1\right)} \tag{19}$$

and

$$\sigma = \sigma_0 + \sqrt{\frac{\sqrt{3}GkT}{2d_l b^2} ln\left(\frac{\dot{\varepsilon} {d_l}^3}{2\delta D_{gb}} + 1\right)} \tag{20}$$

The fundamental properties of the materials considered in the subsequent analysis are listed in Table 1 and the data are collected from multiple sources [114,116,185–197] due to the large number of materials considered. The variation of the shear modulus, G, as a function of the absolute temperature is estimated for some materials. The exact value for the grain boundary diffusion coefficient is not readily available for all materials and therefore the pre-exponent and the activation energy were estimated from the general equations [198] based on the melting temperature of the material.

Table 1
Summary of data for melting temperature (T_m), Burgers vector (b), shear modulus (G) at 298 K, pre-exponential ($\delta D_{0,gb}$) and activation energy (Q_{gb}) for grain boundary diffusion for different metals.

Metal	T_m (K) [185–187,197]	b (nm) [188,189,194]	G (MPa) [185–187,189,193,199]	$\delta D_{0,gb}$ (10^{-14}m^{3}s^{-1})	Q_{gb} (kJ.mol^{-1})
Al	933	0.2864	29,500 – 13.6 × T	5[189]	84[189]
Ag	1234	0.2889	29,900 – 11.6 × T	0.45[189]	90[189]
Au	1336	0.2884	27,700	0.019[190]	112[190]
Be	1556	0.2286	150,000	1.5[b]	133[b]
Bi	545	0.3071	12,800	3.9[a]	45[a]
Cd	594	0.293	27,800	5[189]	54.4[189]
Co	1768	0.2497	82,000	1.5[b]	151[b]
Cr	2133	0.2498	135,000 – 29.5 × T	0.5[189]	192[189]
Cu	1357	0.2556	47,100 – 16.7 × T	0.5[189]	104[189]
Fe (b.c.c.)	1809	0.248	72,600 – 28.7 × T	110[189]	174[189]
Fe (f.c.c.)	1809	0.258	93,200 – 40.7 × T	7.5[189]	159[189]
Hf	2500	0.3127	56,000	35[191]	212[191]
In	429	0.3251	3700	3.9[a]	35[a]
Mg	922	0.321	19,200 – 8.8 × T	500[189]	92[189]
Mo	2888	0.2725	140,000 – 19.7 × T	5.5[189]	263[189]
Nb	2740	0.2864	37,500	5[189]	263[189]
Ni	1728	0.2492	87,700 – 29.3 × T	0.35[189]	115[189]
Pb	600	0.3500	5600	8[189]	66[189]
Pd	1825	0.2751	43,600	0.97[b]	138[b]
Pt	2042	0.2775	61,000	0.97[b]	154[b]
Re	3453	0.2741	181,000	1.5[b]	295[b]
Sn	505	0.3022	18,400	0.3[190]	40[190]
Ta	3253	0.2856	69,000	5.7[189]	280[189]
Ti (h.c.p.)	1940	0.2896	51,700 – 27.0 × T	450[191]	187[191]
Ti (b.c.c.)	1940	0.286	22,000 – 5.16 × T	0.0054[189]	153[189]
U	1430	0.285	75,000	3.9[a]	118[a]
V	2175	0.2618	52,700 – 8.7 × T	5[189]	209[189]
W	3683	0.2741	165,000 – 16.6 × T	33[189]	385[189]
Zn	693	0.2665	60,000 – 35.6 × T	1.3[189]	60.5[189]
Zr	2125	0.3179	40,000 – 21.2 × T	74[191]	188[191]
CrMnFeCoNi	1607	0.254	$85000 - \frac{16000}{(e^{448/T} - 1)}$	14,200 [195]	221[195]

[a] The values for $\delta D_0 = 3.9 \times 10^{-14}$ and $Q_{gb} = 82.5 \times T_m$ were estimated from average correlations [198] between bcc, fcc and hcp structures.
[b] Adapted from the suggested general equations [198] for fcc ($\delta D_0 = 9.7 \times 10^{-15}$; $Q_{gb} = 75.4 \times T_m$) and hcp ($\delta D_0 = 1.5 \times 10^{-14}$; $Q_{gb} = 85.4 \times T_m$) metals.

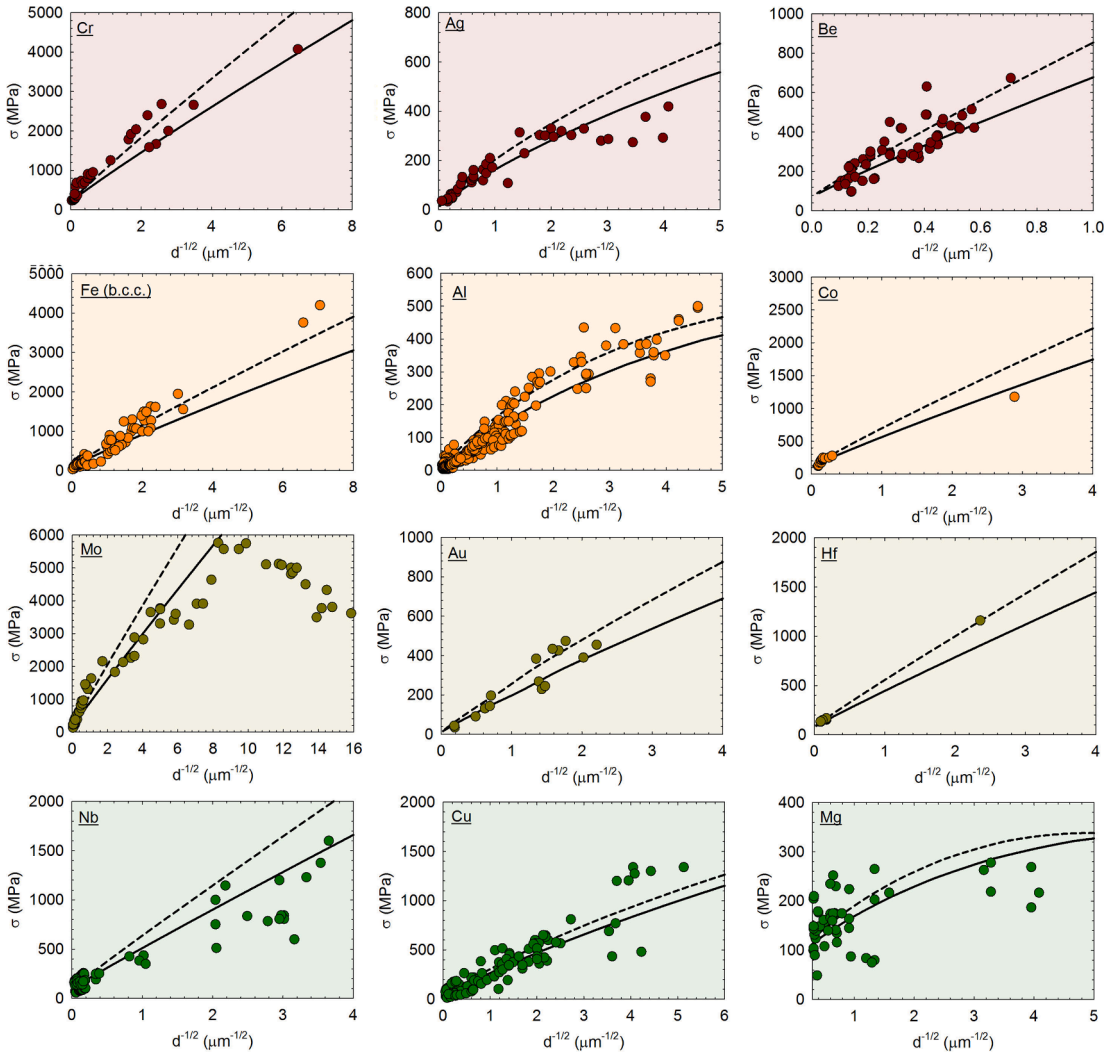

Fig. 18. Flow stress predicted by the model of grain boundary sliding plotted as a function of the inverse of the square root of the grain size. Experimental data taken from the literature for Al [4–25], Ag [200–206], Au [207–210], Be [211–217], Co [218,219], Cr [203,220–223], Cu [95,121,150,151,153,154,156,157,159,224–235], Fe (b.c.c.) [61,96,102–104,236–248], Fe (f.c.c.) [97,237,249–255], Hf [256,257], Mg [63,64,66,105,110–112,258–262], Mo [263–270], Nb [79,271–281], Ni [3,178,282–292], Pd [293,294], Pt [295,296], Re [297,298], Ta [203,299,300], Ti (b.c.c.) [101,301,302], Ti (h.c.p.) [100,303–314], V [269,300,315–320], W [321,322], Zn [51,70,325–329] and Zr [330–335].

Fig. 18 shows the flow stress plotted as a function of $d^{-1/2}$ for 24 different metals with b.c.c. (left column), f.c.c. (middle column) and h.c.p. (right column) structures. Experimental data was taken from the literature for Al [4–25], Ag [200–206], Au [207–210], Be [211–217], Co [218,219], Cr [203,220–223], Cu [95,121,150,151,153,154,156,157,159,224–235], Fe (b.c.c.) [61,96,102–104,236–248], Fe (f.c.c.) [97,237,249–255], Hf [256,257], Mg [63,64,66,105,110–112,258–262], Mo [263–270], Nb [79,271–281], Ni [3,178,282–292], Pd [293,294], Pt [295,296], Re [297,298], Ta [203,299,300], Ti (b.c.c.) [101,301,302], Ti (h.c.p.) [100,303–314], V [269,300,315–320], W [321–324], Zn [51,70,325–329] and Zr [330–335]. The data for f.c.c. Fe was based on 304, 316 and 321 austenitic stainless steel, the data for b.c.c. Ti was based on the Ti-15 % Mo beta alloy and the data for Pt was based on the Pt-5 % Ru alloy. Many of the experimental data were collected from a recent review [55].

The predictions from the model of grain boundary sliding are also shown in Fig. 18 considering spatial grain size (dashed line) and linear intercept grain size (continuous line). The threshold stress, σ_0, was estimated from best fits with the experimental data. A strain rate of 10^{-3} s^{-1} was considered as representative of quasi-static testing. A comparison between the predictions from the model for some materials and the experimental data, in which the flow stress is plotted as a function of the grain size, is available elsewhere [116].

The extent of the experimental data for Co, Hf and Re is not large but they include a broad grain size and flow stress range. Experimental data for samples with grain sizes smaller than ~ 20 nm are available and show grain refinement hardening down to the

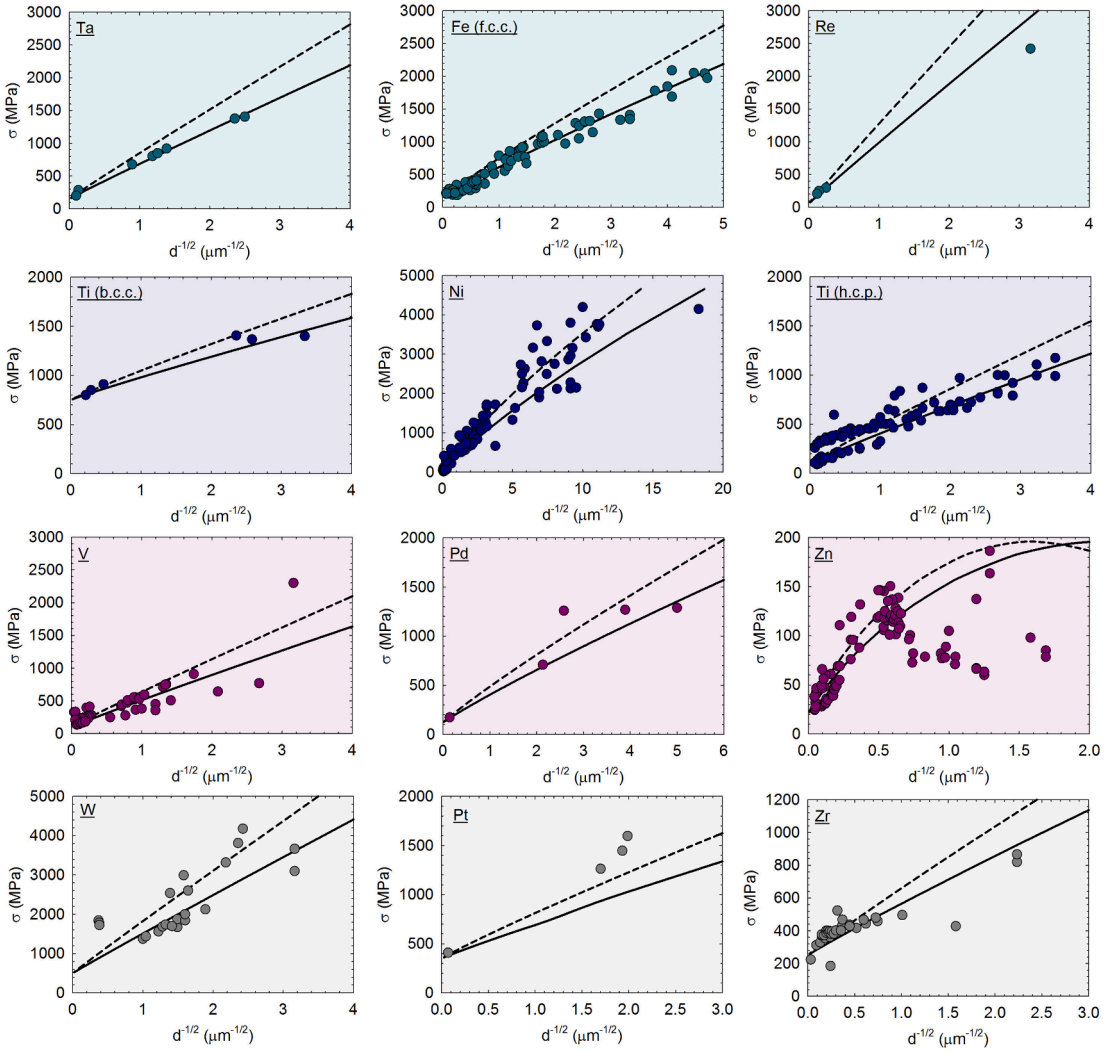

Fig. 18. (*continued*).

nanocrystalline range for a few metals including Cr, Fe (b.c.c.), Mo and Ni. However, a peak in strength is observed at grain sizes of ~ 10 nm in Mo and softening, or inverse Hall-Petch behavior, is observed at smaller grain sizes. Materials with lower melting points, such as Mg and Zn, may display inverse Hall-Petch behavior at small grain sizes and a fairly good agreement is observed between the experimental data and the model. Twinning-controlled deformation plays a major role in the Hall-Petch relationship of coarse-grained Mg. As a consequence, there is a greater dispersion in experimental data for this material and the graph only shows data for grain sizes smaller than ~ 10 μm since slip-controlled deformation is expected for the deformation in finer-grained Mg. This will be discussed further in a later section. Overall, the predictions from the model for this broad range of materials show very good agreement with the experimental data and this provides significant support for the validity of this approach.

The prediction for cadmium is not shown due to the limited range of experimental data [336,337] available but a plot is shown elsewhere [116]. Other materials were also evaluated. Fig. 19 shows the predictions of the model and experimental data for uranium [192,338] and a CrMnFeCoNi alloy [339–352] which also show good agreement despite the low symmetry of the crystalline structure of uranium and the multi component composition of the CrMnFeCoNi alloy.

Some materials with low melting temperatures display inverse Hall-Petch behavior at room temperature and this is also predicted by the model. Fig. 20 shows the prediction from the model for Bi, Pb and Sn. Lead will display an inverse Hall-Petch behavior at grains smaller than a few hundreds of nanometers at a strain rate of 10^{-3} s^{-1} where this is out of the range shown in Fig. 20. However, Bi and Sn display grain refinement softening for grains in the micrometer scale and this is in agreement with experimental data for Bi-Sn [75] and Sn-Pb [74,353,354] alloys.

Some earlier plots included data from alloys which were then compared to the predictions for pure metals showing that generally a good agreement is observed. For example, data for austenitic stainless steel were compared to predictions for f.c.c. Fe and the Ti-15 % Mo alloy was compared to b.c.c. Ti. Also, in order to predict [117] the flow stress of multicomponent alloys, such as the CrMnFeCoNi

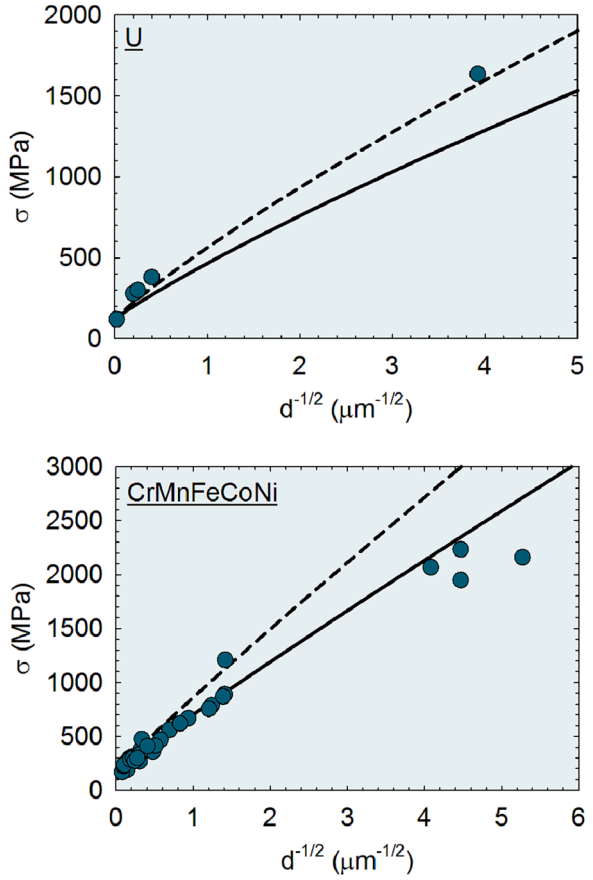

Fig. 19. Flow stress predicted by the model and data taken from the literature for uranium [192,338] and CrMnFeCoNi [339–352].

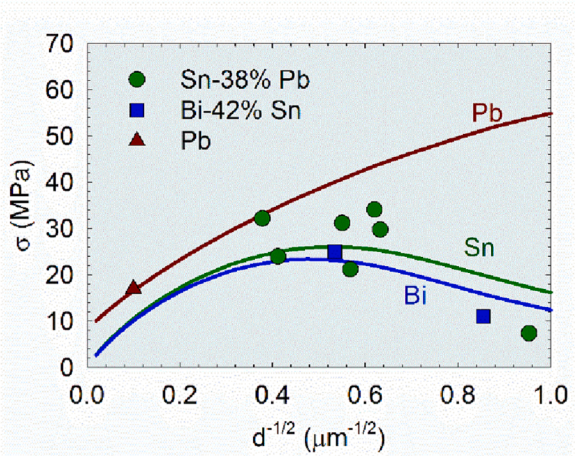

Fig. 20. Flow stress predicted by the model for Pb, Sn and Bi and data taken from the literature for Pb [293] and Bi-Sn [75] and Sn-Pb [74,353,354] alloys.

alloy, it is necessary to estimate the fundamental properties of the alloy. However, minor additions of alloying elements that do not alter significantly the fundamental properties of the pure metal are not expected to change the slope of the σ vs $d^{-1/2}$ plots. For example, the experimental data of Zn-22 % Al, Sn-38 % Pb and Bi-42 % Sn agree with the predictions for Zn, Sn and Bi since these are the major phases in these eutectoid or eutectic alloys and the flow stress is mostly controlled by their deformation.

In order to further evaluate the effect of alloying elements, the experimental data for Al-Mg [22,355–358], Mg-Al [359–367], Cu-Zn

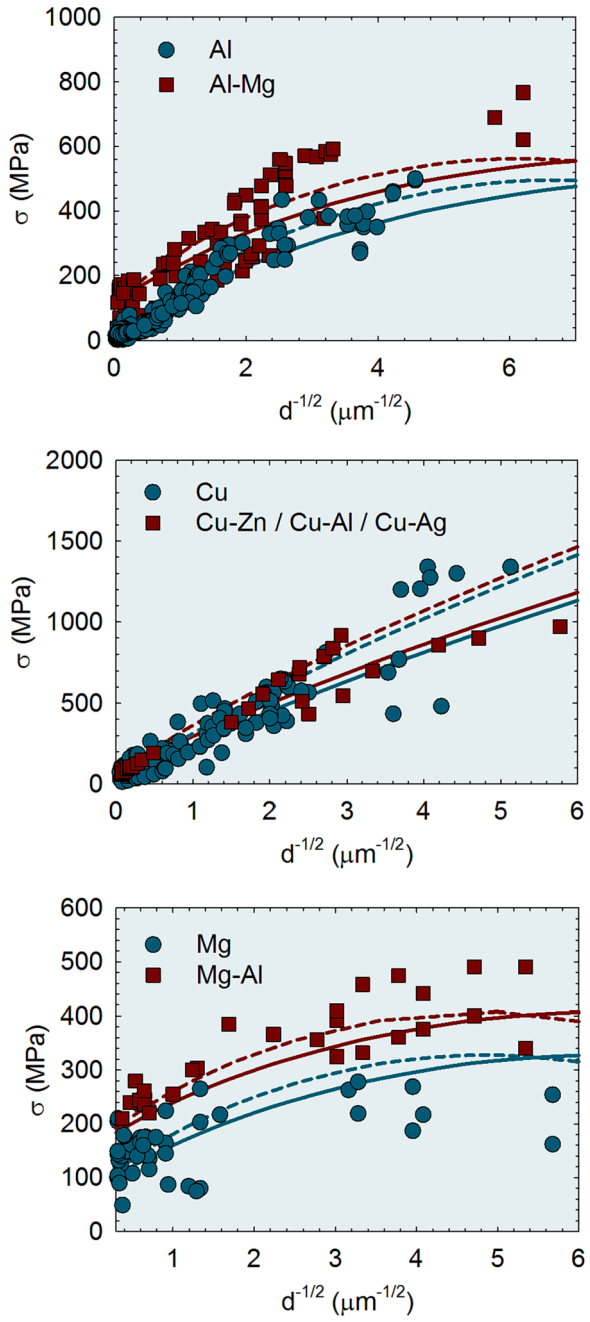

Fig. 21. Flow stress predicted by the model and experimental data for Al [4–25] and Al-Mg [22,355–358] alloy, Cu [95,121,150,151,153,154,156,157,159,224–235], Cu-Zn [166,368], Cu-Al [158,369] and Cu-Ag [153] alloys and Mg [63,64,66,105,110–112,258–262] and Mg-Al [359–367] alloy.

[166,368], Cu-Al [158,369] and Cu-Ag [153] alloys are plotted as a function of the inverse of the square root of the grain size in Fig. 21 and compared directly to experimental data for the pure metals of Al, Mg and Cu and the predictions from the model considering the fundamental properties of the pure metals. It is observed that, as expected, the alloys follow similar slopes to the pure metals and the main difference between the trends observed in the alloys and in the pure metals is limited to the threshold stress, σ_0. The alloying elements may contribute to the strength of the material through the solid solution and this contribution is incorporated in the threshold stress.

The model does not predict a linear relationship between the flow stress and the inverse of the square root of the grain size for all materials and all grain size ranges. In fact, the predictions show a tendency of decreasing slope with decreasing grain size and this tendency is more prominent in low melting point materials such that the inverse Hall-Petch behavior takes place at small grain sizes.

Table 2
Hall-Petch constants estimated using best fits to the experimental data and estimated using Eq. (17) and Eq. (18) for testing at room temperature and at 10^{-3} s^{-1}. The grain size range for the calculations was 100 nm unless indicated in parentheses.

Metal	σ_0 (MPa)	K_{Exp} (MPa μm$^{1/2}$)	K^l_{GBS} (MPa μm$^{1/2}$)	K^s_{GBS}. (MPa μm$^{1/2}$)
CrMnFeCoNi	232	415	500	648
Ag (0.3 μm)	28	150	138	173
Al (0.3 μm)	10	109	116	142
Au (0.3 μm)	3	220	185	237
Be	80	737	612	788
Bi (10 μm)	–	–	58	67
Cd (10 μm)	14	100	110	133
Co	153	356	416	537
Cr	406	646	628	815
Cu	24	241	210	265
Fe (b.c.c.)	64	570	395	510
Fe (f.c.c.)[a]	184	406	410	529
Hf	90	454	346	449
Mg (0.3 μm)	139	20[b]	79	95
Mo	316	580	722	941
Nb	127	284	395	515
Ni	197	309	330	419
Pb (10 μm)			56	70
Pd	282	240	257	330
Pt[c]	355	579	358	464
Re	125	726	904	1180
Sn (10 μm)	–	–	61	72
Ta	208	495	514	671
Ti (b.c.c.)[d]	800	210	197	254
Ti (h.c.p.)	230	246	287	371
U	188	370	274	348
V	138	412	393	510
W	960	854	986	1292
Zn (2 μm)	27	165[e]	154	185
Zr	321	214	239	310
Al-Mg alloy (0.3 μm)	100		116	142
Cu alloys	100	191	210	264
Mg-Al alloy (0.3 μm)	211	50	65	77

[a] Considering austenitic stainless steel.
[b] Considering only $d < 10$ μm.
[c] Considering Pt-5% Ru alloy.
[d] Considering Ti-15% Mo alloy.
[e] Considering only $d > 2$ μm.

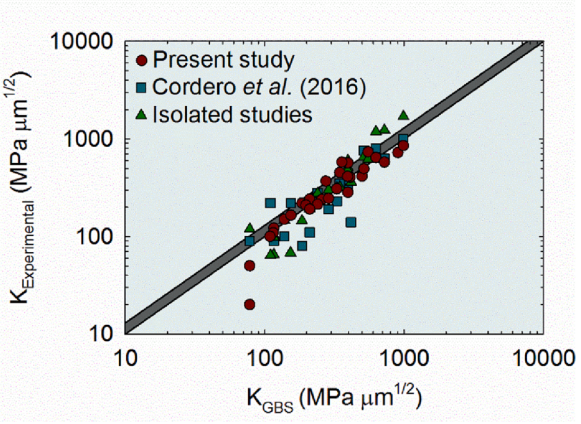

Fig. 22. Hall-Petch slopes K estimated from experimental data in the present study and in a recent review [55] and the values documented in a recent report [370] based on experimental data from isolated studies [14,51,200,209,211,218,220,229,256,263,272,288,300,304,371–377] plotted as a function of the theoretical values of slopes estimated using the grain boundary sliding model.

However, the predictions are fairly linear for many materials over a broad range of grain sizes such that an approximation enables the use of Eq. (2), considering the slope K_{GBS} estimated using Eqs. (17) and (18). Table 2 lists the approximate values of the threshold stress, σ_0, and the Hall-Petch slope $K_{Exp.}$ estimated from a best fit to the experimental data considered in the present analysis and also shows the slopes estimated considering both a spatial grain size, K^s_{GBS}, and a mean linear intercept grain size, K^l_{GBS}. Most of the slopes were estimated considering a grain size of 100 nm for the range but other values, indicated in parentheses, were considered depending on the range of data in the plots and the validity of the mechanism for lower melting point materials.

Overall, the predictions from the model of grain boundary sliding [50] agree well with experimental data from multiple materials tested at room temperature. It is worth noting that the previous analysis was based on experimental data acquired from conventional mechanical testing in which the strain rate is usually in the range of $\sim 10^{-3}$ s^{-1} and this was the strain rate used as the input in the model. In practice, small variations in the strain rate do not affect the predictions significantly for materials with high melting points when tested at room temperature. However, the model predicts that the strain rate plays a significant role for low melting point materials.

In order to evaluate the effectiveness of the model, the values of the slope K estimated from the experimental data are plotted as a function of the theoretical slopes K_{GBS} in Fig. 22. In order to reduce the bias in selecting the experimental data, values of the slope K estimated for different materials in a recent review [55] are also included in the plot. Moreover, values of the slope K selected for different materials in a recent report [370], based on isolated studies in the literature [14,51,200,209,211,218,220,229,256,263,272,288,300,304,371–377], are also shown. Black lines delineate the lower and upper bounds predicted by the model considering the linear intercept grain size as a lower bound and the spatial grain size as an upper bound. The plot shows that the experimental values from the present study display fairly good agreement with the values reported by other authors. It also shows good agreement between the experimental values of K and the theoretical prediction for materials with K values larger than $\sim$ 200 MPa μm$^{1/2}$.

Two points should be mentioned regarding the materials which display low values of K. First, some of the materials in the low K range are Ag, Al, Mg and Zn which have relatively low melting temperatures. An analysis of the data in Fig. 18 shows that the relationship between flow stress and the inverse of the square root of the grain size is not linear for a wide range of grain sizes in these materials. This means that the approximation to a Hall-Petch relationship given by Eq. (2) with a fixed slope K is not accurate. The dispersion in experimental values of K for these materials in the literature supports the assumption of varying slopes over different grain size ranges. Although the approximation to a fixed Hall-Petch slope does not agree with the experimental K, Eqs. (15) and (16) display good agreement with the experimental data of flow stress in Fig. 18. A second point that should be mentioned is that some materials display a lower slope in the coarse-grained region and a higher slope in the fine-grained region causing a dispersion in the values of K in different studies and this topic will be further discussed in a later section.

The Hall-Petch relationship has also been evaluated using computer molecular dynamics simulations. However, due to computing limitations these simulations usually consider very high strain rates, over $\sim 10^8$ s^{-1}, and the predictions of flow stress are usually significantly larger than the values observed in quasi-static experiments. It is interesting to note that the model of grain boundary sliding predicts a contribution from the strain rate and therefore it is possible in practice to compare its predictions to molecular dynamics simulations. Thus, Fig. 23 shows data from simulations for nanocrystalline Cu [141,378] and Al [379,380] together with the prediction from the model considering a linear intercept grain size and a strain rate of 10^8 s^{-1}. It is important to note that the molecular dynamics simulations usually predict grain refinement hardening followed by a maximum in strength at a very small grain size and an inverse Hall-Petch behavior for smaller grains. Thus, the data for inverse Hall-Petch predicted in the simulations are not included in Fig. 23 since a different mechanism is expected to then become rate-controlling. Some simulations considered slightly higher strain rates of $\sim 10^{10}$ s^{-1} and it was found that this difference by two orders of magnitude has no significant effect on the predictions from the model. It is observed that a very high strain rate increases the slope predicted by the model of grain boundary sliding [50] for both

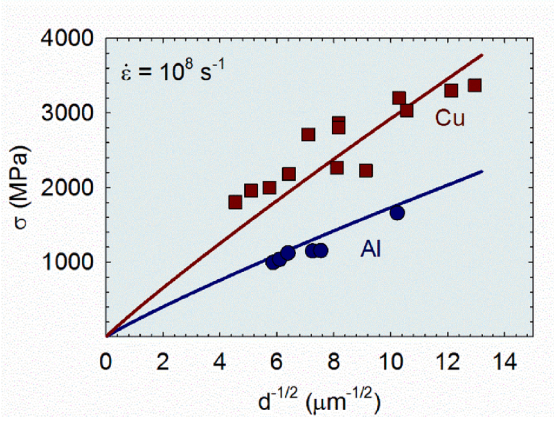

Fig. 23. Flow stress predicted at a high strain rate of 10^8 s^{-1} compared to data taken from the literature for molecular dynamics simulations of Cu [141,378] and Al [379,380].

materials and a good agreement is obtained with the data from the molecular dynamics simulations. The effect of strain rate and temperature on the relationship between flow stress and grain size is further discussed in the next section.

7. Effect of strain rate and temperature

The temperature and the strain rate play significant roles in the relationship between flow stress and grain size and their importance appears to increase in the ultrafine and nanocrystalline ranges. In general, the flow stress decreases with increasing temperature and decreasing strain rate but in practice the rate of softening is not straight forward for all grain sizes and different aspects of these relationships are now examined. It is interesting to initially visualize a general view of the effect of strain rate and temperature as predicted by the model of grain boundary sliding [50]. This is provided in Fig. 24 where the flow stress, σ, is plotted as a function of the strain rate, $\dot{\varepsilon}$, on a logarithmic scale using arbitrary units. Three general temperatures are considered in which one is representative of low temperatures, one of moderate temperatures and the other is for high temperature testing. These three temperature regimes are not absolute for all materials. In fact, the temperature effect is incorporated in the model by its effect on the grain boundary diffusion coefficient which is generally a function of the material melting temperature [190,191,198]. Thus, the concepts of "low", "moderate" and "high" temperatures vary depending on the material. A general correlation suggests that "low" temperature behavior is observed at $T < 0.3\ T_m$, "moderate" temperature behavior at $0.3\ T_m < T < 0.5\ T_m$ and "high" temperature behavior at $T > 0.5\ T_m$ where T_m is the absolute melting temperature of the material.

Two grain sizes, d_1 and d_2, are considered as representative of ultrafine and fine-grained materials, respectively, so that $d_1 < d_2$. Thus, at low temperatures the flow stress of ultrafine-grained materials is higher than fine-grained and the material follows the conventional Hall-Petch behavior. At moderate temperatures there is a transition in which the ultrafine-grained material may be stronger at high strain rates and softer at low strain rates, and the ultrafine-grained material tends to be softer at high temperatures and low strain rates. This general description suggests that the transition between grain refinement hardening (the low temperature regime) and grain refinement softening (the high temperature regime) is incremental and depends on both the temperature and the strain rate. It also depends on the grain size range that is under consideration.

This general view suggests that the transition between grain refinement hardening and grain refinement softening is due to a higher slope in the curves of the samples with finer grain sizes. This slope is associated with the strain rate sensitivity, m, defined as $m = \partial ln\sigma / \partial ln\dot{\varepsilon}$ which plays a major role in determining the mechanical behavior. Thus, the model of grain boundary sliding predicts that the slope of the curves increases with decreasing strain rate and with increasing temperature until it reaches a maximum of 0.5 which is the strain rate sensitivity associated with high temperature grain boundary sliding and superplasticity [33]. This analysis then suggests that samples with finer grains will display superplastic behavior at faster strain rates. The patterns depicted in Fig. 24 will depend also on the strain rate range and the grain size range. It is expected that the threshold stress will also affect the predictions. This general prediction is now compared to experimental trends and data.

Thus, the qualitative prediction from the model of grain boundary sliding [50] suggests that materials with finer grains display a higher slope in the flow stress vs strain rate plot which is associated with a higher strain rate sensitivity. This agrees with multiple reports of increasing strain rate sensitivity with decreasing grain size in many materials including copper [381], aluminum [382,383],

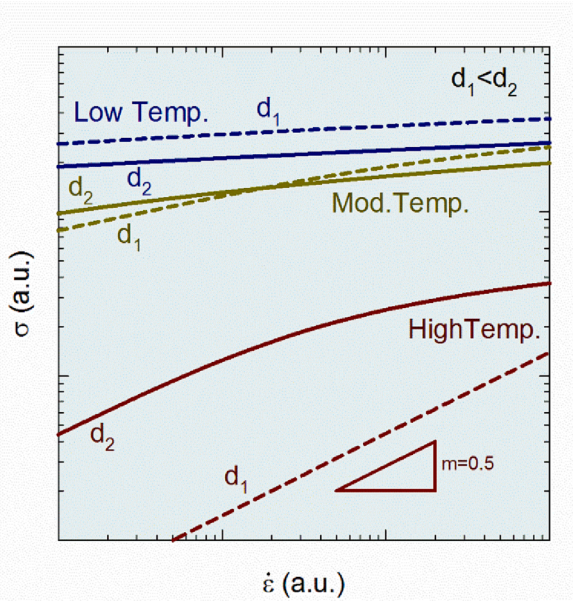

Fig. 24. General view of the relationship between the flow stress and the strain rate for materials with different grain sizes and tested at low, moderate and high temperatures.

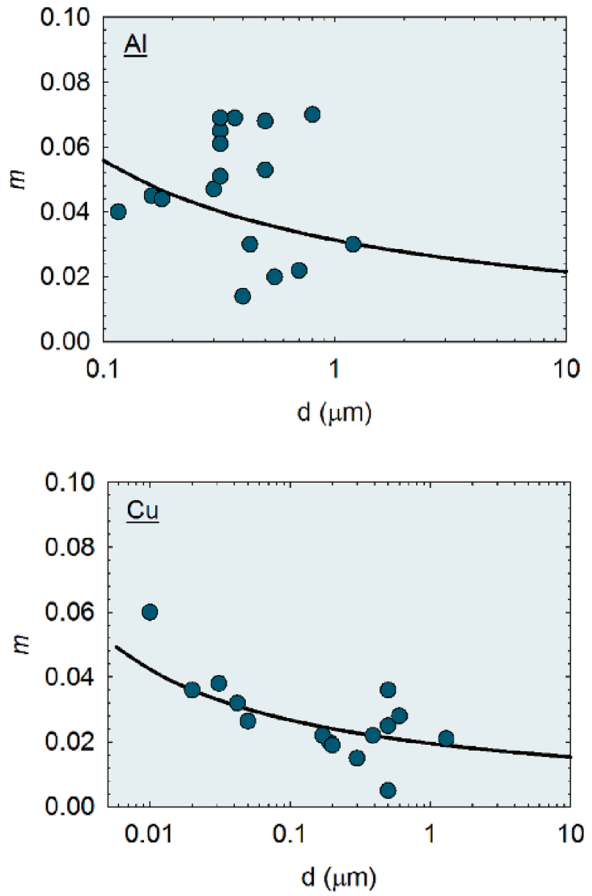

Fig. 25. Strain rate sensitivity, *m*, reported in the literature for Al [4,382,383,385–394] and Cu [160,395–402] plotted as a function of the grain size. The strain rate sensitivity predicted by the model of grain boundary sliding is also plotted as a continuous line.

magnesium [63] and zinc [325]. A summary of strain rate sensitivity data reported in materials processed by SPD is available elsewhere [384]. Therefore, Fig. 25 shows strain rate sensitivity data reported in the literature for aluminum [4,382,383,385–394] and copper [160,395–402] plotted as a function of the grain size. A clear trend of increasing *m* with decreasing grain size is observed in these materials. An equation for the estimation of the strain rate sensitivity for the model of grain boundary sliding is available elsewhere [116]. In practice, the strain rate sensitivity can be estimated from the slopes of the flow stress curves plotted as a function of the strain rate. It is important to remember that the model of grain boundary sliding only predicts the contribution of the grain size to

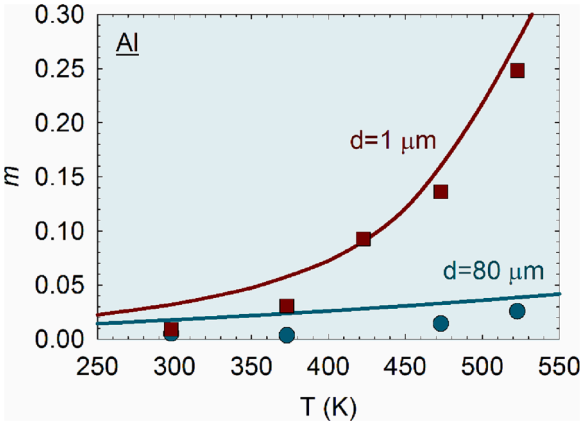

Fig. 26. Strain rate sensitivity of pure aluminum with grain sizes of 1 μm and 80 μm plotted as a function of the temperature. Data from the literature is shown for comparison [382].

the flow stress. Other strengthening mechanisms such as a solid solution strengthening are usually considered thermally-activated and therefore they will affect the strain rate sensitivity. Nevertheless, the contributions of these mechanisms to the flow stresses of pure aluminum and pure copper are expected to be low. Thus, the predicted strain rate senstivities for Al and Cu, considering the linear intercept grain size, are plotted in Fig. 25 and show good quantitative agreement with the experimental data.

Another prediction of the grain boundary sliding model [50] is that the strain rate sensitivity increases in ultrafine-grained materials with increasing temperature. This effect has been reported experimentally [403–405] and Fig. 26 shows an example for pure aluminum in which the strain rate sensitivity, m, was determined for ultrafine-grained samples processed by ECAP and for a coarse-grained sample with $d = 80$ μm [382]. The ultrafine-grained material had an elongated structure of 430 nm in the elongated direction and 270 nm perpendicular to it and the grain size increased to ~ 1 μm upon heating to 473 K. The data show that the strain rate sensitivity is higher in the material with the finer grain structure and increases significantly with increasing temperature. Accordingly, the strain rate sensitivities predicted by the model are also plotted considering linear intercept grain sizes of 80 μm and 1 μm, respectively. The predictions appear to overestimate the strain rate sensitivities at low temperatures but they generally exhibit an overall qualitative agreement with the experimental data.

Another parameter used to evaluate thermally-activated deformation mechanisms is the apparent activation volume. This parameter is usually estimated from the following Eq. (21) and it is related to the strain rate sensitivity [405–407] through the expression

$$v = MkT\frac{\partial \ln \dot{\varepsilon}}{\partial \sigma} = \frac{MkT}{m\sigma} \tag{21}$$

where M is the Taylor factor which relates the shear stress acting on the slip plane and the effective stress in uniaxial loading tests. Some authors consider the von Mises plasticity criterion ($M = \sqrt{3}$) while some authors consider the Taylor factor such that the most used value is $M \approx 3.06$. This parameter can be estimated from the model by considering the variations in flow stress caused by changes in strain rate. Some interesting effects have been observed in ultrafine and nanocrystalline materials. For example, it was reported that the apparent activation volume of ultrafine-grained materials may decrease with increasing temperature [85,403,404,408] and this effect is predicted in these materials by the model of grain boundary sliding as reported recently for a multi-component alloy [117].

Also, it has been observed that the apparent activation volume decreases with decreasing grain size in the ultrafine grain range [85,285,385,395,407]. Some mechanisms have been suggested to explain the Hall-Petch effect such as the mechanism of grain boundary shear promoted by the pile-up of dislocations [85] and a mechanism in which cross-slip controls the transmission of plastic flow across grain boundaries [77] and these mechanisms have addressed these trends and display good agreement with the experimental data. It follows that the grain boundary sliding model also predicts a decrease in v with decreasing grain size. Hence, Fig. 27 shows values of v normalized by b^3 and plotted as a function of the grain size together with the prediction from the model for linear intercept grain sizes considering $M = 3.06$ and estimating the changes in flow stress around 10^{-3} s^{-1}. The apparent activation volume was estimated from reports in the literature and data for Al [4,385,386,393], Cu [232,395,396,398,402,405] and Ni [285,398,403,409–412] are also shown for comparison. The data from the literature, which were estimated considering the von Mises criterion, were converted in order that all data presented in Fig. 27 considers the same criterion of $M = 3.06$. It is readily observed that the values estimated from the model for these materials are fairly similar and show a tendency of increasing v with increasing grain size. Generally, the values predicted by the model agree well with the experimental data.

The model of grain boundary sliding predicts an increase in the strain rate sensitivity with decreasing grain size. This prediction agrees with the experimental observations from metals that display low threshold stresses in such a way that the strength is mainly controlled by the grain size. This includes, for example, pure fcc metals such as Al and Cu. However, this is not the case for other metals

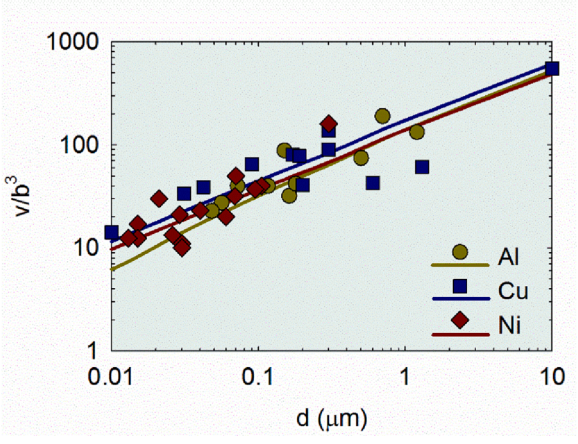

Fig. 27. Apparent activation volume predicted by the model normalized by b^3 plotted as a function of the grain size. Experimental data from the literature for Al [4,385,386,393,413], Cu [160,232,395,396,398,402,405] and Ni [285,398,403,409–412] are also shown for comparison.

such as those with b.c.c. structures. The relationship between m and grain size for these latter materials depends on an estimation of the thermal contribution from the other strengthening mechanisms. Thus, it was shown that the relationship between grain size and strain rate sensitivity differs between pure Ni and high entropy alloys and the difference was attributed to the larger lattice friction stress in the latter [414]. Therefore, the next section evaluates the specific effect of the threshold stress.

8. Threshold stress

The contribution of different strengthening mechanisms was incorporated into a constant threshold stress and estimated empirically in Section 6 based on experimental data in the literature. However, it is important to discuss its general effect on the flow stress at different temperatures and strain rates in order to evaluate the effective contribution of these parameters. It is beyond the scope of the present paper to discuss the individual strengthening mechanisms for each metal and alloy. However, most of the strengthening mechanisms are thermally-activated which means that increasing the temperature and/or decreasing the strain rate also decreases the threshold stress. In practice, the strain rate of thermally-activated mechanisms can be approximated using Eq. (22) [194,396,406,415,416]:

$$\dot{\varepsilon} = \dot{\varepsilon_0}\exp\left(\frac{-\Delta E(\sigma)}{kT}\right) \tag{22}$$

where $\dot{\varepsilon_0}$ is a reference strain rate which can be considered as $\sim 10^5\ s^{-1}$ [417] and $\Delta E(\sigma)$ is the activation energy which is a function of the applied stress.

In practice, the stress contributes to the strain rate by decreasing the activation energy required for deformation. Nevertheless, the explicit estimation of the threshold stress, as a function of strain rate and temperature, is not straight forward. An approximation, which is valid for a range of temperatures, is given by Eq. (23) [418]:

$$\sigma_0 = \sigma_0^*\exp\left(-\frac{1}{0.51}\frac{RT}{\Delta E}\ln\frac{\dot{\varepsilon_0}}{\dot{\varepsilon}}\right) \tag{23}$$

where σ_0^* is the zero temperature flow stress and R is the gas constant. A recent report [117] made use of a similar approximation and estimated the threshold stress of a CrMnFeCoNi multi-component alloy using Eq. (23). The calculations considered $\sigma_0^* = 400$ MPa and $\Delta E = 110$ kJ/mol. Fig. 28 shows the threshold stress estimated using Eq. (23) and appropriate experimental data [339,343,345] of the threshold stress plotted as a function of temperature. A strain rate of $10^{-3}\ s^{-1}$ was considered for the calculation and there is good agreement with the experimental data.

The estimation of the threshold stress at different temperatures and strain rates provides an ability to estimate the overall flow stress of the CrMnFeCoNi alloy over a broad range of testing conditions considering the sum of the threshold stress and the stress predicted by the grain boundary sliding mechanism [50]. Fig. 29a shows the flow stress plotted as a function of $d^{-1/2}$ for different temperatures. The flow stress is then given by Eq. (19) for spatial grain sizes (dashed line) or Eq. (20) for linear intercept grain sizes (continuous line) considering the threshold stress estimated by Eq. (23). Experimental data [339–352,419] are also shown for comparison.

A good agreement is observed between the prediction and the experimental data including the reduced slope and inverse Hall-Petch behavior at 1073 K. It is thus possible to estimate the strain rate sensitivity of this alloy by calculating the flow stress at different strain rates and using an approximation of $m \approx \Delta\ln\sigma/\Delta\ln\dot{\varepsilon}$. Fig. 29b shows the estimated values considering the linear intercept grain size and also considering changes in the strain rate between $10^{-3}\ s^{-1}$ and $3 \times 10^{-3}\ s^{-1}$. It follows that in this case an increase in strain rate

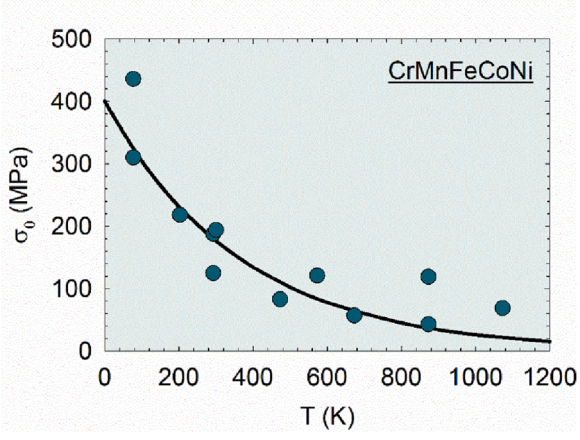

Fig. 28. Threshold stress estimated considering a thermally-activated approximation and experimental data [339,343,345] from the literature for a CrMnFeCoNi multi-component alloy plotted as a function of temperature.

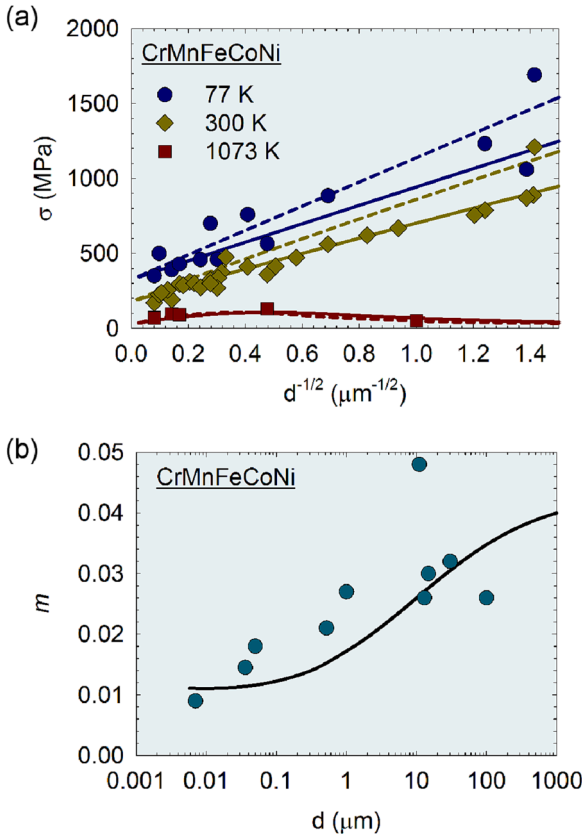

Fig. 29. (a) Flow stress plotted as a function of $d^{-1/2}$ considering the spatial (dashed lines) and linear intercept (continuous lines) grain sizes and the threshold stress estimated using Eq. (16) together with experimental data from the literature [339–352,419] for the CrMnFeCoNi alloy and (b) strain rate sensitivity predicted at room temperature together with experimental data [348,404,408,420–422] taken from the literature.

sensitivity with increasing grain size is predicted and this agrees with data from the literature for the CrMnFeCoNi alloy [348,404,408,420–422] which are shown for comparison.

The previous analysis showed that the relationship between the strain rate sensitivity and the grain size differs between pure f.c.c. aluminum and copper and a multi-component CrMnFeCoNi alloy which also has an f.c.c. structure. The former displays an increased strain rate sensitivity with decreasing grain size while the latter shows the opposite trend. It follows that the trend depends on the magnitude and sensitivity of the threshold stress. It is known that b.c.c. metals display a trend similar to the CrMnFeCoNi alloy in which the strain rate sensitivity decreases with decreasing grain size at room temperature. It is also known that these metals display a significant threshold stress at room temperature. This trend can be predicted by the incorporation of a thermally-activated threshold stress into the analysis as is now examined.

The values of the threshold stress for some b.c.c. metals, estimated from experiments using single crystals or from the intercepts of the Hall-Petch trend lines with the stress axis, were summarized elsewhere [55]. The data for Fe [96,102–104,416,423–425] are plotted in Fig. 30a and it is observed that there is not a continuous trend. An empirical estimation based on Eq. (23), considering $\sigma_0^* =$ 400 MPa and $\Delta E = 48$ kJ/mol, was found to show good agreement with the data for temperatures over 200 K although there was a tendency to underestimate the threshold stress at lower temperatures. Thus, the strain rate sensitivity at room temperature was estimated for b.c.c. Fe and this is plotted as a function of the linear intercept grain size in Fig. 30b. An increase in strain rate sensitivity with increasing grain size is predicted and agrees with the experimental trend as shown by the data taken from the literature [236,396,406,423,426–429]. It follows that the trends of increasing strain rate sensitivity with increasing grain size observed in many b.c.c. metals, such as V [320], Ta [430] and W [323], may be attributed to a significant contribution of the threshold stress in these materials. Experimental data for the threshold stresses in other b.c.c. metals (Mo, Nb, Ta and V) at different temperatures are summarized elsewhere [55].

Although the trend of decreasing strain rate sensitivity with decreasing grain size appears initially to contradict the general view of the effect of strain rate and temperature on the flow stress of samples with different grain sizes as depicted in Fig. 24, it is important to note that this trend is reversed with increasing temperature. Thus, it has been shown that the strain rate sensitivity of ultrafine-grained Fe is larger than its coarse-grained counterpart at 473 K [431]. It was also shown that the strain rate sensitivity of the ultrafine-grained CrMnFeCoNi alloy is significantly larger than its coarse grained counterpart at high temperatures [404]. A further evaluation of the effect of temperature and strain rate on the flow stress requires a consideration of materials having a large set of data available in the

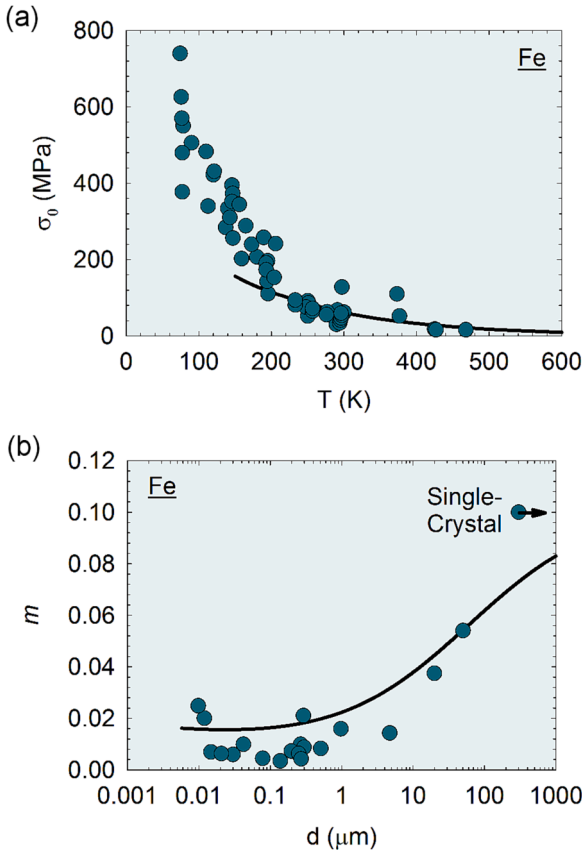

Fig. 30. Threshold stress for b.c.c. Fe estimated from Eq. (23) and experimental data [96,102–104,416,423–425] plotted as a function of temperature and (b) strain rate sensitivity estimated from the model of grain boundary sliding considering a thermally-activated threshold stress plotted as a function of grain size and data taken from the literature [236,396,406,423,426–429].

literature. The next section evaluates the behavior of Al-Mg and Mg-Al alloys for which numerous studies of high temperature behavior are now available.

9. An examination of high temperature behavior of some alloys

The general view of the effect of strain rate and temperature on the flow stress of materials with different grain sizes predicted by

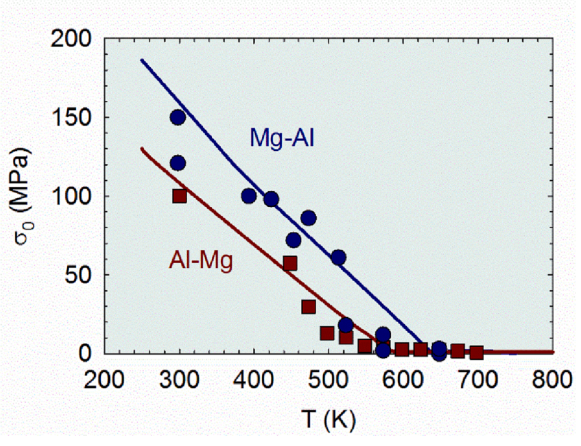

Fig. 31. Threshold stress estimated in experiments for Al-Mg [388,432] and for Mg-Al [68,106,433,434] alloys. The prediction of the threshold stress considering Eq. (14) is also shown for comparison.

the model of grain boundary sliding [50] was depicted in Fig. 24. In order to provide a qualitative and quantitative evaluation of these predictions, it is necessary to gather data from multiple sets of experiments in the literature. It is fair to say that the high temperature behavior of aluminum alloys and magnesium alloys have been extensively studied in recent years and there is a sufficient number of results for these materials. Therefore, the following analyses will focus on two groups of alloys, Al-Mg and Mg-Al. The commercial Mg-3 % Al-1 % Zn (AZ31) alloy is considered for the Mg-Al group since there are several studies for this alloy. However, the data were collected for a broader range of compositions for the Al-Mg group. It is important to remember that these alloys display significant threshold stresses at low and moderate temperatures. Therefore, a procedure similar to that adopted earlier for the CrMnFeCoNi alloy and Fe is used to provide an empirical description of the threshold stress.

Fig. 31 shows experimental data of the threshold stress for Al-Mg [388,432] alloys and for the Mg-Al [68,106,433,434] alloy. Both alloy groups seem to display a negligible threshold stress above a certain temperature. It follows, therefore, that Eq. (23) would tend to overestimate the threshold stress at high temperatures and thus it is necessary to adopt a different equation for the analysis. Following earlier reports [417,418,435], a different approximation was used to estimate the stress from Eq. (22) where the threshold stress was expressed as

$$\sigma_0 = \sigma_0^* \left(1 - \left(\frac{RT}{\Delta E} \ln \frac{\dot{\varepsilon}_0}{\dot{\varepsilon}} \right)^{2/3} \right) \tag{24}$$

Analysis shows that Eq. (24) has a significant disadvantage since it leads to negative values for the threshold stress at high temperatures and low strain rates. To avoid this ambiguity, a limiting threshold stress of 1 MPa for Al-Mg and 0.1 MPa for Mg-Al alloys was considered for situations where lower values were predicted. Also, a consideration of the threshold stress using Eq. (24) leads to some sharp steps in the σ vs $\dot{\varepsilon}$ plots. A detailed description of the threshold stress is out of the scope of the present analysis and therefore, for the sake of simplicity, Eq. (24) was used for the following analysis. The values of σ_0^* and ΔE considered in this analysis were 300 MPa and 87 kJ/mol for the Al-Mg alloys and 400 MPa and 98 kJ/mol for the Mg-Al alloys. The predictions from Eq. (24) for the Al-Mg and Mg-Al alloys are shown as continuous lines in Fig. 31.

Accordingly, the flow stresses predicted by Eq. (20), considering the threshold stress given by Eq. (24), are plotted for the Mg-Al alloy as a function of the strain rate for different temperatures and grain sizes in Fig. 32. Two grain sizes were selected for each temperature based on the availability of experimental data in the literature. Specifically, the finer grain sizes for each temperature are associated with white symbols and dashed lines while the coarser grain sizes are shown with filled symbols and continuous lines. Grain refinement hardening is predicted at room temperature, a transition from grain refinement hardening to grain refinement softening takes place at 423 K at low strain rates and grain refinement softening is observed at 723 K. There is a general agreement with the data from the literature [34,39,43,359,433] which supports the assumption of a gradual transition from grain refinement hardening to grain refinement softening with increasing temperature and decreasing strain rate.

An additional prediction by the model of grain boundary sliding is the occurrence of a gradual increase in the strain rate sensitivity of ultrafine-grained materials with increasing temperature. This is depicted in Fig. 33 which shows the flow stress predicted by the model for Al-Mg alloys, considering a thermally-activated threshold stress, plotted as a function of the strain rate for a large range of strain rates. The predictions consider ultrafine-grained samples tested at different temperatures. A gradual increase in slope, which is correlated to the strain rate sensitivity, is predicted with decreasing strain rate and with increasing temperature. The strain rate sensitivity tends to level off at ~ 0.5 giving rise to superplasticity. Data from the literature [432,436–438] are also plotted and show a good agreement with the predictions. It is especially interesting to note that the consideration of a threshold stress leads to a decrease in the slope of the curves at low strain rates and low stresses. This gives rise to a sigmoidal shape in the stress vs strain rate curves which agrees with experimental data as reported in very early experiments on a superplastic alloy [439]. Thus, the general view of the effect

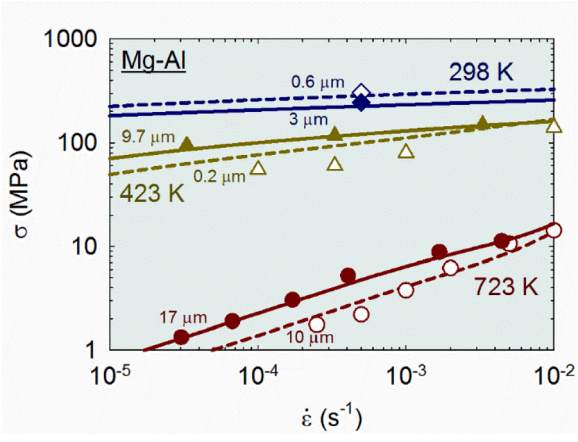

Fig. 32. Flow stress predicted by Eq. (20) considering the threshold stress predicted by Eq. (24) at different temperatures for the Mg-Al alloy with different grain sizes plotted as a function of the strain rate. Data taken from the literature [34,39,43,359,433] is shown for comparison.

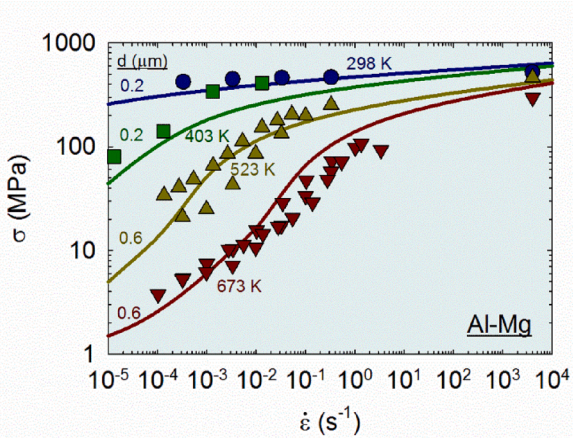

Fig. 33. Flow stress predicted by the model for ultrafine- grained Al-Mg alloys tested at different temperatures plotted as a function of the strain rate. Data from the literature is shown for comparison [432,436–438].

of temperature and strain rate on the flow stress depicted in Fig. 24 is supported by experimental observations.

10. The advent of extended ductility or quasi-superplasticity

The previous analysis shows that the model of grain boundary sliding can indeed predict the contribution of the grain size to the flow stress of different materials when tested at different temperatures and strain rates. It is expected that coarse-grained materials, with grain sizes larger than the stable sub-grain size, will undergo strain hardening and the deformation mechanism changes during deformation. However, in situations in which the grain size is smaller than the stable sub-grain size, strain hardening can be hindered and the material deforms under steady-state conditions. This situation is typical of creep and the mechanism of grain boundary sliding can predict the stress at which the material will flow provided the threshold stress is known.

A direct consequence of this analysis is the notion that the strain rate sensitivity can increase with decreasing grain size and that ultrafine-grained materials display a gradual increase in strain rate sensitivity with decreasing strain rate and with increasing temperature. This effect has been widely reported in the literature [232,382,386,404,431] and this is generally considered an effective strategy for overcoming the strength-ductility paradox [232,386,402,440–442].

The importance of the strain rate sensitivity for the ductility lies specifically in its importance in hindering localized deformation. This has a direct impact in elongations in tension since the necking evolution is affected by the development of localized deformation. A mathematical description of the effect of the strain rate sensitivity in the development of necking was given in a very early report [443]. In practice, the higher the strain rate sensitivity so the higher the elongation in tension and this was shown by data collected from multiple reports [444–446]. Fig. 34 shows a summary of elongations reported in tension plotted as a function of the strain rate sensitivity: the original data [444] are shown in gray filled symbols, recent data [40,72,73,75,122,232,353,386–388,402,419,436,437,447–472] were divided into tests at temperatures higher than 0.5 T_m (cyan filled symbols) and tests at $T < 0.5\ T_m$ (red filled symbols). It is clear that the strain rate sensitivity, m, affects the elongation and an

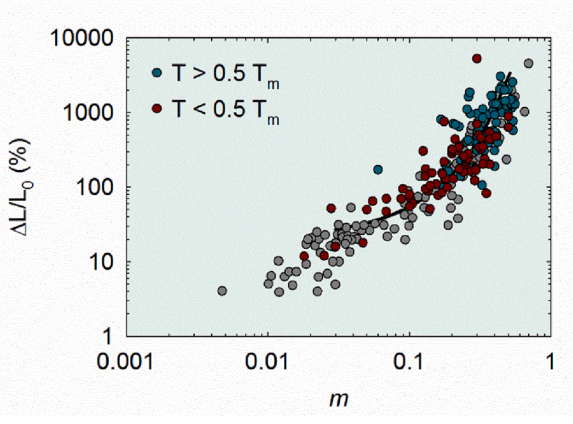

Fig. 34. Elongations in tension reported in the literature [40,72,73,75,122,232,353,386–388,402,419,436,437,444,447–470,473] plotted as a function of the strain rate sensitivity parameter, m.

empirical relationship of the type $\Delta L/L_0(\%) = 20e^{10m}$ is plotted as a continuous line.

A detailed observation of the data in Fig. 34 suggests that a value of m larger than ~ 0.4 and very high elongations, larger than ~ 1000 %, are mostly observed in high temperature testing. The data from tests at a low temperature ($T < 0.5\ T_m$) depicted in red symbols are primarily concentrated at m values lower than ~ 0.4 and the elongations are lower than ~ 1000 %. The model for grain boundary sliding [50] suggests that strain rate sensitivity values larger than ~ 0.4 should be observed at low temperatures provided the grain size is sufficiently small and the strain rate is sufficiently low. However, in practice at least two effects set difficulties for the success of this prediction. First, very small grain sizes tend to grow with heating and grain growth is observed in many materials at temperatures below $0.5T_m$. Second, solid solutions and second phase particles, which are used to prevent grain growth, can generate significant threshold stresses which thereby compromise the strain rate sensitivity.

In spite of the difficulties to expand the range of conventional superplasticity, with $m \approx 0.5$, to lower temperatures, there have been many reports of extraordinary elongations at $T < 0.5\ T_m$. For example, an early report [436] documented elongations over 100 % at 403 K (~0.43 T_m) in an Al-3 % Mg alloy with a grain size of ~ 200 nm. An elongation of 202 % was reported at 773 K (~0.43 T_m) in steel [454]. Also, an elongation of 300 % was reported at 623 K (~0.36 T_m) in electrodeposited Ni which had an as-processed grain size of only 20 nm [474] and later a superplastic elongation of 895 % was reported in electrodeposited Ni at 693 K (~0.4 T_m) [471]. Moreover, an extraordinary elongation of ~ 5300 % was reported at a high strain rate of 10^{-1} s^{-1} in electrodeposited Ni at 777 K (~0.45 T_m) [473]. The appearance of the specimen after pulling to failure is shown in Fig. 35.

Thus, examination of the data in Fig. 34 suggests elongations of > 100 % can be obtained in situations in which m is larger than ~ 0.15. This level of strain rate sensitivity and very high elongations are readily obtained at $T < 0.5\ T_m$. In fact, recent investigations have shown exceptional elongations at room temperature in materials with very small grain sizes. For example, an elongation of 510 % was reported at room temperature in a Zn-0.5 % Cu alloy [475]. Also, an elongation of 480 % was reported in an Al-30 % Zn alloy [73]. There are also many reports of high elongations in magnesium. Although coarse-grained magnesium can display brittle behavior, a recent report showed that grain refinement improves ductility in magnesium alloys [67]. An early report suggested also that the ductility could be enhanced significantly by decreasing the grain size in pure magnesium [476]. Furthermore, recent reports have confirmed this trend and experimental data [63,64,72,122,124,455,476–478] of the elongations of pure magnesium and some magnesium alloys (Mg-Li, Mg-Mn, Mg-Bi) are plotted as a function of the grain size in Fig. 36. It is clearly observed that exceptional ductilities arise in fine and ultrafine-grained magnesium at room temperature. This high ductility is also observed in compression [479] and even at high strain rates [123].

The phenomenon of superplasticity is widely established in the literature and has been defined as an elongation of at least 400 % and a strain rate sensitivity of ~ 0.5 [446]. It is known that superplasticity is controlled by grain boundary sliding and is usually observed at high temperatures in fine grained materials. The model for grain boundary sliding [50] incorporates the rate-controlling equation for high temperature superplasticity and also predicts steady-state deformation at low and moderate temperatures for polycrystals in which the grain is smaller than the stable sub-grain size. In these latter situations the model predicts, in agreement with the experimental data, different strain rate sensitivities which increase with decreasing grain size, decreasing strain rate and increasing temperature. Thus, it predicts strain rate sensitivities associated with elongations that may vary from a few percent up to extraordinary elongations over 100 %. This phenomenon, which can be called extended plasticity or quasi-superplasticity, has been reported in multiple materials with ultrafine-grained structure tested at low and moderate temperatures.

11. Other deformation mechanisms operating at low and moderate temperatures

The preceding analyses shows that the mechanism of grain boundary sliding [50] displays very good agreement with a broad range of experimental data for multiple materials tested over a range of different conditions. However, careful inspection of the data shows that other deformation mechanisms may prevail under specific conditions. An analysis of these disagreements and the possible contributions from diffusion creep mechanisms are now presented.

11.1. Twinning-controlled deformation

Some metals display significant contributions from twinning to the plastic deformation and this mechanism may control the flow stress under specific conditions. An example is shown in Fig. 37 in which σ vs $d^{-1/2}$ data [68,359–367] for magnesium alloy AZ31 is plotted. One set of results in which samples were compressed along the extrusion direction [68] is highlighted. This orientation seems to favor twinning and the data display a clear linear trend with a high slope. It is expected that, as the grain size decreases, the flow stress for slip-controlled deformation becomes lower and the alloy follows the slope predicted by the grain boundary sliding mechanism. This explains the multiple reports of high slopes in Mg and its alloys in the coarse-grained region. Twinning may also affect the flow stress of other materials such as Co [218].

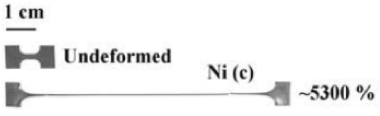

Fig. 35. Appearance of specimen of ultrafine grained Ni pulled to failure at ~ $0.45T_m$ at a high strain rate of 10^{-1} s^{-1} [473].

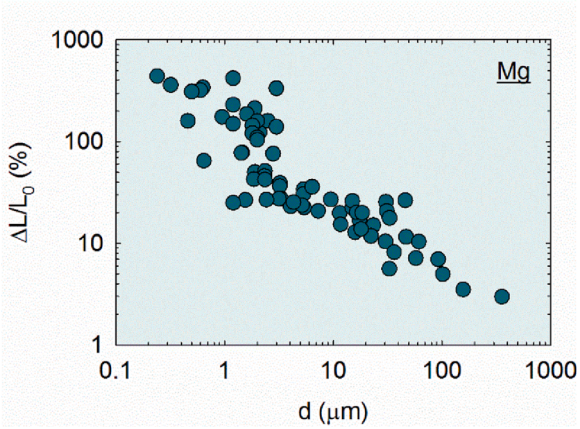

Fig. 36. Elongation to failure of pure Mg and some Mg alloys tested at room temperature plotted as a function of the grain size [63,64,72,122,124,455,476–478].

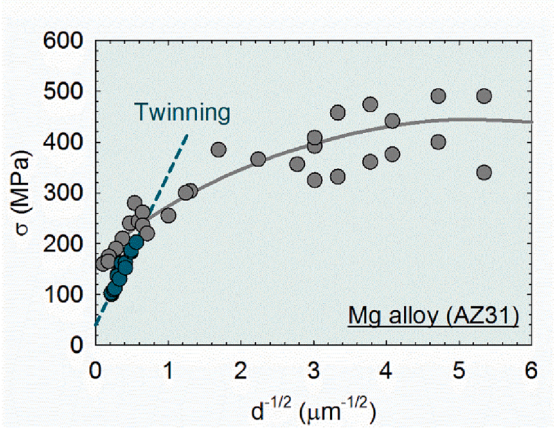

Fig. 37. Flow stress of magnesium alloy AZ31 [359–367] plotted as a function of $d^{-1/2}$ in which the data for twinning-controlled deformation [68] is highlighted.

11.2. A lower slope in some coarse-grained materials

Although the experimental data for pure aluminum demonstrate a good agreement with the model of grain boundary sliding for an extensive set of the results, a careful inspection of isolated sets in the coarse-grained region suggests a lower slope. This is illustrated in Fig. 38 in which the complete datum points [4–25] are displayed in (a) and a clearer view of the coarse-grained data is given in (b). The data from isolated sets of experiments [11,13,19,25] are highlighted and clearly show a reduced slope for grain sizes larger than ~ 10 μm. This reduced initial slope is followed by an increased slope and the data then tend to agree with the predictions from the model of grain boundary sliding at smaller grain sizes.

This change in slope has been reported in the literature [22–25,480] and it was recently shown that the addition of Mg as an alloying element decreases the range for this reduced slope [22]. Thus, the early reports of low Hall-Petch slopes in pure aluminum [26] may be attributed to the limited range of grain sizes evaluated. Recent experiments, in which finer grain sizes are considered, report K slopes in the range of 116–120 MPa $\mu m^{1/2}$ [22], 131 MPa $\mu m^{1/2}$ [24] and 215.6 MPa $\mu m^{1/2}$ [23] which tend to agree with the slopes of 116 MPa $\mu m^{1/2}$ and 142 MPa $\mu m^{1/2}$ predicted by the model of grain boundary sliding considering linear intercept and spatial grain sizes, respectively. This suggests that a different mechanism may control the flow stress of coarse-grained pure aluminum so that the grain boundary sliding mechanism controls the flow stress at grain sizes below ~ 10 μm and in aluminum alloys.

A similar effect was also reported in copper and the limiting grain size for the transition in slopes was estimated as ~ 3 μm [153]. A lower Hall-Petch slope in the coarse grained regime was also reported in IF steel [242] and Ni-Co and CoCrNi alloys [481]. An analysis of data for pure metals and alloys also suggests upward breaks in the Hall-Petch slope in Al, Cu and Mg [482].

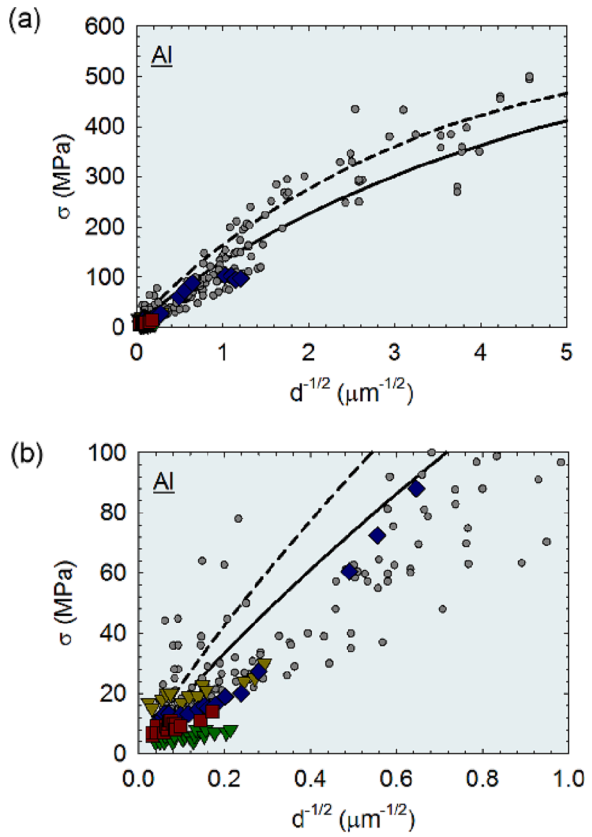

Fig. 38. Flow stress of aluminum plotted as a function of $d^{-1/2}$ considering (a) a broad range of grain sizes and (b) coarse grain sizes. Data taken from the literature [4–25] are shown and some experimental sets [11,13,19,25] are highlighted.

11.3. The significance of grain refinement softening and grain boundary stability

Grain refinement softening or an inverse Hall-Petch behavior has been observed in many metals and it is predicted by the model of grain boundary sliding under specific circumstances such as a high homologous temperature, low strain rates and very fine grains. Previous analyses showed examples of good agreement between the model and experimental data for multiple conditions. However, careful inspection of the data revealed some reports of grain refinement softening in conditions not predicted by the model, such as the occurrence of a few datum points in aluminum, zinc and magnesium.

A recent report [178] documented an inverse Hall-Petch behavior in electrodeposited Ni with Mo as an alloying element. The as-processed samples displayed a maximum hardness at a grain size of 10 nm and grain refinement softening at smaller grain sizes.

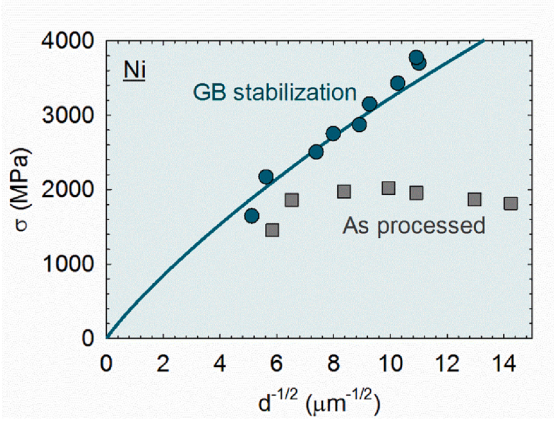

Fig. 39. Flow stress of nanocrystalline Ni-Mo alloys [178] before and after grain boundary stabilization.

However, stabilization of the grain boundaries by annealing at low temperatures caused an increase in hardness of the nanocrystalline Ni-Mo alloy. Fig. 39 shows the experimental data of hardness divided by 3 plotted as a function of $d^{-1\,2}$ [178]. The prediction from the model of grain boundary sliding [50] for Ni is also shown and there is good agreement between the model and the experimental data obtained in the samples in which the grain boundaries were stabilized.

It is interesting to note that mechanically driven grain coarsening was reported in the as-processed Ni-Mo alloy while grain coarsening was suppressed in the alloys in which the grain boundaries were stabilized [178]. This suggests that a different deformation mechanism with lower flow stress may be associated with grain boundary mobility. A decrease in hardness with concomitant grain growth was also reported in nanocrystalline copper [149]. This suggests a parallel to observations in pure Mg since grain coarsening was observed during room temperature deformation of ultrafine pure Mg processed by HPT [122].

A careful analysis of data from Mg shows that grain refinement softening can take place at grain sizes smaller than a few microns in samples processed from bulk pure Mg. However, magnesium samples produced from a consolidation of powders and Mg alloys do not appear to display grain refinement softening in this grain size range. Fig. 40 shows the flow stress of pure magnesium processed from bulk samples [64,66,122,261] (diamond gray symbols), pure Mg processed from a consolidation of powders [258,262,483] (square cyan symbols) and a magnesium alloy (AZ31) [359–367] (round red symbols) plotted as a function of $d^{-1/2}$. An inverse Hall-Petch behavior is observed in bulk Mg at grain sizes smaller than $\sim$ 1 μm while high flow stresses are observed in Mg processed from powders. It is expected that magnesium oxide is incorporated in the samples processed from powder consolidation and these particles may pin the grain boundaries preventing grain growth during deformation. Alloying elements can also hinder grain boundary migration and the data show good agreement between the Mg alloy and the model of grain boundary sliding. In fact, a recent paper reported negligible grain coarsening in a magnesium alloy with a grain size of $\sim$ 0.1 μm subjected to indentation creep at room temperature [115].

Stress-coupled grain growth was also observed in nanocrystalline aluminum [176,177]. In addition, grain refinement softening was reported in Al and it seems related to the purity level. Thus, softening was reported in Al with 99.99 % purity at grain sizes below $\sim$ 1 μm [22,24,25] and the softening was observed at grain sizes even larger in Al having 99.9999 % purity [71]. Such softening is not observed in commercial purity Al and Al alloys which also supports the assumption that grain boundary mobility plays a role in this effect.

11.4. The significance of diffusion creep

The increase in strain rate sensitivity and the change in slope in the Hall-Petch plots for ultrafine and nanocrystalline metals is sometimes attributed to a contribution from diffusion creep mechanisms. It is therefore interesting to evaluate the contributions of the Nabarro-Herring creep [30,31] and Coble creep [29] mechanisms. The rate controlling equations for these mechanisms are given as.

$$\dot{\varepsilon}_{NH} = 14\frac{D_l G b}{kT}\left(\frac{b}{d}\right)^{2}\left(\frac{\sigma}{G}\right)^{1} \tag{25}$$

and

$$\dot{\varepsilon}_{Coble} = 33.4\frac{\delta D_{gb} G}{kT}\left(\frac{b}{d}\right)^{3}\left(\frac{\sigma}{G}\right)^{1} \tag{26}$$

where D_l is the coefficient for lattice diffusion.

The mechanism of Coble creep is expected to play a major role in the deformation of metals with finer grain structures because of the higher grain size exponent. In order to discuss the contribution of diffusion creep, it is necessary to plot the predictions for conditions in which experimental data are available. Fig. 41 shows experimental data for an Al alloy tested at 403 K [436], a Cu alloy tested at 673 K [450] and a Mg alloy tested at 423 K [43]. These conditions were selected as they fall within the moderate temperature range for these materials. The grain sizes reported were $\sim$ 0.2 μm for the Al alloy and the Mg alloy and $\sim$ 1 μm for the Cu alloy and these are within the smallest grain sizes that are reasonably stable under these testing conditions. Thus, the flow stress predicted by Nabarro-Herring and Coble creep, considering the grain sizes and temperature, are plotted as a function of the strain rate. The prediction from the model of grain boundary sliding is also shown for comparison. These predictions included the contribution of the threshold stress, given by Eq. (24), estimated for Al-Mg and Mg-Al alloys. A zero temperature stress, σ_0^*, of 100 MPa and an activation energy, ΔE, of 100 kJ/mol were considered for the estimation of the threshold stress, using Eq. (23), for Cu alloys at high temperatures.

Inspection shows that, as expected, Nabarro-Herring creep should not contribute to deformation of the alloys for the conditions of testing. However, the predictions from Coble creep suggest this mechanism may play a major role in deformation of these materials. In fact, Coble creep should be rate-controlling for some of the testing conditions but nevertheless none of the conditions display the expected high slope in the stress vs strain rate plot. This suggests, therefore, that there is something hindering the operation of the Coble creep mechanism.

It has been suggested that some low energy boundaries may only act as sources and sinks for point defects above a critical threshold stress [484]. A threshold stress for diffusional creep was also considered in the analysis of data of low temperature tensile creep testing of electrodeposited Cu [485] although further creep testing in compression [486] failed to confirm the trend obtained in tension. It seems that, although the predictions from the rate equation for Coble creep suggest this mechanism should play a role in the deformation of ultrafine-grained materials especially at moderate temperatures, there is a lack of true experimental validation. A recent

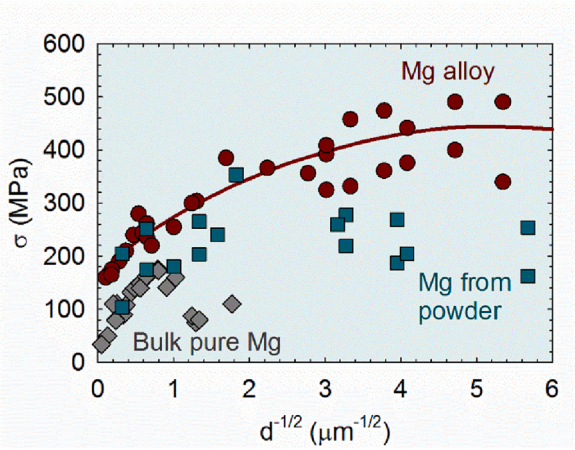

Fig. 40. Flow stress of pure magnesium processed from bulk samples [64,66,122,261], pure Mg processed from a consolidation of powders [258,262,483] and a magnesium alloy (AZ31) [359–367] plotted as a function of $d^{-1/2}$.

overview paper on creep of ultrafine-grained materials pointed out that grain growth can take place before and during creep testing [487] and this will undoubtedly affect the occurrence of diffusion creep. Nevertheless, it is important to note that the experimental data presented in Fig. 41 follow the predictions from the model of grain boundary sliding with fairly good agreement in terms of both the level of the flow stress and the slope of the data.

12. General evaluation of the grain boundary sliding mechanism

It was pointed out in the introduction to this review that it is widely accepted that the flow stress increases with decreasing grain size at low temperatures but the flow stress decreases with decreasing grain size at high temperatures. Although these opposite trends are usually treated separately, the present analysis demonstrates that the mechanism of grain boundary sliding [50] provides an adequate explanation for both effects. Accordingly, the general relationship between flow stress, grain size and temperature predicted by Eqs. (15) or (16) of the mechanism for grain boundary sliding is shown in a 3D graph in Fig. 42 by considering a constant strain rate. The flow stress and the grain size are plotted using arbitrary units on a logarithmic scale and the temperature is plotted in arbitrary units using a linear scale. Thus, at low temperatures the flow stress decreases with increasing grain size and the slope is ~ -0.5. This agrees with the assumption of $\sigma \propto d^{-1/2}$ which has been reported since almost 70 years ago. With increasing temperature, the flow stress of all grain sizes decreases but the rate of softening becomes more pronounced with decreasing grain size. As a consequence, heating causes a gradual transition in the relationship between flow stress and grain size such that at high temperatures the flow stress decreases with decreasing grain size. Eventually a relationship is observed in which the flow stress is directly proportional to the grain size at small grain sizes. This trend is also widely reported in the literature for superplastic materials and in fact the trends reported for low and high temperatures in Fig. 3 in the introduction are incorporated in the trend revealed by the model of grain boundary sliding now depicted in Fig. 42.

The previous sections showed that the phenomenology of the model of grain boundary sliding [50] is supported by experimental observations including offsets at grain boundaries during deformation, an emission of dislocations from grain boundaries, dislocation pile-ups, an increase in the vacancy density and the absorbing of dislocations at grain boundaries. Trends associated with the strain rate sensitivity and apparent activation volume predicted by the model also agree with experimental observations. However, the best evaluation of the rate-controlling mechanism is from the quantitative agreement with experimental data which was shown in multiple separate plots. In order to provide a comprehensive evaluation of the effectiveness of the model, the flow stress observed in multiple experiments are now plotted as a function of the theoretical flow stress predicted by the model in Fig. 43.

The inputs for the prediction of flow stress were the material fundamental properties (D_{gb}, G, b), the grain size of the sample, the testing strain rate and temperature and the threshold stress which incorporates the other hardening mechanisms. The room temperature threshold stresses were estimated from the best fits with experimental data as previously shown in Figs. 18–21. In order to provide evaluations of data from different strain rates and temperatures, the threshold stresses of CrMnFeCoNi, Cu alloys and Fe (b.c.c.) were estimated from Eq. (23) and the threshold stresses for Al and Mg alloys were estimated from Eq. (24) following the procedure described earlier. The experimental data were compared to either the flow stress predicted considering a spatial grain size in Eq. (19) or a mean linear intercept grain size in Eq. (20). A lower bound of grain size of 10 nm was considered for all materials except Zn for which the lower bound was 2 μm. An upper bound grain size of 10 μm was considered for the room temperature testing of Mg due to the occurrence of twinning in coarse-grained samples as discussed previously.

Accordingly, Fig. 43 includes the data depicted in Figs. 18-21 which contain flow stresses for the room temperature testing of Ag [200–206], Al [4–25], Au [207–210], Be [211–217], Bi alloy [75], Co [218,219], Cr [203,220–223], CrMnFeCoNi [339–352], Cu [95,121,150,151,153,154,156,157,159,224–235], Fe (b.c.c.) [61,96,102–104,236–248], Fe (f.c.c.) alloy [97,237,249–255], Hf

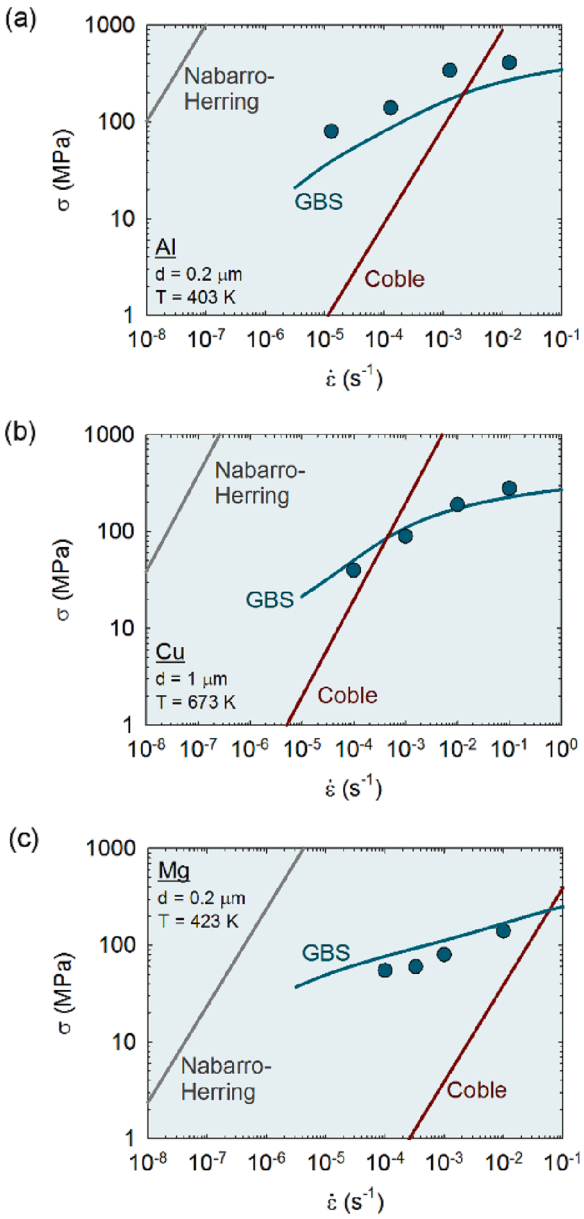

Fig. 41. Flow stress predicted by diffusion creep mechanisms and the mechanism of grain boundary sliding for (a) Al, (b), Cu and (c) Mg with fine-grained structures and tested at moderate temperatures plotted as a function of the strain rate. Experimental data from Al [436], Cu [450] and Mg [43] alloys tested under similar conditions are shown for comparison.

[256,257], Mg [63,64,66,105,110–112,258–262], Mo [263–270], Nb [79,271–281], Ni [3,178,282–292], Pb [293], Pd [293,294], Pt alloy [295,296], Re [297,298], Sn alloy [74,353,354], Ta [203,299,300], Ti (b.c.c.) alloy [101,301,302], Ti (h.c.p.) [100,303–314], U [192,338], V [269,300,315–320], W [321–324], Zn [51,70,325–329] and Zr [330–335]. It also includes data for room temperature testing of Al [22,355–358], Cu [153,158,166,368,369] and Mg [359–367] alloys and data from molecular dynamics simulations of Al [379,380] and Cu [141,378]. Data from high strain rate testing of CrMnFeCoNi [350,351] and an Al alloy [432], low and high temperature testing of the CrMnFeCoNi [339–341,343,344,346,348,404,408,419,421,488] alloy and high temperature testing of Al [432,436–438], Cu [450,489], Fe [98,99,469] and Mg [34,35,40,41,43,68,106,433,490–492] alloys are also included. The total number of experimental datum points is>2,300 and the range of flow stresses covers approximately 4 orders of magnitude.

A very good quantitative agreement is observed between the flow stress predicted by the model of grain boundary sliding and the values observed in experiments such that most of the points in Fig. 43 lie next to the central line which indicates perfect agreement. The great majority of the points lie within the gray lines that limit an agreement within a factor of 2. Furthermore, most of the points outside these gray lines are related to dispersions in experimental data for coarse-grained copper and aluminum since the difference in

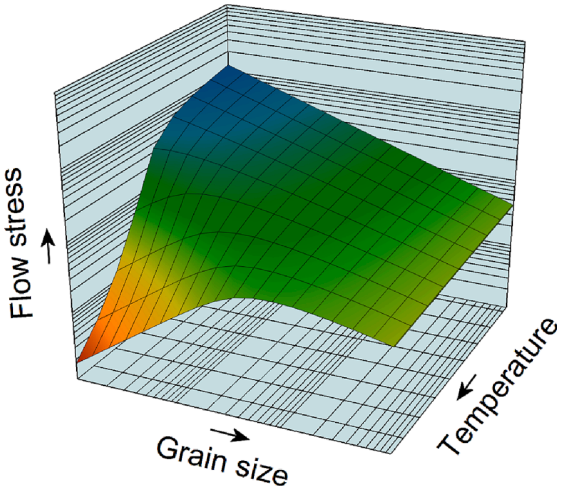

Fig. 42. General trend between the flow stress, grain size and temperature predicted by the model of grain boundary sliding [50].

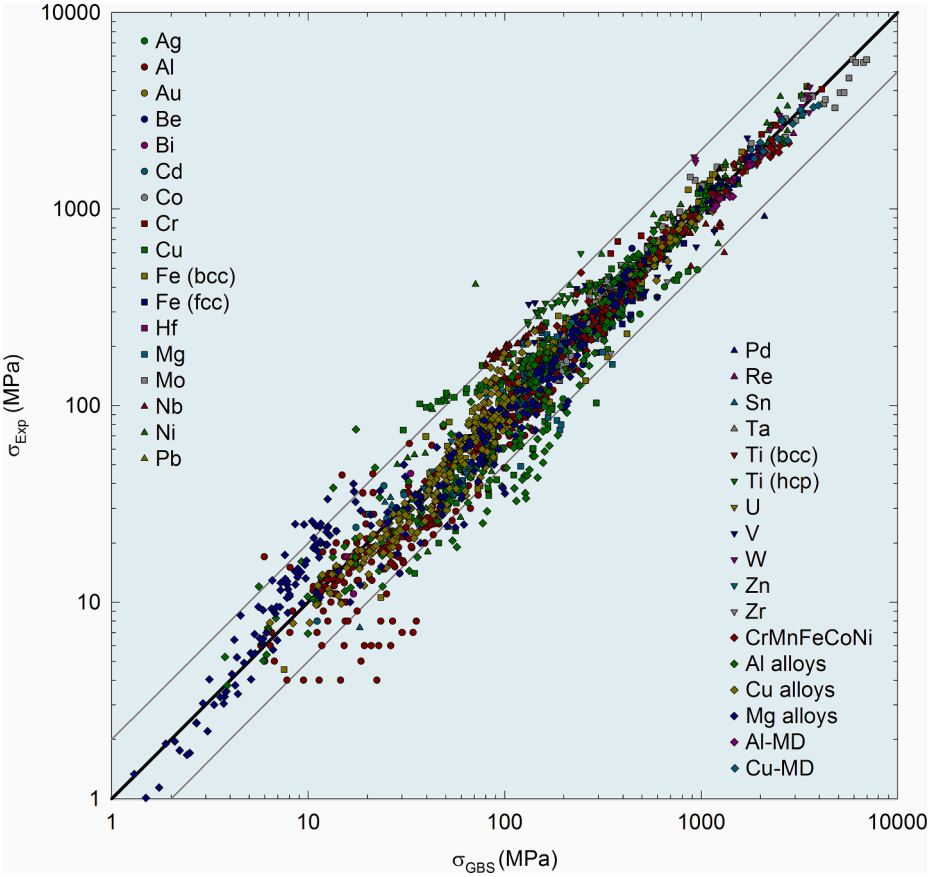

Fig. 43. Flow stress reported in experiments for a wide range of materials, grain sizes and testing conditions plotted as a function of the flow stress predicted by the mechanism of grain boundary sliding. Over 2300 datum points were included in this analysis and their description is given in the text.

flow stresses reported for these materials in the literature can reach up to one order of magnitude. Also, the empirical approximation considered for the threshold stresses of Al and Mg alloys can cause larger dispersions of the data such that some points appear outside the gray lines.

13. Concluding remarks

Many advances were made in recent decades on research regarding the relationship between the grain size and flow stress at low, moderate and high temperatures. Both the Hall-Petch relationship and superplasticity remain active topics of research even after many decades. Furthermore, the recent ability to produce nanocrystalline materials has led to great advances in the field despite the initial dispersion in data from different processing and characterization techniques. The advances in structural characterization, combined with the development of molecular dynamics simulations, has enabled the observation of deformation features both *ex situ* and *in situ*. Multiple trends were reviewed in the present study and they are discussed below.

It is not uncommon that the grain boundary strengthening contribution is considered athermal in analyses of the strength of metallic alloys or varies only based on the variation of G with temperature. On the contrary, the present review and much experimental evidence in the literature show it should be considered a thermally-activated contribution. Likewise, some analyses also consider the threshold stress as a constant which means an athermal contribution although there is now much evidence that it is thermally-activated. The notion that the flow stress can be the sum of more than one thermally-activated mechanism readily explains trends observed in the strain rate sensitivity and apparent activation volume at small grain sizes. The empirical correlation used in the present analysis for Al and Mg alloys permits an estimate of the threshold stress at different temperatures and strain rates and this is important in understanding trends taking place at moderate temperatures where both the grain size strengthening and the threshold stress play important roles. However, the dispersion of data demonstrates that it is not necessarily accurate for all conditions. This is expected especially in Al-Mg alloys which undergo dynamic strain ageing and therefore the relationship between the threshold stress and temperature is not straight forward.

A recent analysis [117] showed that the sum of the grain size strengthening and the threshold stress estimated by Eq. (16) for a multicomponent CrMnFeCoNi alloy provided a good quantitative agreement with experimental data and allowed an evaluation of the strain rate sensitivity, apparent activation volume and activation energy trends for different grain sizes, strain rates and temperatures. There have been studies on the analysis of the contribution of the solid solution to the threshold stress of alloys [417,418,435,493] and multicomponent alloys [194,346,494–496] and the values of the activation energy and zero temperature flow stress considered in the present analysis and elsewhere [117] for the CrMnFeCoNi alloy are in reasonable agreement with the values determined theoretically [346]. The overall and comprehensive analysis of data in Fig. 43 shows that the mechanism of grain boundary sliding [50] generally provides an excellent estimation of the effect of grain size on the flow stress for multiple materials and different strain rates and temperatures. Nevertheless, it is not expected that a single deformation mechanism will be rate-controlling for all materials and at all testing conditions independent of all structural features but the average grain size. Thus, some disagreements were already identified.

It was shown that the model of grain boundary sliding does not agree with experimental data under some specific conditions such as twinning-controlled deformation, some metals with coarse-grained structure and in situations in which grain boundary mobility plays a role (see Section 11). Other deformation mechanisms may prevail under these and other circumstances that will be disclosed by further research. Multiple models have been suggested in the literature to explain both the Hall-Petch effect and superplasticity. These different models have shown both agreement and disagreement with the experimental data. It is expected that further advances in structure characterization and a reduction in dispersion of the experimental data will clarify these deformation features and experimental trends and therefore it will become possible to better distinguish the deformation mechanisms operating under different conditions from low to high temperatures.

14. Summary and conclusions

1. The relationship between the grain size and the flow stress that has attracted so much attention for over 70 years is critically reviewed in light of recent advances in data and structural characterization and the development of a phenomenological model. This topic is usually treated within limited materials and temperature ranges but it is now expanded to include a broad set of over 30 metals and alloys and low, moderate and high temperatures. It is shown that one model [50] can indeed predict general trends under multiple conditions including computer molecular dynamics simulations. Some disagreement with specific trends are also documented.
2. Recent advances in structural characterization further clarify that grain boundary sliding, dislocation emission and absorption at grain boundaries, dislocation pile-ups and excess vacancies can be observed in ultrafine and nanocrystalline materials at room temperature. These observations support the phenomenological description of the model of grain boundary sliding.
3. Recent advances on mechanical characterization show that different trends are observed in plots of flow stress vs the inverse of the square root of the grain size in some materials. Many of these differences in trends are associated with the homologous temperature of testing. Also, an increased strain rate sensitivity and reduced apparent activation volume have been reported at very small grain sizes in some materials. A pronounced increase in strain rate sensitivity with increased temperature is also reported in ultrafine-grained materials and gives rise to extended ductility, quasi-superplasticity and even to true superplasticity. These trends are predicted and support the model of grain boundary sliding as the rate-controlling mechanism.
4. It is shown that the relationship between the flow stress and the grain size is thermally-activated. This notion permits a prediction of the relationship at different temperatures and strain rates. A thermally-activated description of the threshold stress complements the prediction and readily explains the trend of decreasing strain rate sensitivity with grain refinement reported in some materials.
5. A general description of the relationship between flow stress, grain size and temperature shows a gradual transition from grain refinement hardening at low temperatures to grain refinement softening at high temperatures. The analysis developed in this

review is quantitatively supported by >2,300 datum points from the literature for multiple materials, grain sizes, strain rates and temperatures.

Declaration of Competing Interest

The authors declare that they have no known competing financial interests or personal relationships that could have appeared to influence the work reported in this paper.

Data availability

Data will be made available on request.

Acknowledgements

This work was supported by CNPq (Grant #302445/2018-8) and FAPEMIG (Grant TEC-PPM-00324-17) (RBF), by the National Science Foundation of the United States under Grant No. CMMI-2051205 (MK) and by the European Research Council under ERC Grant Agreement No. 267464-SPDMETALS (TGL).

References

[1] Hall EO. The deformation and ageing of mild steel 3. Discussion of results. Proc Phys Soc Lond Sect B 1951;64:747–53.
[2] Petch NJ. The cleavage strength of polycrystals. J Iron Steel Inst 1953;174:25–8.
[3] Hughes GD, Smith SD, Pande CS, Johnson HR, Armstrong RW. Hall-Petch strengthening for the microhardness of twelve nanometer grain diameter electrodeposited nickel. Scr Metall 1986;20:93–7.
[4] Hayes RW, Witkin D, Zhou F, Lavernia EJ. Deformation and activation volumes of cryomilled ultrafine-grained aluminum. Acta Mater 2004;52:4259–71.
[5] Tsuji N, Okuno S, Matsuura T, Koizumi Y, Minamino Y. Mechanical properties as a function of grain size in ultrafine grained aluminum and iron fabricated by ARB and annealing process. Mater Sci Forum 2003;426–432:2667–72.
[6] Edalati K, Cubero-Sesin JM, Alhamidi A, Mohamed IF, Horita Z. Influence of severe plastic deformation at cryogenic temperature on grain refinement and softening of pure metals: Investigation using high-pressure torsion. Mater Sci Eng A 2014;613:103–10.
[7] Bachmaier A, Pippan R. Effect of oxide particles on the stabilization and final microstructure in aluminium. Mater Sci Eng A 2011;528:7589–95.
[8] Horita Z, Fujinami T, Nemoto M, Langdon TG. Equal-channel angular pressing of commercial aluminum alloys: Grain refinement, thermal stability and tensile properties. Metall Mater Trans A 2000;31:691–701.
[9] Huang Y, Bazarnik P, Wan D, Luo D, Pereira PHR, Lewandowska M, et al. The fabrication of graphene-reinforced Al-based nanocomposites using high-pressure torsion. Acta Mater 2019;164:499–511.
[10] Fujita H, Tabata T. The effect of grain size and deformation sub-structure on mechanical properties of polycrystalline aluminum. Acta Metall 1973;21:355–65.
[11] Hansen N. The effect of grain size and strain on the tensile flow stress of aluminium at room temperature. Acta Metall 1977;25:863–9.
[12] Wyrzykowski JW, Grabski MW. Effect of annealing temperature on structure and properties of fine-grained aluminium. Metal Sci 1983;17:445–50.
[13] Al-Haidary JT, Petch NJ, de los Rios ER. The plastic deformation of polycrystals I. Aluminium between room temperature and 400°C. Philos Mag A 1983;47:869–90.
[14] Tsuji N, Ito Y, Saito Y, Minamino Y. Strength and ductility of ultrafine grained aluminum and iron produced by ARB and annealing. Scr Mater 2002;47:893–9.
[15] Sato YS, Urata M, Kokawa H, Ikeda K. Hall-Petch relationship in friction stir welds of equal channel angular-pressed aluminium alloys. Mater Sci Eng A 2003;354:298–305.
[16] Yu CY, Kao PW, Chang CP. Transition of tensile deformation behaviors in ultrafine-grained aluminum. Acta Mater 2005;53:4019–28.
[17] Maung K, Earthman JC, Mohamed FA. Inverse Hall-Petch behavior in diamantane stabilized bulk nanocrystalline aluminum. Acta Mater 2012;60:5850–7.
[18] Sun PL, Cerreta EK, Gray GT, Bingert JF. The effect of grain size, strain rate, and temperature on the mechanical behavior of commercial purity aluminum. Metall Mater Trans A 2006;37:2983–94.
[19] Hansen N. Microstructure and and flow stress of aluminum and dispersion-strengthened aluminum aluminum-oxide products drawn at room temperature. Trans Metall Soc AIME 1969;245:2061–8.
[20] Hultgren F. Grain boundary + substructure hardening in aluminum. Trans Metall Soc AIME 1964;230:898–903.
[21] Choi HJ, Lee SW, Park JS, Bae DH. Tensile behavior of bulk nanocrystalline aluminum synthesized by hot extrusion of ball-milled powders. Scr Mater 2008;59:1123–6.
[22] Kamikawa N, Hirooka T, Furuhara T. Yielding behaviour and Hall-Petch relationship in ultrafine-grained Al–Mg binary alloys. Mater Sci Technol 2021;37:210–23.
[23] Balog M, Krizik P, Bajana O, Hu T, Yang H, Schoenung JM, et al. Influence of grain boundaries with dispersed nanoscale Al2O3 particles on the strength of Al for a wide range of homologous temperatures. J Alloy Compd 2019;772:472–81.
[24] Kamikawa N, Hirochi T, Furuhara T. Strengthening Mechanisms in Ultrafine-Grained and Sub-grained High-Purity Aluminum. Metall Mater Trans A 2019;50:234–48.
[25] Kamikawa N, Huang X, Tsuji N, Hansen N. Strengthening mechanisms in nanostructured high-purity aluminium deformed to high strain and annealed. Acta Mater 2009;57:4198–208.
[26] Wyrzykowski JW, Grabski MW. The Hall-Petch relation in aluminium and its dependence on the grain boundary structure. Philos Mag A 1986;53:505–20.
[27] Bird JE, Mukherjee AK, Dorn JE. Quantitative relation between properties and microstructure. Jerusalem, Israel: Israel Universities Press; 1969. p. 255–342.
[28] Blum W, Zeng XH. A simple dislocation model of deformation resistance of ultrafine-grained materials explaining Hall-Petch strengthening and enhanced strain rate sensitivity. Acta Mater 2009;57:1966–74.
[29] Coble RL. A model for boundary diffusion controlled creep in polycrystalline materials. J Appl Phys 1963;34:1679–82.
[30] Nabarro FRN. Deformation of crystals by the motion of single ions. Report of a conference on strength of solids. London, U.K: The Physical Society; 1948. p. 75–90.
[31] Herring C. Diffusional viscosity of a polycrystalline solid. J Appl Phys 1950;21:437–45.
[32] Langdon TG. Grain boundary sliding revisited: Developments in sliding over four decades. J Mater Sci 2006;41:597–609.
[33] Langdon TG. A unified approach to grain boundary sliding in creep and superplasticity. Acta Metall Mater 1994;42:2437–43.
[34] Figueiredo RB, Langdon TG. Developing superplasticity in a magnesium AZ31 alloy by ECAP. J Mater Sci 2008;43:7366–71.
[35] Figueiredo RB, Langdon TG. Evaluating the superplastic flow of a magnesium AZ31 alloy processed by equal-channel angular pressing. Metall Mater Trans A 2014;45:3197–204.
[36] Figueiredo RB, Langdon TG. Analysis of the creep behavior of fine-grained AZ31 magnesium alloy. Mater Sci Eng A 2020;787:139489.

[37] Somekawa H, Hosokawa H, Watanabe H, Higashi K. Diffusion bonding in superplastic magnesium alloys. Mater Sci Eng A 2003;339:328–33.
[38] del Valle JA, Pérez-Prado MT, Ruano OA. Deformation mechanisms responsible for the high ductility in a Mg AZ31 alloy analyzed by electron backscattered diffraction. Metall Mater Trans A 2005;36:1427–38.
[39] Figueiredo RB, Langdon TG. Grain refinement and mechanical behavior of a magnesium alloy processed by ECAP. J Mater Sci 2010;45:4827–36.
[40] Lin HK, Huang JC, Langdon TG. Relationship between texture and low temperature superplasticity in an extruded AZ31 Mg alloy processed by ECAP. Mater Sci Eng A 2005;402:250–7.
[41] Lin HK, Huang JC. High strain rate and/or low temperature superplasticity in AZ31 Mg alloys processed by simple high-ratio extrusion methods. Mater Trans 2002;43:2424–32.
[42] Panicker MRR, Chokshi AH. Influence of grain size on high temperature fracture in a Mg AZ31 alloy. Mater Sci Eng A 2011;528:3031–6.
[43] Xu J, Wang XW, Shirooyeh M, Xing GN, Shan DB, Guo B, et al. Microhardness, microstructure and tensile behavior of an AZ31 magnesium alloy processed by high-pressure torsion. J Mater Sci 2015;50:7424–36.
[44] Pearson C. The viscous properties of extruded eutectic alloys of lead-tin and bismuth-tin. J Inst Metals. 1934;54:111–24.
[45] Langdon TG. An evaluation of the strain contributed by grain boundary sliding in superplasticity. Mater Sci Eng A 1994;174:225–30.
[46] Ball A, Hutchison MM. Superplasticity in the Aluminium-Zinc Eutectoid. Metal Science Journal. 1969;3:1–7.
[47] Mukherjee AK. The rate controlling mechanism in superplasticity. Mater Sci Eng 1971;8:83–9.
[48] Eshelby JD, Frank FC, Nabarro FRN. XLI. The equilibrium of linear arrays of dislocations. Lond Edinburgh Dublin Philos Mag J Sci 1951;42:351–64.
[49] Friedel J. Dislocations. Oxford, U.K.: Pergamon Press; 1964.
[50] Figueiredo RB, Langdon TG. Deformation mechanisms in ultrafine-grained metals with an emphasis on the Hall-Petch relationship and strain rate sensitivity. J Mater Res Technol 2021;14:137–59.
[51] Armstrong R, Codd I, Douthwaite RM, Petch NJ. The plastic deformation of polycrystalline aggregates. Philos Mag: J Theor Exp Appl Phys 1962;7:45–58.
[52] Hansen N. Polycrystalline strengthening. Metall Trans A 1985;16:2167–90.
[53] Armstrong RW. The influence of polycrystal grain size on several mechanical properties of materials. Metall Mater Trans B 1970;1:1169–76.
[54] Cottrell AH. Theory of brittle fracture in steel and similar metals. Trans Met Soc AIME. 1958;212:192–203.
[55] Cordero ZC, Knight BE, Schuh CA. Six decades of the Hall-Petch effect – a survey of grain-size strengthening studies on pure metals. Int Mater Rev 2016;61:495–512.
[56] Naik SN, Walley SM. The Hall-Petch and inverse Hall-Petch relations and the hardness of nanocrystalline metals. J Mater Sci 2020;55:2661–81.
[57] Armstrong RW. 60 Years of Hall-Petch: Past to Present Nano-Scale Connections. Mater Trans 2014;55:2–12.
[58] Balasubramanian N, Langdon TG. The strength–grain size relationship in ultrafine-grained metals. Metall Mater Trans A 2016;47:5827–38.
[59] Ralston KD, Birbilis N, Davies CHJ. Revealing the relationship between grain size and corrosion rate of metals. Scr Mater 2010;63:1201–4.
[60] Li JCM, Chou YT. The role of dislocations in the flow stress grain size relationships. Metall Mater Trans B 1970;1:1145.
[61] Tejedor R, Edalati K, Benito JA, Horita Z, Cabrera JM. High-pressure torsion of iron with various purity levels and validation of Hall-Petch strengthening mechanism. Mater Sci Eng A 2019;743:597–605.
[62] Meyers MA, Mishra A, Benson DJ. Mechanical properties of nanocrystalline materials. Prog Mater Sci 2006;51:427–556.
[63] Somekawa H, Mukai T. Hall-Petch breakdown in fine-grained pure magnesium at low strain rates. Metall Mater Trans A 2015;46:894–902.
[64] Zheng R, Du J-P, Gao S, Somekawa H, Ogata S, Tsuji N. Transition of dominant deformation mode in bulk polycrystalline pure Mg by ultra-grain refinement down to sub-micrometer. Acta Mater 2020;198:35–46.
[65] Castro MM, Pereira PHR, Isaac A, Langdon TG, Figueiredo RB. Inverse Hall-Petch behaviour in an AZ91 alloy and in an AZ91–Al2O3 composite consolidated by high-pressure torsion. Adv Eng Mater 2020;22:1900894.
[66] Zheng R, Gong W, Du J-p, Gao S, Liu M, Li G, et al. Rediscovery of Hall-Petch strengthening in bulk ultrafine grained pure Mg at cryogenic temperature: A combined in-situ neutron diffraction and electron microscopy study. Acta Mater 2022;238:118243.
[67] Carvalho AP, Figueiredo RB. An Overview of the effect of grain size on mechanical properties of magnesium and its alloys. Mater Trans 2023. advpub.
[68] Barnett MR, Keshavarz Z, Beer AG, Atwell D. Influence of grain size on the compressive deformation of wrought Mg–3Al–1Zn. Acta Mater 2004;52:5093–103.
[69] Mohamed FA, Yang H. Deformation mechanisms in nanocrystalline materials. Metall Mater Trans A 2010;41:823–37.
[70] Naziri H, Pearce R. The effect of grain size on workhardening and superplasticity in Zn/0.4% A1 alloy. Scr Metall 1969;3:811–4.
[71] Ito Y, Edalati K, Horita Z. High-pressure torsion of aluminum with ultrahigh purity (99.9999%) and occurrence of inverse Hall-Petch relationship. Mater Sci Eng A 2017;679:428–34.
[72] Edalati K, Masuda T, Arita M, Furui M, Sauvage X, Horita Z, et al. Room-temperature superplasticity in an ultrafine-grained magnesium alloy. Sci Rep 2017;7:2662.
[73] Edalati K, Horita Z, Valiev RZ. Transition from poor ductility to room-temperature superplasticity in a nanostructured aluminum alloy. Sci Rep 2018;8:6740.
[74] Lin K, Li Z, Liu Y, Ma E, Wang JT, Langdon TG. Exploiting tube high-pressure shearing to prepare a microstructure in Pb-Sn alloys for unprecedented superplasticity. Scr Mater 2022;209:114390.
[75] Wang CT, He Y, Langdon TG. The significance of strain weakening and self-annealing in a superplastic Bi–Sn eutectic alloy processed by high-pressure torsion. Acta Mater 2020;185:245–56.
[76] Li JCM, Liu GCT. Circular dislocation pile-ups. Philos Mag: J Theor Exp Appl Phys 1967;15:1059–63.
[77] Armstrong RW. Hall-Petch description of nanopolycrystalline Cu, Ni and Al strength levels and strain rate sensitivities. Phil Mag 2016;96:3097–108.
[78] Ashby MF. The deformation of plastically non-homogeneous materials. Philos Mag: J Theor Exp Appl Phys 1970;21:399–424.
[79] Conrad H, Feuerstein S, Rice L. Effects of grain size on the dislocation density and flow stress of niobium. Mater Sci Eng 1967;2:157–68.
[80] Conrad H. Effect of grain size on the lower yield and flow stress of iron and steel. Acta Metall 1963;11:75–7.
[81] Meyers MA, Ashworth E. A model for the effect of grain size on the yield stress of metals. Philos Mag A 1982;46:737–59.
[82] Cannon WR, Langdon TG. Creep of ceramics. J Mater Sci 1988;23:1–20.
[83] Twiss RJ. Theory and applicability of a recrystallized grain size paleopiezometer. Pure Appl Geophys 1977;115:227–44.
[84] White S. Grain and sub-grain size variations across a mylonite zone. Contrib Miner Petrol 1979;70:193–202.
[85] Conrad H. Grain size dependence of the plastic deformation kinetics in Cu. Mater Sci Eng A 2003;341:216–28.
[86] Conrad H, Narayan J. Mechanisms for grain size hardening and softening in Zn. Acta Mater 2002;50:5067–78.
[87] Chinh NQ, Olasz D, Ahmed AQ, Sáfrán G, Lendvai J, Langdon TG. Modification of the Hall-Petch relationship for submicron-grained fcc metals. Mater Sci Eng A 2023;862:144419.
[88] Kim HS, Estrin Y, Bush MB. Plastic deformation behaviour of fine-grained materials. Acta Mater 2000;48:493–504.
[89] Kim HS, Estrin Y, Bush MB. Constitutive modelling of strength and plasticity of nanocrystalline metallic materials. Mater Sci Eng A 2001;316:195–9.
[90] Kim HS, Estrin Y. Phase mixture modeling of the strain rate dependent mechanical behavior of nanostructured materials. Acta Mater 2005;53:765–72.
[91] Chokshi AH, Rosen A, Karch J, Gleiter H. On the validity of the hall-petch relationship in nanocrystalline materials. Scr Metall 1989;23:1679–83.
[92] Carlton CE, Ferreira PJ. What is behind the inverse Hall-Petch effect in nanocrystalline materials? Acta Mater 2007;55:3749–56.
[93] Mohamed FA, Chauhan M. Interpretation of the creep behavior of nanocrystalline Ni in terms of dislocation accommodated boundary sliding. Metall Mater Trans A 2006;37:3555–67.
[94] Mohamed FA. Correlation between the Deformation of Nanostructured Materials and the Model of Dislocation Accommodated Boundary Sliding. Metall Mater Trans A 2008;39:470–2.
[95] Ono N, Karashima S. Grain size dependence of flow stress in copper polycrystals. Scr Metall 1982;16:381–4.
[96] Hutchison MM. The temperature dependence of the yield stress of polycrystalline iron. Philos Mag: J Theor Exp Appl Phys 1963;8:121–7.
[97] Kashyap BP, Tangri K. On the Hall-Petch relationship and substructural evolution in type 316L stainless steel. Acta Metall Mater 1995;43:3971–81.
[98] Dingley DJ, McLean D. Components of the flow stress of iron. Acta Metall 1967;15:885–901.

[99] Brindley BJ, Barnby JT. Dynamic strain ageing in mild steel. Acta Metall 1966;14:1765–80.
[100] Okazaki K, Conrad H. Effects of interstitial content and grain size on the strength of titanium at low temperatures. Acta Metall 1973;21:1117–29.
[101] Chia K-H, Jung K, Conrad H. Dislocation density model for the effect of grain size on the flow stress of a Ti–15.2 at.% Mo β-alloy at 4.2–650K. Mater Sci Eng A 2005;409:32–8.
[102] Petch NJ. The ductile-brittle transition in the fracture of α-iron: I. Philos Mag: J Theor Exp Appl Phys 1958;3:1089–97.
[103] Heslop J, Petch NJ. LXXXVIII. The stress to move a free dislocation in alpha iron. Philos Mag: J Theor Exp Appl Phys 1956;1:866–73.
[104] Conrad H, Schoeck G. Cottrell locking and the flow stress in iron. Acta Metall 1960;8:791–6.
[105] Ono N, Nowak R, Miura S. Effect of deformation temperature on Hall-Petch relationship registered for polycrystalline magnesium. Mater Lett 2004;58:39–43.
[106] Atwell DL, Barnett MR, Hutchinson WB. The effect of initial grain size and temperature on the tensile properties of magnesium alloy AZ31 sheet. Mater Sci Eng A 2012;549:1–6.
[107] Panin VE, Moiseenko DD, Elsukova TF. Multiscale model of deformed polycrystals. Hall-Petch problem. Physical Mesomechanics. 2014;17:1–14.
[108] Panin VE, Armstrong RW. Hall-Petch analysis for temperature and strain rate dependent deformation of polycrystalline lead. Phys Mesomech 2016;19:35–40.
[109] Hauser FE, Landon PR, Dorn JE. Fracture of magnesium alloys at low temperature. Trans Am Inst Min Metall Eng 1956;206:589–93.
[110] Rao GS, Prasad YVRK. Grain boundary strengthening in strongly textured magnesium produced by hot rolling. Metall Trans A 1982;13:2219–26.
[111] Wilson DV, Chapman JA. Effects of preferred orientation on the grain size dependence of yield strength in metals. Philos Mag 1963;8:1543–51.
[112] Wilson DV. Ductility of polycrystalline magnesium below 300 K. J Inst Met 1970;98:133–43.
[113] Li Y, Bushby AJ, Dunstan DJ. The Hall-Petch effect as a manifestation of the general size effect. Proc R Soc: Math Phys Eng Sci 2016;472:20150890.
[114] Figueiredo RB, Edalati K, Langdon TG. Effect of creep parameters on the steady-state flow stress of pure metals processed by high-pressure torsion. Mater Sci Eng A 2022;835:142666.
[115] Carvalho AP, Figueiredo RB. The effect of ultragrain refinement on the strength and strain rate sensitivity of a ZK60 magnesium alloy. Adv Eng Mater 2022;24:2100846.
[116] Figueiredo RB, Langdon TG. Effect of grain size on strength and strain rate sensitivity in metals. J Mater Sci 2022;57:5210–29.
[117] Figueiredo RB, Wolf W, Langdon TG. Effect of grain size on strength and strain rate sensitivity in the CrMnFeCoNi high-entropy alloy. J Mater Res Technol 2022;20:2358.
[118] Thompson AW. Calculation of true volume grain diameter. Metallography 1972;5:366–9.
[119] Falk LKL, Howell PR, Dunlop GL, Langdon TG. The role of matrix dislocations in the superplastic deformation of a copper alloy. Acta Metall 1986;34:1203–14.
[120] Chinh NQ, Szommer P, Horita Z, Langdon TG. Experimental evidence for grain-boundary sliding in ultrafine-grained aluminum processed by severe plastic deformation. Adv Mater 2006;18:34–9.
[121] Valiev RZ, Kozlov EV, Ivanov YF, Lian J, Nazarov AA, Baudelet B. Deformation behaviour of ultra-fine-grained copper. Acta Metall Mater 1994;42:2467–75.
[122] Figueiredo RB, Sabbaghianrad S, Giwa A, Greer JR, Langdon TG. Evidence for exceptional low temperature ductility in polycrystalline magnesium processed by severe plastic deformation. Acta Mater 2017;122:322–31.
[123] Somekawa H, Singh A, Sahara R, Inoue T. Excellent room temperature deformability in high strain rate regimes of magnesium alloy. Sci Rep 2018;8:656.
[124] Somekawa H, Singh A, Mukai T, Inoue T. Effect of alloying elements on room temperature tensile ductility in magnesium alloys. Phil Mag 2016;96:2671–85.
[125] Chinh NQ, Valiev RZ, Sauvage X, Varga G, Havancsák K, Kawasaki M, et al. Grain boundary phenomena in an ultrafine-grained Al–Zn alloy with improved mechanical behavior for micro-devices. Adv Eng Mater 2014;16:1000–9.
[126] Wang L, Teng J, Liu P, Hirata A, Ma E, Zhang Z, et al. Grain rotation mediated by grain boundary dislocations in nanocrystalline platinum. Nat Commun 2014;5:4402.
[127] Li H, Gao S, Tomota Y, Ii S, Tsuji N, Ohmura T. Mechanical response of dislocation interaction with grain boundary in ultrafine-grained interstitial-free steel. Acta Mater 2021;206:116621.
[128] Youssef KM, Scattergood RO, Murty KL, Horton JA, Koch CC. Ultrahigh strength and high ductility of bulk nanocrystalline copper. Appl Phys Lett 2005;87:091904.
[129] Kumar KS, Suresh S, Chisholm MF, Horton JA, Wang P. Deformation of electrodeposited nanocrystalline nickel. Acta Mater 2003;51:387–405.
[130] Setman D, Schafler E, Korznikova E, Zehetbauer MJ. The presence and nature of vacancy type defects in nanometals detained by severe plastic deformation. Mater Sci Eng A 2008;493:116–22.
[131] Divinski SV, Reglitz G, Rösner H, Estrin Y, Wilde G. Ultra-fast diffusion channels in pure Ni severely deformed by equal-channel angular pressing. Acta Mater 2011;59:1974–85.
[132] Schafler E, Steiner G, Korznikova E, Kerber M, Zehetbauer MJ. Lattice defect investigation of ECAP-Cu by means of X-ray line profile analysis, calorimetry and electrical resistometry. Mater Sci Eng A 2005;410–411:169–73.
[133] Würschum R, Oberdorfer B, Steyskal E-M, Sprengel W, Puff W, Pikart P, et al. Free volumes in bulk nanocrystalline metals studied by the complementary techniques of positron annihilation and dilatometry. Phys B Condens Matter 2012;407:2670–5.
[134] Oberdorfer B, Setman D, Steyskal E-M, Hohenwarter A, Sprengel W, Zehetbauer M, et al. Grain boundary excess volume and defect annealing of copper after high-pressure torsion. Acta Mater 2014;68:189–95.
[135] Cao WQ, Gu CF, Pereloma EV, Davies CHJ. Stored energy, vacancies and thermal stability of ultra-fine grained copper. Mater Sci Eng A 2008;492:74–9.
[136] Oberdorfer B, Lorenzoni B, Unger K, Sprengel W, Zehetbauer M, Pippan R, et al. Absolute concentration of free volume-type defects in ultrafine-grained Fe prepared by high-pressure torsion. Scr Mater 2010;63:452–5.
[137] Čížek J, Janeček M, Vlasák T, Smola B, Melikhova O, Islamgaliev RK, et al. The Development of Vacancies during Severe Plastic Deformation. Mater Trans 2019;60:1533–42.
[138] Yamakov V, Wolf D, Phillpot SR, Mukherjee AK, Gleiter H. Dislocation processes in the deformation of nanocrystalline aluminium by molecular-dynamics simulation. Nat Mater 2002;1:45–9.
[139] Yamakov V, Wolf D, Salazar M, Phillpot SR, Gleiter H. Length-scale effects in the nucleation of extended dislocations in nanocrystalline Al by molecular-dynamics simulation. Acta Mater 2001;49:2713–22.
[140] Van Swygenhoven H, Derlet PM, Frøseth AG. Nucleation and propagation of dislocations in nanocrystalline fcc metals. Acta Mater 2006;54:1975–83.
[141] Schiøtz J, Jacobsen KW. A maximum in the strength of nanocrystalline copper. Science 2003;301:1357–9.
[142] Farkas D, Frøseth A, Van Swygenhoven H. Grain boundary migration during room temperature deformation of nanocrystalline Ni. Scr Mater 2006;55:695–8.
[143] Millett PC, Desai T, Yamakov V, Wolf D. Atomistic simulations of diffusional creep in a nanocrystalline body-centered cubic material. Acta Mater 2008;56:3688–98.
[144] Schiøtz J, Di Tolla FD, Jacobsen KW. Softening of nanocrystalline metals at very small grain sizes. Nature 1998;391:561–3.
[145] Schiøtz J, Vegge T, Di Tolla FD, Jacobsen KW. Atomic-scale simulations of the mechanical deformation of nanocrystalline metals. Phys Rev B 1999;60:11971–83.
[146] Van Swygenhoven H, Spaczer M, Caro A, Farkas D. Competing plastic deformation mechanisms in nanophase metals. Phys Rev B 1999;60:22–5.
[147] Van Swygenhoven H, Spaczer M, Caro A. Microscopic description of plasticity in computer generated metallic nanophase samples: a comparison between Cu and Ni. Acta Mater 1999;47:3117–26.
[148] Tabor D. A simple theory of static and dynamic hardness. Proc R Soc Lond Ser A-Math Phys Sci 1948;192:247–74.
[149] Zhang K, Weertman JR, Eastman JA. Rapid stress-driven grain coarsening in nanocrystalline Cu at ambient and cryogenic temperatures. Appl Phys Lett 2005;87:061921.
[150] Hayashi K, Etoh H. Pressure sintering of iron, cobalt, nickel and copper ultrafine powders and the crystal grain size and hardness of the compacts. Mater Trans JIM 1989;30:925–31.
[151] Morris DG, Morris MA. Microstructure and strength of nanocrystalline copper alloy prepared by mechanical alloying. Acta Metall Mater 1991;39:1763–70.

[152] Edalati K, Bachmaier A, Beloshenko VA, Beygelzimer Y, Blank VD, Botta WJ, et al. Nanomaterials by severe plastic deformation: review of historical developments and recent advances. Mater Res Lett 2022;10:163–256.
[153] Tian YZ, Ren YP, Gao S, Zheng RX, Wang JH, Pan HC, et al. Two-stage Hall-Petch relationship in Cu with recrystallized structure. J Mater Sci Technol 2020;48:31–5.
[154] Jenei P, Yoon EY, Gubicza J, Kim HS, Lábár JL, Ungár T. Microstructure and hardness of copper–carbon nanotube composites consolidated by High Pressure Torsion. Mater Sci Eng A 2011;528:4690–5.
[155] An XH, Wu SD, Zhang ZF, Figueiredo RB, Gao N, Langdon TG. Enhanced strength-ductility synergy in nanostructured Cu and Cu-Al alloys processed by high-pressure torsion and subsequent annealing. Scr Mater 2012;66:227–30.
[156] Haouaoui M, Karaman I, Maier HJ, Hartwig KT. Microstructure evolution and mechanical behavior of bulk copper obtained by consolidation of micro- and nanopowders using equal-channel angular extrusion. Metall Mater Trans A 2004;35A:2935–49.
[157] Flinn JE, Field DP, Korth GE, Lillo TM, Macheret J. The flow stress behavior of OFHC polycrystalline copper. Acta Mater 2001;49:2065–74.
[158] Huang CX, Hu W, Yang G, Zhang ZF, Wu SD, Wang QY, et al. The effect of stacking fault energy on equilibrium grain size and tensile properties of nanostructured copper and copper–aluminum alloys processed by equal channel angular pressing. Mater Sci Eng A 2012;556:638–47.
[159] Jiang H, Zhu YT, Butt DP, Alexandrov IV, Lowe TC. Microstructural evolution, microhardness and thermal stability of HPT-processed Cu. Mater Sci Eng A 2000;290:128–38.
[160] Chen J, Lu L, Lu K. Hardness and strain rate sensitivity of nanocrystalline Cu. Scr Mater 2006;54:1913–8.
[161] Nieman GW, Weertman JR, Siegel RW. Mechanical behavior of nanocrystalline Cu and Pd. J Mater Res 2011;6:1012–27.
[162] Sanders PG, Eastman JA, Weertman JR. Elastic and tensile behavior of nanocrystalline copper and palladium. Acta Mater 1997;45:4019–25.
[163] Yu H, Xin Y, Wang M, Liu Q. Hall-Petch relationship in Mg alloys: A review. J Mater Sci Technol 2018;34:248–56.
[164] Wang Y, Choo H. Influence of texture on Hall-Petch relationships in an Mg alloy. Acta Mater 2014;81:83–97.
[165] Guan B, Xin Y, Huang X, Wu P, Liu Q. Quantitative prediction of texture effect on Hall-Petch slope for magnesium alloys. Acta Mater 2019;173:142–52.
[166] Meakin JD, Petch NJ. Strain-hardening of polycrystals: The α-brasses. Philos Mag: J Theor Exp Appl Phys 1974;29:1149–56.
[167] Tabor D. The hardness of metals. Oxford, U.K.: Clarendon Press; 1951.
[168] Zhang P, Li SX, Zhang ZF. General relationship between strength and hardness. Mater Sci Eng A 2011;529:62–73.
[169] Nix WD, Gao H. Indentation size effects in crystalline materials: A law for strain gradient plasticity. J Mech Phys Solids 1998;46:411–25.
[170] Zhang Y, Karnati S, Pan T, Liou F. Determination of constitutive relation from miniature tensile test with digital image correlation. J Strain Anal Eng Des 2020;55:99–108.
[171] Kumar K, Pooleery A, Madhusoodanan K, Singh RN, Chakravartty JK, Dutta BK, et al. Use of miniature tensile specimen for measurement of mechanical properties. Proc Eng 2014;86:899–909.
[172] Torbati-Sarraf SA, Alizadeh R, Mahmudi R, Langdon TG. Evaluating the flow properties of a magnesium ZK60 alloy processed by high-pressure torsion: a comparison of two different miniature testing techniques. Mater Sci Eng A 2017;708:432–9.
[173] Carvalho AP, Reis LM, Pinheiro RPRP, Pereira PHR, Langdon TG, Figueiredo RB. Using plane strain compression test to evaluate the mechanical behavior of magnesium processed by HPT. Metals. 2022;12:125.
[174] Mohebbi MS, Akbarzadeh A, Yoon Y-O, Kim S-K. Flow stress analysis of ultrafine grained AA 1050 by plane strain compression test. Mater Sci Eng A 2014;593:136–44.
[175] Williams RE. Space-filling polyhedron: its relation to aggregates of soap bubbles, plant cells, and metal crystallites. Science 1968;161:276–7.
[176] Legros M, Gianola DS, Hemker KJ. In situ TEM observations of fast grain-boundary motion in stressed nanocrystalline aluminum films. Acta Mater 2008;56:3380–93.
[177] Gianola DS, Warner DH, Molinari JF, Hemker KJ. Increased strain rate sensitivity due to stress-coupled grain growth in nanocrystalline Al. Scr Mater 2006;55:649–52.
[178] Hu J, Shi YN, Sauvage X, Sha G, Lu K. Grain boundary stability governs hardening and softening in extremely fine nanograined metals. Science 2017;355:1292–6.
[179] Wang K, Liu FC, Xue P, Wang D, Xiao BL, Ma ZY. Superplastic constitutive equation including percentage of high-angle grain boundaries as a microstructural parameter. Metall Mater Trans A 2016;47:546–59.
[180] Liu FC, Ma ZY, Zhang FC. High strain rate superplasticity in a micro-grained Al–Mg–Sc alloy with predominant high angle grain boundaries. J Mater Sci Technol 2012;28:1025–30.
[181] Liu FC, Xue P, Ma ZY. Microstructural evolution in recrystallized and unrecrystallized Al–Mg–Sc alloys during superplastic deformation. Mater Sci Eng A 2012;547:55–63.
[182] Zhou X, Li XY, Lu K. Stabilizing nanograins in metals with grain boundary relaxation. Scr Mater 2020;187:345–9.
[183] Xu W, Zhang B, Du K, Li XY, Lu K. Thermally stable nanostructured Al-Mg alloy with relaxed grain boundaries. Acta Mater 2022;226:117640.
[184] Lehto P, Remes H, Saukkonen T, Hänninen H, Romanoff J. Influence of grain size distribution on the Hall-Petch relationship of welded structural steel. Mater Sci Eng A 2014;592:28–39.
[185] Buch A. Short handbook of metal elements properties and elastic properties of pure metals. 3rd ed. Warsaw: Krzysztof Biesaga; 2005.
[186] Buch A. Pure metals properties, a scientific-technical handbook. London and Tel Aviv: ASM International/Freund Publishing House; 1999.
[187] Metals Handbook. Properties and selection of nonferrous alloys and special-purpose materials. Ohio: ASM International, Metals Park; 1990.
[188] Cullity BD. Elements of X-ray diffraction. 2nd ed. London: Addison-Wesley; 1978.
[189] Frost HJ, Ashby MF. Deformation-mechanism maps: the plasticity and creep of metals and ceramics. Oxford, U.K: Pergamon Press; 1982.
[190] Brown AM, Ashby MF. Correlations for diffusion constants. Acta Metall 1980;28:1085–101.
[191] Herzig C, Divinski S, Mishin Y. Bulk and interface boundary diffusion in group IV hexagonal close-packed metals and alloys. Metall Mater Trans A 2002;33:765–75.
[192] Liu F, Zhao Y, Yuan Z, Li F, Zou D, Wang W, et al. Formation of nanostructures in α-uranium processed by high pressure torsion. Mater Sci Eng A 2022;849:143442.
[193] Laplanche G, Gadaud P, Horst O, Otto F, Eggeler G, George EP. Temperature dependencies of the elastic moduli and thermal expansion coefficient of an equiatomic, single-phase CoCrFeMnNi high-entropy alloy. J Alloy Compd 2015;623:348–53.
[194] Varvenne C, Luque A, Curtin WA. Theory of strengthening in fcc high entropy alloys. Acta Mater 2016;118:164–76.
[195] Vaidya M, Pradeep KG, Murty BS, Wilde G, Divinski SV. Radioactive isotopes reveal a non sluggish kinetics of grain boundary diffusion in high entropy alloys. Sci Rep 2017;7:12293.
[196] Glienke M, Vaidya M, Gururaj K, Daum L, Tas B, Rogal L, et al. Grain boundary diffusion in CoCrFeMnNi high entropy alloy: Kinetic hints towards a phase decomposition. Acta Mater 2020;195:304–16.
[197] Vaidya M, Trubel S, Murty BS, Wilde G, Divinski SV. Ni tracer diffusion in CoCrFeNi and CoCrFeMnNi high entropy alloys. J Alloy Compd 2016;688:994–1001.
[198] Gust W, Mayer S, Bögel A, Predel B. Generalized representation of grain boundary self-diffusion data. J Phys Colloques 1985;46:C4-537–4-544.
[199] Migliori A, Ledbetter H, Thoma DJ, Darling TW. Beryllium's monocrystal and polycrystal elastic constants. J Appl Phys 2004;95:2436–40.
[200] Aldrich JW, Armstrong RW. The grain size dependence of the yield, flow and fracture stress of commercial purity silver. Metall Trans 1970;1:2547–50.
[201] Carreker RP. Tensile deformation of silver as a function of temperature, strain rate, and grain size. Trans Am Inst Min Metall Eng 1957;209:112–5.
[202] Kizuka T, Ichinose H, Ishida Y. Structure and hardness of nanocrystalline silver. J Mater Sci 1997;32:1501–7.
[203] Edalati K, Horita Z. High-pressure torsion of pure metals: Influence of atomic bond parameters and stacking fault energy on grain size and correlation with hardness. Acta Mater 2011;59:6831–6.
[204] Gubicza J, Chinh NQ, Lábár JL, Hegedűs Z, Xu C, Langdon TG. Microstructure and yield strength of severely deformed silver. Scr Mater 2008;58:775–8.
[205] Kobelev NP, Soifer YM, Andrievski RA, Gunther B. Microhardness and elastic properties of nanocrystalline silver. Nanostruct Mater 1993;2:537–44.

[206] Qin XY, Wu XJ, Zhang LD. The microhardness of nanocrystalline silver. Nanostruct Mater 1995;5:101–10.
[207] Matsunaga H, Horita Z. Softening and microstructural coarsening without twin formation in FCC metals with low stacking fault energy after processing by high-pressure torsion. Mater Trans 2009;50:1633–7.
[208] Emery RD, Povirk GL. Tensile behavior of free-standing gold films Part I. Coarse-grained films. Acta Mater 2003;51:2067–78.
[209] Emery RD, Povirk GL. Tensile behavior of free-standing gold films. Part II. Fine-grained films. Acta Mater 2003;51:2079–87.
[210] Gubicza J, Chinh NQ, Szommer P, Vinogradov A, Langdon TG. Microstructural characteristics of pure gold processed by equal-channel angular pressing. Scr Mater 2007;56:947–50.
[211] Khristenko IN, Papirov II, Tikhinskii GF. Effect of structural factors on the yield strength of beryllium. Met Sci Heat Treat 1976;18:597–600.
[212] Webster D, Greene RL, Lawley RW. Factors controlling the strength and ductility of high purity beryllium block. Metall Mater Trans B 1974;5:91.
[213] Gelles S, Nerses V, Siergiej JM. Beryllium as a Structural Material. JOM 1963;15:843–8.
[214] Odegard Jr BC. Influence of purity level on the mechanical properties of hot isostatically pressed beryllium. Report No. SAND-79-8232. Sandia Laboratories: Livermore CA, USA; 1979. p. 18.
[215] Kardashev BK, Kupriyanov IB. Elastic, micro- and macroplastic properties of polycrystalline beryllium. Phys Solid State 2011;53:2480–5.
[216] London GJ, Keith GH, Pinto NP. Grain-size and oxide content affect Beryllium's properties. Metals Eng Q 1976;16:45–57.
[217] Levine ED, Pemsler JP, Gelles SH. Characteristics of vacuum-distilled beryllium. J Nucl Mater 1964;12:40–9.
[218] Fleurier G, Hug E, Martinez M, Dubos P-A, Keller C. Size effects and Hall-Petch relation in polycrystalline cobalt. Philos Mag Lett 2015;95:122–30.
[219] Edalati K, Toh S, Arita M, Watanabe M, Horita Z. High-pressure torsion of pure cobalt: hcp-fcc phase transformations and twinning during severe plastic deformation. Appl Phys Lett 2013;102:181902.
[220] Marcinkowski MJ, Lipsitt HA. The plastic deformation of chromium at low temperatures. Acta Metall 1962;10:95–111.
[221] Brittain CP, Armstrong RW, Smith GC. Hall-Petch dependence for ultrafine grain size electrodeposited chromium. Scr Metall 1985;19:89–91.
[222] Provenzano V, Valiev R, Rickerby DG, Valdre G. Mechanical properties of nanostructured chromium. Nanostruct Mater 1999;12:1103–8.
[223] Wu D, Zhang J, Huang JC, Bei H, Nieh TG. Grain-boundary strengthening in nanocrystalline chromium and the Hall-Petch coefficient of body-centered cubic metals. Scr Mater 2013;68:118–21.
[224] Feltham P, Meakin JD. On the mechanism of work hardening in face-centred cubic metals, with special reference to polycrystalline copper. Philos Mag: J Theor Exp Appl Phys 1957;2:105–12.
[225] Thompson AW, Baskes MI. The influence of grain size on the work hardening of face-center cubic polycrystals. Philos Mag: J Theor Exp Appl Phys 1973;28:301–8.
[226] Merz MD, Dahlgren SD. Tensile strength and work hardening of ultrafine-grained high-purity copper. J Appl Phys 1975;46:3235–7.
[227] Hansen N, Ralph B. The strain and grain size dependence of the flow stress of copper. Acta Metall 1982;30:411–7.
[228] Carreker RP, Hibbard WR. Tensile deformation of high-purity copper as a function of temperature, strain rate, and grain size. Acta Metall 1953;1:654–63.
[229] Gertsman VY, Hoffmann M, Gleiter H, Birringer R. The study of grain size dependence of yield stress of copper for a wide grain size range. Acta Metall Mater 1994;42:3539–44.
[230] Thompson AW, Backofen WA. Production and mechanical behavior of very fine-grained copper. Metall Trans 1971;2:2004–5.
[231] Tian YZ, Gao S, Zhao LJ, Lu S, Pippan R, Zhang ZF, et al. Remarkable transitions of yield behavior and Lüders deformation in pure Cu by changing grain sizes. Scr Mater 2018;142:88–91.
[232] Wang YM, Ma E. Three strategies to achieve uniform tensile deformation in a nanostructured metal. Acta Mater 2004;52:1699–709.
[233] Gubicza J, Dobatkin SV, Khosravi E, Kuznetsov AA, Lábár JL. Microstructural stability of Cu processed by different routes of severe plastic deformation. Mater Sci Eng A 2011;528:1828–32.
[234] Zhilyaev AP, Swaminathan S, Gimazov AA, McNelley TR, Langdon TG. An evaluation of microstructure and microhardness in copper subjected to ultra-high strains. J Mater Sci 2008;43:7451–6.
[235] Schafler E, Kerber MB. Microstructural investigation of the annealing behaviour of high-pressure torsion (HPT) deformed copper. Mater Sci Eng A 2007;462:139–43.
[236] Batista BA, Soares RB, Lins VFC, Figueiredo RB, Hohenwarter A, Matencio T. Corrosion in Hank's solution and mechanical strength of ultrafine-grained pure iron. Adv Eng Mater 2020;22:2000183.
[237] Takaki S, Kawasaki K, Kimura Y. Mechanical properties of ultra fine grained steels. J Mater Process Technol 2001;117:359–63.
[238] Cracknell A, Petch NJ. Frictional forces on dislocation arrays at the lower yield point in iron. Acta Metall 1955;3:186–9.
[239] Tjerkstra HH. The effect of grain size on the stress-strain curve of α-iron and the connection with the plastic deformation of the grain boundaries. Acta Metall 1961;9:259–63.
[240] Jago RA, Hansen N. Grain size effects in the deformation of polycrystalline iron. Acta Metall 1986;34:1711–20.
[241] Butler JF. Lüders front propagation in low carbon steels. J Mech Phys Solids 1962;10:313–8.
[242] Gao S, Chen M, Joshi M, Shibata A, Tsuji N. Yielding behavior and its effect on uniform elongation in IF steel with various grain sizes. J Mater Sci 2014;49:6536–42.
[243] Muñoz JA, Higuera OF, Expósito AH, Boulaajaj A, Bolmaro RE, Dumitru FD, et al. Thermal stability of ARMCO iron processed by ECAP. Int J Adv Manuf Technol 2018;98:2917–32.
[244] Hohenwarter A, Kammerhofer C, Pippan R. The ductile to brittle transition of ultrafine-grained Armco iron: an experimental study. J Mater Sci 2010;45:4805–12.
[245] Valiev RZ, Ivanisenko Y, Rauch EF, Baudelet B. Structure and deformaton behaviour of Armco iron subjected to severe plastic deformation. Acta Mater 1996;44:4705–12.
[246] Wetscher F, Vorhauer A, Stock R, Pippan R. Structural refinement of low alloyed steels during severe plastic deformation. Mater Sci Eng A 2004;387–389:809–16.
[247] Edalati K, Fujioka T, Horita Z. Evolution of mechanical properties and microstructures with equivalent strain in pure Fe processed by high pressure torsion. Mater Trans 2009;50:44–50.
[248] Muñoz JA, Higuera OF, Benito JA, Bradai D, Khelfa T, Bolmaro RE, et al. Analysis of the micro and substructural evolution during severe plastic deformation of ARMCO iron and consequences in mechanical properties. Mater Sci Eng A 2019;740–741:108–20.
[249] Astafurov SV, Maier GG, Melnikov EV, Moskvina VA, Panchenko MY, Astafurova EG. The strain-rate dependence of the Hall-Petch effect in two austenitic stainless steels with different stacking fault energies. Mater Sci Eng A 2019;756:365–72.
[250] Kashyap BP, Tangri K. On the Hall-Petch relationship in type 316L stainless steel at room temperature. Scr Metall Mater 1990;24:1777–82.
[251] Nakao Y, Miura H. Nano-grain evolution in austenitic stainless steel during multi-directional forging. Mater Sci Eng A 2011;528:1310–7.
[252] Varin RA, Kurzydlowski KJ. The effects of nitrogen content and twin boundaries on the yield strength of various commercial heats of type 316 austenitic stainless steel. Mater Sci Eng A 1988;101:221–6.
[253] Odnobokova M, Belyakov A, Enikeev N, Molodov DA, Kaibyshev R. Annealing behavior of a 304L stainless steel processed by large strain cold and warm rolling. Mater Sci Eng A 2017;689:370–83.
[254] Mine Y, Horita N, Horita Z, Takashima K. Effect of ultrafine grain refinement on hydrogen embrittlement of metastable austenitic stainless steel. Int J Hydrogen Energy 2017;42:15415–25.
[255] Shakhova I, Dudko V, Belyakov A, Tsuzaki K, Kaibyshev R. Effect of large strain cold rolling and subsequent annealing on microstructure and mechanical properties of an austenitic stainless steel. Mater Sci Eng A 2012;545:176–86.
[256] Cerreta E, Yablinsky CA, Gray GT, Vogel SC, Brown DW. The influence of grain size and texture on the mechanical response of high purity hafnium. Mater Sci Eng A 2007;456:243–51.
[257] Edalati K, Horita Z, Mine Y. High-pressure torsion of hafnium. Mater Sci Eng A 2010;527:2136–41.

[258] Choi HJ, Kim Y, Shin JH, Bae DH. Deformation behavior of magnesium in the grain size spectrum from nano- to micrometer. Mater Sci Eng A 2010;527:1565–70.
[259] Li J, Xu W, Wu X, Ding H, Xia K. Effects of grain size on compressive behaviour in ultrafine grained pure Mg processed by equal channel angular pressing at room temperature. Mater Sci Eng A 2011;528:5993–8.
[260] Caceres CH, Mann GE, Griffiths JR. Grain Size Hardening in Mg and Mg-Zn Solid Solutions. Metall Mater Trans A 2011;42:1950–9.
[261] Silva CLP, Oliveira AC, Costa CGF, Figueiredo RB, de Fátima LM, Pereira MM, et al. Effect of severe plastic deformation on the biocompatibility and corrosion rate of pure magnesium. J Mater Sci 2017;52:5992–6003.
[262] Ren R, Fan J, Wang B, Zhang Q, Li W, Dong H. Hall-Petch relationship and deformation mechanism of pure Mg at room temperature. J Alloy Compd 2022;920:165924.
[263] Johnson AA. The effect of grain size on the tensile properties of high-purity molybdenum at room temperature. Philos Mag: J Theor Exp Appl Phys 1959;4:194–9.
[264] Wronski AS, Johnson AA. The deformation and fracture properties of polycrystalline molybdenum. Philos Mag: J Theor Exp Appl Phys 1962;7:213–27.
[265] Sherman MA, Bunshah RF, Beale HA. High-rate physical vapor deposition of refractory metals. J Vac Sci Technol 1975;12:697–703.
[266] McNally CM, Kao WH, Nieh TG. The effect of potassium doping on the strength of molybdenum. Scr Metall 1988;22:1847–50.
[267] Yoder KB, Elmustafa AA, Lin JC, Hoffman RA, Stone DS. Activation analysis of deformation in evaporated molybdenum thin films. J Phys D Appl Phys 2003;36:884–95.
[268] Imgram AG, Spretnak JW, Ogden HR. Effect of metallurgical structure on tensile + notch-tensile properties of molybdenum + Mo-0.5Ti. Trans Metall Soc AIME 1964;230:1345–52.
[269] Lee S, Edalati K, Horita Z. Microstructures and Mechanical Properties of Pure V and Mo Processed by High-Pressure Torsion. Mater Trans 2010;51:1072–9.
[270] Duan FH, Naunheim Y, Schuh CA, Li Y. Breakdown of the Hall-Petch relationship in extremely fine nanograined body-centered cubic Mo alloys. Acta Mater 2021;213:116950.
[271] Omar AM, Entwisle AR. The effect of grain size on the deformation of niobium. Mater Sci Eng 1970;5:263–70.
[272] Szkopiak ZC. The Hall-Petch parameters of niobium determined by the grain size and extrapolation methods. Mater Sci Eng 1972;9:7–13.
[273] Churchman AT. Cleavage fracture in niobium. J Inst Met 1960;88:221–2.
[274] Popova EN, Popov VV, Romanov EP, Pilyugin VP. Thermal stability of nanocrystalline Nb produced by severe plastic deformation. Phys Met Metallogr 2006;101:52–7.
[275] Popov VV, Popova EN, Stolbovskii AV, Pilyugin VP, Arkhipova NK. Nanostructurization of Nb by high-pressure torsion in liquid nitrogen and the thermal stability of the structure obtained. Phys Met Metallogr 2012;113:295–301.
[276] Popova EN, Popov VV, Romanov EP, Pilyugin VP. Effect of the degree of deformation on the structure and thermal stability of nanocrystalline niobium produced by high-pressure torsion. Phys Met Metallogr 2007;103:407–13.
[277] Evans PRV, Weinberg AF, van Thyne RJ. Irradiation hardening in columbium. Acta Metall 1963;11:143–50.
[278] Wilcox BA, Huggins RA. Effect of hydrogen on dislocation locking in niobium. J Less Common Metals 1960;2:292–303.
[279] Adams MA, Roberts AC, Smallman RE. Yield and fracture in polycrystalline niobium. Acta Metall 1960;8:328–37.
[280] Johnson AA. The low temperature tensile properties of niobium. Acta Metall 1960;8:737–40.
[281] Lee S, Horita Z. High-pressure torsion for pure chromium and niobium. Mater Trans 2012;53:38–45.
[282] Zhang HW, Huang X, Pippan R, Hansen N. Thermal behavior of Ni (99.967% and 99.5% purity) deformed to an ultra-high strain by high pressure torsion. Acta Mater 2010;58:1698–707.
[283] Bachmaier A, Hohenwarter A, Pippan R. New procedure to generate stable nanocrystallites by severe plastic deformation. Scr Mater 2009;61:1016–9.
[284] Krasilnikov N, Lojkowski W, Pakiela Z, Valiev R. Tensile strength and ductility of ultra-fine-grained nickel processed by severe plastic deformation. Mater Sci Eng A 2005;397:330–7.
[285] Dalla Torre F, Spätig P, Schäublin R, Victoria M. Deformation behaviour and microstructure of nanocrystalline electrodeposited and high pressure torsioned nickel. Acta Mater 2005;53:2337–49.
[286] Floreen S, Westbrook JH. Grain boundary segregation and the grain size dependence of strength of nickel-sulfur alloys. Acta Metall 1969;17:1175–81.
[287] Nakada Y, Keh AS. Solid-solution strengthening in Ni-C alloys. Metall Trans 1971;2:441–7.
[288] Wilcox BA, Clauer AH. The role of grain size and shape in strengthening of dispersion hardened nickel alloys. Acta Metall 1972;20:743–57.
[289] Thompson AAW. Yielding in nickel as a function of grain or cell size. Acta Metall 1975;23:1337–42.
[290] El-Sherik AM, Erb U, Palumbo G, Aust KT. Deviations from hall-petch behaviour in as-prepared nanocrystalline nickel. Scr Metall Mater 1992;27:1185–8.
[291] Knapp JA, Follstaedt DM. Hall-Petch relationship in pulsed-laser deposited nickel films. J Mater Res 2011;19:218–27.
[292] Zhou X, Feng Z, Zhu L, Xu J, Miyagi L, Dong H, et al. High-pressure strengthening in ultrafine-grained metals. Nature 2020;579:67–72.
[293] Edalati K, Horita Z. Significance of homologous temperature in softening behavior and grain size of pure metals processed by high-pressure torsion. Mater Sci Eng A 2011;528:7514–23.
[294] Ivanisenko Y, Kurmanaeva L, Weissmueller J, Yang K, Markmann J, Rösner H, et al. Deformation mechanisms in nanocrystalline palladium at large strains. Acta Mater 2009;57:3391–401.
[295] Renk O, Hohenwarter A, Maier-Kiener V, Pippan R. Exploring the anneal hardening phenomenon in nanocrystalline Pt-Ru alloys. J Alloy Compd 2023;935:168005.
[296] Battaini P. Microstructure analysis of selected platinum alloys. Platin Met Rev 2011;55:74–83.
[297] Mito M, Matsui H, Tsuruta K, Yamaguchi T, Nakamura K, Deguchi H, et al. Large enhancement of superconducting transition temperature in single-element superconducting rhenium by shear strain. Sci Rep 2016;6:36337.
[298] Wei Z, Zhang L, Li X, Long Y, Qu X. Effect of grain size on deformation behavior of pure rhenium. Mater Sci Eng A 2022;829:142170.
[299] Huang Y, Maury N, Zhang NX, Langdon TG. Microstructures and mechanical properties of pure tantalum processed by high-pressure torsion. IOP Conf Ser: Mater Sci Eng 2014;63:012100.
[300] Jankowski AF, Go J, Hayes JP. Thermal stability and mechanical behavior of ultra-fine bcc Ta and V coatings. Surf Coat Technol 2007;202:957–61.
[301] Janeček M, Čížek J, Stráský J, Václavová K, Hruška P, Polyakova V, et al. Microstructure evolution in solution treated Ti15Mo alloy processed by high pressure torsion. Mater Charact 2014;98:233–40.
[302] Gatina S, Semenova I, Leuthold J, Valiev R. Nanostructuring and Phase Transformations in the β-Alloy Ti-15Mo during High-Pressure Torsion. Adv Eng Mater 2015;17:1742–7.
[303] Hu H, Cline RS. Mechanism of reorientation during recrystallization of polycrystalline titanium. Trans Metall Soc AIME 1968;242:1013–24.
[304] Lederich RJ, Sastry SML, O'Neal JE, Rath BB. The effect of grain size on yield stress and work hardening of polycrystalline titanium at 295 K and 575 K. Mater Sci Eng 1978;33:183–8.
[305] Popov AA, Pyshmintsev IY, Demakov SL, Illarionov AG, Lowe TC, Sergeyeva AV, et al. Structural and mechanical properties of nanocrystalleve titanium processed by severe plastic deformation. Scr Mater 1997;37:1089–94.
[306] Sergueeva AV, Stolyarov VV, Valiev RZ, Mukherjee AK. Advanced mechanical properties of pure titanium with ultrafine grained structure. Scr Mater 2001;45:747–52.
[307] Hyun C-Y, Lee J-H, Kim H-K. Microstructures and mechanical properties of ultrafine grained pure Ti produced by severe plastic deformation. Res Chem Intermed 2010;36:629–38.
[308] Ghaderi A, Barnett MR. Sensitivity of deformation twinning to grain size in titanium and magnesium. Acta Mater 2011;59:7824–39.
[309] Jones RL, Conrad H. Effect of grain size on strength of alpha-titanium at room temperature. Trans Metall Soc AIME 1969;245:779–89.
[310] Holden FC, Ogden HR, Jaffee RI. Microstructure and mechanical properties of iodide titanium. Trans Am Inst Min Metall Eng 1953;197:238–42.

[311] Luo P, McDonald DT, Xu W, Palanisamy S, Dargusch MS, Xia K. A modified Hall-Petch relationship in ultrafine-grained titanium recycled from chips by equal channel angular pressing. Scr Mater 2012;66:785–8.
[312] Wang CT, Gao N, Gee MG, Wood RJK, Langdon TG. Effect of grain size on the micro-tribological behavior of pure titanium processed by high-pressure torsion. Wear 2012;280–281:28–35.
[313] Stolyarov VV, Zhu YT, Alexandrov IV, Lowe TC, Valiev RZ. Influence of ECAP routes on the microstructure and properties of pure Ti. Mater Sci Eng A 2001; 299:59–67.
[314] Figueiredo RB, de C.Barbosa ER, Zhao X, Yang X, Liu X, Cetlin PR, et al. Improving the fatigue behavior of dental implants through processing commercial purity titanium by equal-channel angular pressing. Mater Sci Eng A 2014;619:312–8.
[315] Lindley TG, Smallman RE. The plastic deformation of polycrystalline vanadium at low temperatures. Acta Metall 1963;11:361–71.
[316] Chun YB, Ahn SH, Shin DH, Hwang SK. Combined effects of grain size and recrystallization on the tensile properties of cryorolled pure vanadium. Mater Sci Eng A 2009;508:253–8.
[317] Nouet G, Deschanvres A. Relations entre les essais de dureté et de traction et la taille des grains dans le vanadium. J Less Common Metals 1974;35:17–29.
[318] Sherman DH, Owen CV, Scott TE. Effect of hydrogen on structure and properties of vanadium. Trans Metall Soc AIME 1968;242:1775–84.
[319] Sherman MA, Bunshah RF. Yield strength of fine-grained vanadium produced by high-rate physical vapor deposition. J Nucl Mater 1975;57:151–4.
[320] Wei Q, Jiao T, Ramesh KT, Ma E. Nano-structured vanadium: processing and mechanical properties under quasi-static and dynamic compression. Scr Mater 2004;50:359–64.
[321] Vashi UK, Armstrong RW, Zima GE. The hardness and grain size of consolidated fine tungsten powder. Metall Trans 1970;1:1769–71.
[322] Meieran ES, Thomas DA. Structure of drawn and annealed tungsten wire. Trans Metall Soc AIME 1965;233:937–43.
[323] Wei Q, Ramesh KT, Ma E, Kesckes LJ, Dowding RJ, Kazykhanov VU, et al. Plastic flow localization in bulk tungsten with ultrafine microstructure. Appl Phys Lett 2005;86:101907.
[324] Wei Q, Zhang HT, Schuster BE, Ramesh KT, Valiev RZ, Kecskes LJ, et al. Microstructure and mechanical properties of super-strong nanocrystalline tungsten processed by high-pressure torsion. Acta Mater 2006;54:4079–89.
[325] Mueller H, Haessner F. Influence of grain size and texture on the flow stress of zinc. Scr Metall 1981;15:487–92.
[326] Chmelík F, Trojanová Z, Lukáč P, Převorovský Z. Acoustic emission from zinc deformed at room temperature Part II The influence of grain size on deformation behaviour and acoustic emission of pure zinc. J Mater Sci Lett 1993;12:1166–8.
[327] Dusek P, Lukac P. Deformation of zinc polycrystals at room-temperature. Kovove Mater-Metall Mater 1979;17:538–45.
[328] Kawasaki M, Ahn B, Langdon TG. Microstructural evolution in a two-phase alloy processed by high-pressure torsion. Acta Mater 2010;58:919–30.
[329] Lukac P, Malek P. Effect of temperature on the deformation-behavior of a superplastic zinc alloy. Czech J Phys 1981;31:228–30.
[330] Abson DJ, Jonas JJ. Substructure strengthening in zirconium and zirconium-tin alloys. J Nucl Mater 1972;42:73–85.
[331] Ramani SV, Rodriguez P. Grain size dependence of the deformation behaviour of alpha zirconium. Can Metall Q 1972;11:61–7.
[332] Coleman CE, Hardie D. Grain-size-dependence in flow and fracture of alpha-zirconium. J Inst Met 1966;94:387–97.
[333] Jiang L, Pérez-Prado MT, Gruber PA, Arzt E, Ruano OA, Kassner ME. Texture, microstructure and mechanical properties of equiaxed ultrafine-grained Zr fabricated by accumulative roll bonding. Acta Mater 2008;56:1228–42.
[334] Podolskiy AV, Bonarski BJ, Setman D, Mangler C, Schafler E, Tabachnikova ED, et al. Microstructure and properties of nanostructured zirconium processed by high pressure torsion. Mater Sci Forum 2011;667–669:433–8.
[335] Edalati K, Horita Z, Yagi S, Matsubara E. Allotropic phase transformation of pure zirconium by high-pressure torsion. Mater Sci Eng A 2009;523:277–81.
[336] Tegart WJM. Tensile properties of polycrystalline cadmium and some cadmium alloys in range - 196 to 200 degrees C. J Inst Met 1962;91:99–104.
[337] Mannan SL, Rodriguez P. Grain size dependence of the deformation behaviour of cadmium. Acta Metall 1975;23:221–8.
[338] Zou D-I, He L-f, Xiao D-w, Zhao Y-w, Qiu Z-c, Lu C, et al. Microstructure and mechanical properties of fine grained uranium prepared by ECAP and subsequent intermediate heat treatment. Trans Nonferrous Metals Soc China 2020;30:2749–56.
[339] Otto F, Dlouhý A, Somsen C, Bei H, Eggeler G, George EP. The influences of temperature and microstructure on the tensile properties of a CoCrFeMnNi high-entropy alloy. Acta Mater 2013;61:5743–55.
[340] Gali A, George EP. Tensile properties of high- and medium-entropy alloys. Intermetallics 2013;39:74–8.
[341] Gludovatz B, Hohenwarter A, Catoor D, Chang EH, George EP, Ritchie RO. A fracture-resistant high-entropy alloy for cryogenic applications. Science 2014;345: 1153–8.
[342] Schuh B, Mendez-Martin F, Völker B, George EP, Clemens H, Pippan R, et al. Mechanical properties, microstructure and thermal stability of a nanocrystalline CoCrFeMnNi high-entropy alloy after severe plastic deformation. Acta Mater 2015;96:258–68.
[343] Sun SJ, Tian YZ, Lin HR, Dong XG, Wang YH, Wang ZJ, et al. Temperature dependence of the Hall-Petch relationship in CoCrFeMnNi high-entropy alloy. J Alloy Compd 2019;806:992–8.
[344] Sun SJ, Tian YZ, Lin HR, Yang HJ, Dong XG, Wang YH, et al. Achieving high ductility in the 1.7 GPa grade CoCrFeMnNi high-entropy alloy at 77 K. Mater Sci Eng A 2019;740–741:336–41.
[345] Sun SJ, Tian YZ, Lin HR, Dong XG, Wang YH, Zhang ZJ, et al. Enhanced strength and ductility of bulk CoCrFeMnNi high entropy alloy having fully recrystallized ultrafine-grained structure. Mater Des 2017;133:122–7.
[346] Laplanche G, Bonneville J, Varvenne C, Curtin WA, George EP. Thermal activation parameters of plastic flow reveal deformation mechanisms in the CrMnFeCoNi high-entropy alloy. Acta Mater 2018;143:257–64.
[347] Zherebtsov S, Stepanov N, Ivanisenko Y, Shaysultanov D, Yurchenko N, Klimova M, et al. Evolution of microstructure and mechanical properties of a CoCrFeMnNi high-entropy alloy during high-pressure torsion at room and cryogenic temperatures. Metals. 2018;8:123.
[348] Han Z, Ren W, Yang J, Du Y, Wei R, Zhang C, et al. The deformation behavior and strain rate sensitivity of ultra-fine grained CoNiFeCrMn high-entropy alloys at temperatures ranging from 77 K to 573 K. J Alloy Compd 2019;791:962–70.
[349] Kilmametov A, Kulagin R, Mazilkin A, Seils S, Boll T, Heilmaier M, et al. High-pressure torsion driven mechanical alloying of CoCrFeMnNi high entropy alloy. Scr Mater 2019;158:29–33.
[350] Soares GC, Patnamsetty M, Peura P, Hokka M. Effects of adiabatic heating and strain rate on the dynamic response of a CoCrFeMnNi high-entropy alloy. J Dyn Behav Mater 2019;5:320–30.
[351] Shabani M, Indeck J, Hazeli K, Jablonski PD, Pataky GJ. Effect of strain rate on the tensile behavior of CoCrFeNi and CoCrFeMnNi high-entropy alloys. J Mater Eng Perform 2019;28:4348–56.
[352] Liu G, Lu DH, Liu XW, Liu FC, Yang Q, Du H, et al. Solute segregation effect on grain boundary migration and Hall-Petch relationship in CrMnFeCoNi high-entropy alloy. Mater Sci Technol 2019;35:500–8.
[353] Lugon LP, Figueiredo RB, Cetlin PR. Tensile behavior of an eutectic Pb-Sn alloy processed by ECAP and rolling. J Mater Res Technol 2014;3:327–30.
[354] Ha TK, Chang YW. Effects of Temperature and Microstructure on the Superplasticity in Microduplex Pb-Sn Alloys. Mater Sci Forum 2001;357–359:159–64.
[355] Furukawa M, Horita Z, Nemoto M, Valiev RZ, Langdon TG. Microhardness measurements and the Hall-Petch relationship in an Al-Mg alloy with submicrometer grain size. Acta Mater 1996;44:4619–29.
[356] Hayes JS, Keyte R, Prangnell PB. Effect of grain size on tensile behaviour of a submicron grained Al–3 wt-%Mg alloy produced by severe deformation. Mater Sci Technol 2000;16:1259–63.
[357] Valiev RZ, Chmelik F, Bordeaux F, Kapelski G, Baudelet B. The Hall-Petch relation in submicro-grained Al-1.5% Mg alloy. Scr Metall Mater 1992;27:855–60.
[358] Youssef KM, Scattergood RO, Murty KL, Koch CC. Nanocrystalline Al–Mg alloy with ultrahigh strength and good ductility. Scr Mater 2006;54:251–6.
[359] Razavi SM, Foley DC, Karaman I, Hartwig KT, Duygulu O, Kecskes LJ, et al. Effect of grain size on prismatic slip in Mg–3Al–1Zn alloy. Scr Mater 2012;67: 439–42.
[360] Yuan W, Mishra RS, Carlson B, Mishra RK, Verma R, Kubic R. Effect of texture on the mechanical behavior of ultrafine grained magnesium alloy. Scr Mater 2011;64:580–3.

[361] Straska J, Janecek M, Gubicza J, Krajnak T, Yoon EY, Kim HS. Evolution of microstructure and hardness in AZ31 alloy processed by high pressure torsion. Mater Sci Eng A 2015;625:98–106.
[362] Zhou H, Hu L, Sun Y, Zhang H, Duan C, Yu H. Synthesis of nanocrystalline AZ31 magnesium alloy with titanium addition by mechanical milling. Mater Charact 2016;113:108–16.
[363] Silva CLP, Soares RB, Pereira PHR, Figueiredo RB, Lins VFC, Langdon TG. The Effect of High-Pressure Torsion on Microstructure, Hardness and Corrosion Behavior for Pure Magnesium and Different Magnesium Alloys. Adv Eng Mater 2019;21:1801081.
[364] Zhan MY, Li YY, Chen WP, Chen WD. Microstructure and mechanical properties of Mg–Al–Zn alloy sheets severely deformed by accumulative roll-bonding. J Mater Sci 2007;42:9256–61.
[365] Xia K, Wang JT, Wu X, Chen G, Gurvan M. Equal channel angular pressing of magnesium alloy AZ31. Mater Sci Eng A 2005;410–411:324–7.
[366] Guan D, Rainforth WM, Sharp J, Gao J, Todd I. On the use of cryomilling and spark plasma sintering to achieve high strength in a magnesium alloy. J Alloy Compd 2016;688:1141–50.
[367] del Valle JA, Carreño F, Ruano OA. Influence of texture and grain size on work hardening and ductility in magnesium-based alloys processed by ECAP and rolling. Acta Mater 2006;54:4247–59.
[368] Zhang ZJ, Duan QQ, An XH, Wu SD, Yang G, Zhang ZF. Microstructure and mechanical properties of Cu and Cu–Zn alloys produced by equal channel angular pressing. Mater Sci Eng A 2011;528:4259–67.
[369] An XH, Lin QY, Wu SD, Zhang ZF, Figueiredo RB, Gao N, et al. Significance of stacking fault energy on microstructural evolution in Cu and Cu-Al alloys processed by high-pressure torsion. Phil Mag 2011;91:3307–26.
[370] Jiang L, Fu H, Zhang H, Xie J. Physical mechanism interpretation of polycrystalline metals' yield strength via a data-driven method: A novel Hall-Petch relationship. Acta Mater 2022;231:117868.
[371] Koizumi T, Kuroda M. Grain size effects in aluminum processed by severe plastic deformation. Mater Sci Eng A 2018;710:300–8.
[372] Miura S, Ono N, Nishimura Y. Hall-Petch Relation and Twin Boundaries in Pure Copper and Cu-Al Alloys. J Soc Mater Sci, Jpn 2009;58:865–72.
[373] Hull D, Mogford IL. Ductile-brittle transition in steels irradiated with neutrons. Philos Mag: J Theor Exp Appl Phys 1958;3:1213–22.
[374] Tan C, Zhou K, Ma W, Attard B, Zhang P, Kuang T. Selective laser melting of high-performance pure tungsten: parameter design, densification behavior and mechanical properties. Sci Technol Adv Mater 2018;19:370–80.
[375] Risebrough NR, Teghtsoonian E. The linear hardening of cadmium. Can J Phys 1967;45:591–605.
[376] Yuan W, Panigrahi SK, Su JQ, Mishra RS. Influence of grain size and texture on Hall-Petch relationship for a magnesium alloy. Scr Mater 2011;65:994–7.
[377] Gong J, Benjamin Britton T, Cuddihy MA, Dunne FPE, Wilkinson AJ. ⟨a⟩ Prismatic, ⟨a⟩ basal, and ⟨c+a⟩ slip strengths of commercially pure Zr by micro-cantilever tests. Acta Mater 2015;96:249–57.
[378] Vo NQ, Averback RS, Bellon P, Caro A. Limits of hardness at the nanoscale: Molecular dynamics simulations. Phys Rev B 2008;78:241402.
[379] Kadau K, Lomdahl PS, Holian BL, Germann TC, Kadau D, Entel P, et al. Molecular-dynamics study of mechanical deformation in nano-crystalline aluminum. Metall Mater Trans A 2004;35:2719–23.
[380] Xu W, Dávila LP. Tensile nanomechanics and the Hall-Petch effect in nanocrystalline aluminium. Mater Sci Eng A 2018;710:413–8.
[381] Li YJ, Zeng XH, Blum W. Transition from strengthening to softening by grain boundaries in ultrafine-grained Cu. Acta Mater 2004;52:5009–18.
[382] May J, Höppel HW, Göken M. Strain rate sensitivity of ultrafine-grained aluminium processed by severe plastic deformation. Scr Mater 2005;53:189–94.
[383] Mueller J, Durst K, Amberger D, Göken M. Local Investigations of the Mechanical Properties of Ultrafine Grained Metals by Nanoindentations. Mater Sci Forum 2006;503–504:31–6.
[384] Kawasaki M, Ahn B, Kumar P, Jang J, Langdon TG. Nano- and micro-mechanical properties of ultrafine-grained materials processed by severe plastic deformation techniques. Adv Eng Mater 2017;19:1600578.
[385] Miyamoto H, Ota K, Mimaki T. Viscous nature of deformation of ultra-fine grain aluminum processed by equal-channel angular pressing. Scr Mater 2006;54:1721–5.
[386] Höppel HW, May J, Göken M. Enhanced strength and ductility in ultrafine-grained aluminium produced by accumulative roll bonding. Adv Eng Mater 2004;6:781–4.
[387] Kim H-W, Kang S-B, Tsuji N, Minamino Y. Elongation increase in ultra-fine grained Al–Fe–Si alloy sheets. Acta Mater 2005;53:1737–49.
[388] Ma ZY, Liu FC, Mishra RS. Superplastic deformation mechanism of an ultrafine-grained aluminum alloy produced by friction stir processing. Acta Mater 2010;58:4693–704.
[389] Maier V, Merle B, Göken M, Durst K. An improved long-term nanoindentation creep testing approach for studying the local deformation processes in nanocrystalline metals at room and elevated temperatures. J Mater Res 2013;28:1177–88.
[390] Maier V, Durst K, Mueller J, Backes B, Höppel HW, Göken M. Nanoindentation strain-rate jump tests for determining the local strain-rate sensitivity in nanocrystalline Ni and ultrafine-grained Al. J Mater Res 2011;26:1421–30.
[391] Ruppert M, Böhm W, Nguyen H, Höppel HW, Merklein M, Göken M. Influence of upscaling accumulative roll bonding on the homogeneity and mechanical properties of AA1050A. J Mater Sci 2013;48:8377–85.
[392] Böhner A, Maier V, Durst K, Höppel HW, Göken M. Macro- and nanomechanical properties and strain rate sensitivity of accumulative roll bonded and equal channel angular pressed ultrafine-grained materials. Adv Eng Mater 2011;13:251–5.
[393] Chinh NQ, Csanádi T, Győri T, Valiev RZ, Straumal BB, Kawasaki M, et al. Strain rate sensitivity studies in an ultrafine-grained Al–30wt.% Zn alloy using micro- and nanoindentation. Mater Sci Eng A 2012;543:117–20.
[394] Wang M, Shan A. Effect of strain rate on the tensile behavior of ultra-fine grained pure aluminum. J Alloy Compd 2008;455:L10–4.
[395] Dalla Torre FH, Pereloma EV, Davies CHJ. Strain hardening behaviour and deformation kinetics of Cu deformed by equal channel angular extrusion from 1 to 16 passes. Acta Mater 2006;54:1135–46.
[396] Wei Q, Cheng S, Ramesh KT, Ma E. Effect of nanocrystalline and ultrafine grain sizes on the strain rate sensitivity and activation volume: fcc versus bcc metals. Mater Sci Eng A 2004;381:71–9.
[397] Lu L, Li SX, Lu K. An abnormal strain rate effect on tensile behavior in nanocrystalline copper. Scr Mater 2001;45:1163–9.
[398] Gray GT, Lowe TC, Cady CM, Valiev RZ, Aleksandrov IV. Influence of strain rate & temperature on the mechanical response of ultrafine-grained Cu, Ni, and Al-4Cu-0.5Zr. Nanostruct Mater 1997;9:477–80.
[399] Li YJ, Blum W. Strain rate sensitivity of Cu after severe plastic deformation by multiple compression. Phys Status Solidi (a) 2005;202:R119–21.
[400] Cheng S, Ma E, Wang YM, Kecskes LJ, Youssef KM, Koch CC, et al. Tensile properties of in situ consolidated nanocrystalline Cu. Acta Mater 2005;53:1521–33.
[401] Lu L, Schwaiger R, Shan ZW, Dao M, Lu K, Suresh S. Nano-sized twins induce high rate sensitivity of flow stress in pure copper. Acta Mater 2005;53:2169–79.
[402] Alawadhi MY, Sabbaghianrad S, Huang Y, Langdon TG. Evaluating the paradox of strength and ductility in ultrafine-grained oxygen-free copper processed by ECAP at room temperature. Mater Sci Eng A 2021;802:140546.
[403] Wang YM, Hamza AV, Ma E. Temperature-dependent strain rate sensitivity and activation volume of nanocrystalline Ni. Acta Mater 2006;54:2715–26.
[404] Maier-Kiener V, Schuh B, George EP, Clemens H, Hohenwarter A. Insights into the deformation behavior of the CrMnFeCoNi high-entropy alloy revealed by elevated temperature nanoindentation. J Mater Res 2017;32:2658–67.
[405] Duhamel C, Brechet Y, Champion Y. Activation volume and deviation from Cottrell-Stokes law at small grain size. Int J Plast 2010;26:747–57.
[406] Wei Q. Strain rate effects in the ultrafine grain and nanocrystalline regimes—influence on some constitutive responses. J Mater Sci 2007;42:1709–27.
[407] Conrad H, Jung K. On the strain rate sensitivity of the flow stress of ultrafine-grained Cu processed by equal channel angular extrusion (ECAE). Scr Mater 2005;53:581–4.
[408] Lee D-H, Choi I-C, Yang G, Lu Z, Kawasaki M, Ramamurty U, et al. Activation energy for plastic flow in nanocrystalline CoCrFeMnNi high-entropy alloy: A high temperature nanoindentation study. Scr Mater 2018;156:129–33.
[409] Pan D, Nieh TG, Chen MW. Strengthening and softening of nanocrystalline nickel during multistep nanoindentation. Appl Phys Lett 2006;88:161922.

[410] Vehoff H, Lemaire D, Schüler K, Waschkies T, Yang B. The effect of grain size on strain rate sensitivity and activation volume – from nano to ufg nickel. Int J Mater Res 2007;98:259–68.
[411] Zhang XF, Fujita T, Pan D, Yu JS, Sakurai T, Chen MW. Influences of grain size and grain boundary segregation on mechanical behavior of nanocrystalline Ni. Mater Sci Eng A 2010;527:2297–304.
[412] Gu C, Lian J, Jiang Q, Jiang Z. Ductile–brittle–ductile transition in an electrodeposited 13 nanometer grain sized Ni–8.6wt.% Co alloy. Mater Sci Eng A 2007;459:75–81.
[413] Choi HJ, Lee SW, Park JS, Bae DH. Positive Deviation from a Hall-Petch Relation in Nanocrystalline Aluminum. Mater Trans 2009;50:640–3.
[414] Zhao Y, Wang X, Cao T, Han J-K, Kawasaki M, Jang J-i, et al. Effect of grain size on the strain rate sensitivity of CoCrFeNi high-entropy alloy. Mater Sci Eng A 2020;782:139281.
[415] Kocks UF, Argon AS, Ashby MF. Thermodynamics and Kinetics of Slip. Prog Mater Sci 1975;19:1–288.
[416] Mordike BL, Haasen P. The influence of temperature and strain rate on the flow stress of α-iron single crystals. Philos Mag: J Theor Exp Appl Phys 1962;7:459–74.
[417] Varvenne C, Leyson GPM, Ghazisaeidi M, Curtin WA. Solute strengthening in random alloys. Acta Mater 2017;124:660–83.
[418] Leyson GPM, Hector LG, Curtin WA. Solute strengthening from first principles and application to aluminum alloys. Acta Mater 2012;60:3873–84.
[419] Shahmir H, He J, Lu Z, Kawasaki M, Langdon TG. Evidence for superplasticity in a CoCrFeNiMn high-entropy alloy processed by high-pressure torsion. Mater Sci Eng A 2017;685:342–8.
[420] Xiao L, Huang P, Wang F. Inverse grain-size-dependent strain rate sensitivity of face-centered cubic high-entropy alloy. J Mater Sci Technol 2021;86:251–9.
[421] Moon J, Hong SI, Bae JW, Jang MJ, Yim D, Kim HS. On the strain rate-dependent deformation mechanism of CoCrFeMnNi high-entropy alloy at liquid nitrogen temperature. Mater Res Lett 2017;5:472–7.
[422] Wu Z, Gao Y, Bei H. Thermal activation mechanisms and Labusch-type strengthening analysis for a family of high-entropy and equiatomic solid-solution alloys. Acta Mater 2016;120:108–19.
[423] Spitzig WA, Keh AS. Orientation dependence of the strain-rate sensitivity and thermally activated flow in iron single crystals. Acta Metall 1970;18:1021–33.
[424] Allen NP, Hopkins BE, McLennan JE, Bullard EC. The tensile properties of single crystals of high-purity iron at temperatures from 100 to −253°C. Proc R Soc Lond Ser A: Math Phys Sci 1956;234:221–46.
[425] Steijn RP, Brick R. Flow and fracture of single crystals of high purity ferrite. Trans Am Soc Metals 1954;46:1406–48.
[426] Wei Q, Kecskes L, Jiao T, Hartwig KT, Ramesh KT, Ma E. Adiabatic shear banding in ultrafine-grained Fe processed by severe plastic deformation. Acta Mater 2004;52:1859–69.
[427] Jang D, Atzmon M. Grain-size dependence of plastic deformation in nanocrystalline Fe. J Appl Phys 2003;93:9282–6.
[428] Malow TR, Koch CC, Miraglia PQ, Murty KL. Compressive mechanical behavior of nanocrystalline Fe investigated with an automated ball indentation technique. Mater Sci Eng A 1998;252:36–43.
[429] Jia D, Ramesh KT, Ma E. Effects of nanocrystalline and ultrafine grain sizes on constitutive behavior and shear bands in iron. Acta Mater 2003;51:3495–509.
[430] Wei Q, Jiao T, Mathaudhu SN, Ma E, Hartwig KT, Ramesh KT. Microstructure and mechanical properties of tantalum after equal channel angular extrusion (ECAE). Mater Sci Eng A 2003;358:266–72.
[431] May J, Höppel HW, Göken M. Strain Rate Sensitivity of Ultrafine Grained FCC- and BCC-Type Metals. Mater Sci Forum 2006;503–504:781–6.
[432] Pereira PHR, Wang YC, Huang Y, Langdon TG. Influence of grain size on the flow properties of an Al-Mg-Sc alloy over seven orders of magnitude of strain rate. Mater Sci Eng A 2017;685:367–76.
[433] del Valle JA, Carreño F, Ruano OA. On the threshold stress for superplasticity in Mg–Al–Zn alloys. Scr Mater 2007;57:829–32.
[434] Takahashi H, Oishi Y, Wakamatsu K, Kawabe N. Tensile properties and bending formability of drawn magnesium alloy pipes. Mater Sci Forum 2003;419–422:345–8.
[435] Leyson GPM, Curtin WA, Hector LG, Woodward CF. Quantitative prediction of solute strengthening in aluminium alloys. Nat Mater 2010;9:750–5.
[436] Wang J, Horita Z, Furukawa M, Nemoto M, Tsenev NK, Valiev RZ, et al. An investigation of ductility and microstructural evolution in an Al−3% Mg alloy with submicron grain size. J Mater Res 1993;8:2810–8.
[437] Komura S, Horita Z, Furukawa M, Nemoto M, Langdon TG. An evaluation of the flow behavior during high strain rate superplasticity in an Al-Mg-Sc alloy. Metall Mater Trans A 2001;32:707–16.
[438] Musin F, Kaibyshev R, Motohashi Y, Itoh G. High strain rate superplasticity in a commercial Al–Mg–Sc alloy. Scr Mater 2004;50:511–6.
[439] Ishikawa H, Mohamed FA, Langdon TG. The influence of strain rate on ductility in the superplastic Zn–22% Al eutectoid. Philos Mag 1975;32:1269–71.
[440] Kumar P, Kawasaki M, Langdon TG. Review: Overcoming the paradox of strength and ductility in ultrafine-grained materials at low temperatures. J Mater Sci 2016;51:7–18.
[441] Mungole T, Kumar P, Kawasaki M, Langdon TG. A critical examination of the paradox of strength and ductility in ultrafine-grained metals. J Mater Res 2014;29:2534–46.
[442] Kumar P, Kawasaki M, Langdon TG. Resolving the strength-ductility paradox through severe plastic deformation of a cast Al-7% Si alloy. Mater Sci Forum 2017;879:1043–8.
[443] Hart EW. Theory of the tensile test. Acta Metall 1967;15:351–5.
[444] Woodford DA. Strain-rate sensitivity as a measure of ductility. Trans ASM. 1969;62:291–3.
[445] Langdon TG. The mechanical properties of superplastic materials. Metall Trans A 1982;13:689–701.
[446] Langdon TG. Seventy-five years of superplasticity: historic developments and new opportunities. J Mater Sci 2009;44:5998–6010.
[447] Dalla Torre F, Van Swygenhoven H, Schäublin R, Spätig P, Victoria M. Mechanical behaviour of nanocrystalline electrodeposited Ni above room temperature. Scr Mater 2005;53:23–7.
[448] Chan KC, Wang GF, Wang CL, Zhang KF. Low temperature and high strain rate superplasticity of the electrodeposited Ni/Si3N4(W) composite. Scr Mater 2005;53:1285–90.
[449] Park SS, You BS. Low-temperature superplasticity of extruded Mg–Sn–Al–Zn alloy. Scr Mater 2011;65:202–5.
[450] Neishi K, Horita Z, Langdon TG. Achieving superplasticity in ultrafine-grained copper: influence of Zn and Zr additions. Mater Sci Eng A 2003;352:129–35.
[451] Zhao YH, Bingert JF, Liao XZ, Cui BZ, Han K, Sergueeva AV, et al. Simultaneously increasing the ductility and strength of ultra-fine-grained pure copper. Adv Mater 2006;18:2949–53.
[452] Tanaka T, Higashi K. Superplasticity at room temperature in Zn-22Al alloy processed by equal-channel-angular extrusion. Mater Trans 2004;45:1261–5.
[453] Tanaka T, Kohzu M, Takigawa Y, Higashi K. Low cycle fatigue behavior of Zn–22mass%Al alloy exhibiting high-strain-rate superplasticity at room temperature. Scr Mater 2005;52:231–6.
[454] Wang T, Hu J, Du L-X, Sun G-S, Misra RDK. Strain rate and temperature dependence of low temperature superplastic deformation in a nanostructured microalloyed steel. Mater Lett 2019;243:165–8.
[455] Matsunoshita H, Edalati K, Furui M, Horita Z. Ultrafine-grained magnesium-lithium alloy processed by high-pressure torsion: low-temperature superplasticity and potential for hydroforming. Mater Sci Eng A 2015;640:443–8.
[456] Valiev RZ, Murashkin MY, Kilmametov A, Straumal B, Chinh NQ, Langdon TG. Unusual super-ductility at room temperature in an ultrafine-grained aluminum alloy. J Mater Sci 2010;45:4718–24.
[457] Figueiredo RB, Pereira PHR, Langdon TG. Low temperature superplasticity in ultrafine-grained AZ31 alloy. Defect Diffusion Forum 2018;385:59–64.
[458] Figueiredo RB, Langdon TG. Using high-pressure torsion to achieve superplasticity in an AZ91 magnesium alloy. Metals 2020;10:681.
[459] Figueiredo RB, Langdon TG. Achieving superplastic properties in a ZK10 magnesium alloy processed by equal-channel angular pressing. J Mater Res Technol 2016.
[460] Valiev RZ, Alexandrov IV, Zhu YT, Lowe TC. Paradox of strength and ductility in metals processed by severe plastic deformation. J Mater Res 2002;17:5–8.
[461] Lapovok R, Cottam R, Thomson PF, Estrin Y. Extraordinary superplastic ductility of magnesium alloy ZK60. J Mater Res 2005;20:1375–8.

[462] Figueiredo RB, Terzi S, Langdon TG. Using X-ray microtomography to evaluate cavity formation in a superplastic magnesium alloy processed by equal-channel angular pressing. Acta Mater 2010;58:5737–48.
[463] Figueiredo RB, Langdon TG. Record superplastic ductility in a magnesium alloy processed by equal-channel angular pressing. Adv Eng Mater 2008;10:37–40.
[464] Mabuchi M, Ameyama K, Iwasaki H, Higashi K. Low temperature superplasticity of AZ91 magnesium alloy with non-equilibrium grain boundaries. Acta Mater 1999;47:2047–57.
[465] Mabuchi M, Iwasaki H, Yanase K, Higashi K. Low temperature superplasticity in an AZ91 magnesium alloy processed by ECAE. Scr Mater 1997;36:681–6.
[466] Figueiredo RB, Pereira PHR, Langdon TG. Effect of numbers of turns of high-pressure torsion on the development of exceptional ductility in pure magnesium. Adv Eng Mater 2020;22:1900565.
[467] Nguyen N-T-C, Asghari-Rad P, Sathiyamoorthi P, Zargaran A, Lee CS, Kim HS. Ultrahigh high-strain-rate superplasticity in a nanostructured high-entropy alloy. Nature. Communications 2020;11:2736.
[468] Nene SS, Liu K, Sinha S, Frank M, Williams S, Mishra RS. Superplasticity in fine grained dual phase high entropy alloy. Materialia 2020;9:100521.
[469] Han J, Kang S-H, Lee S-J, Kawasaki M, Lee H-J, Ponge D, et al. Superplasticity in a lean Fe-Mn-Al steel. Nat Commun 2017;8:751.
[470] Figueiredo RB, Langdon TG. The development of superplastic ductilities and microstructural homogeneity in a magnesium ZK60 alloy processed by ECAP. Mater Sci Eng A 2006;430:151–6.
[471] McFadden SX, Zhilyaev AP, Mishra RS, Mukherjee AK. Observations of low-temperature superplasticity in electrodeposited ultrafine grained nickel. Mater Lett 2000;45:345–9.
[472] Bednarczyk W, Kawałko J, Wątroba M, Gao N, Starink MJ, Bała P, et al. Microstructure and mechanical properties of a Zn-0.5Cu alloy processed by high-pressure torsion. Mater Sci Eng: A 2020;776:139047.
[473] Prasad MJNV, Chokshi AH. Extraordinary high strain rate superplasticity in electrodeposited nano-nickel and alloys. Scr Mater 2010;63:136–9.
[474] McFadden SX, Mishra RS, Valiev RZ, Zhilyaev AP, Mukherjee AK. Low-temperature superplasticity in nanostructured nickel and metal alloys. Nature 1999;398:684–6.
[475] Bednarczyk W, Kawałko J, Wątroba M, Bała P. Achieving room temperature superplasticity in the Zn-0.5Cu alloy processed via equal channel angular pressing. Mater Sci Eng A 2018;723:126–33.
[476] Chapman JA, Wilson DU. The room-temperature ductility of fine-grain Magnesium. J Inst Met 1962–63;91:39–40.
[477] Somekawa H, Basha DA, Singh A. Room temperature grain boundary sliding behavior of fine-grained Mg-Mn alloys. Mater Sci Eng A 2018;730:355–62.
[478] Somekawa H, Singh A. Superior room temperature ductility of magnesium dilute binary alloy via grain boundary sliding. Scr Mater 2018;150:26–30.
[479] Zeng Z, Nie J-F, Xu S-W, H. J. Davies C, Birbilis N. Super-formable pure magnesium at room temperature. Nat Commun 2017;8:972.
[480] Mohammadi A, Enikeev NA, Murashkin MY, Arita M, Edalati K. Examination of inverse Hall-Petch relation in nanostructured aluminum alloys by ultra-severe plastic deformation. J Mater Sci Technol 2021;91:78–89.
[481] Yoshida S, Bhattacharjee T, Bai Y, Tsuji N. Friction stress and Hall-Petch relationship in CoCrNi equi-atomic medium entropy alloy processed by severe plastic deformation and subsequent annealing. Scr Mater 2017;134:33–6.
[482] Dangwal S, Edalati K, Valiev RZ, Langdon TG. Breaks in the Hall-Petch relationship after severe plastic deformation of magnesium, aluminum, copper, and iron. Crystals 2023;13:413.
[483] Panda S, Toth LS, Zou JX, Grosdidier T. Effect of strain heterogeneities on microstructure, texture, hardness, and H-activation of high-pressure torsion mg consolidated from different powders. Materials 2018;11:1335.
[484] Gleiter H. Grain boundaries as point defect sources or sinks—Diffusional creep. Acta Metall 1979;27:187–92.
[485] Cai B, Kong QP, Lu L, Lu K. Low temperature creep of nanocrystalline pure copper. Mater Sci Eng: A 2000;286:188–92.
[486] Li YJ, Blum W, Breutinger F. Does nanocrystalline Cu deform by Coble creep near room temperature? Mater Sci Eng A 2004;387–389:585–9.
[487] Kral P, Dvorak J, Sklenicka V, Langdon TG. The Characteristics of Creep in Metallic Materials Processed by Severe Plastic Deformation. Mater Trans 2019;60:1506–17.
[488] Reddy SR, Bapari S, Bhattacharjee PP, Chokshi AH. Superplastic-like flow in a fine-grained equiatomic CoCrFeMnNi high-entropy alloy. Mater Res Lett 2017;5:408–14.
[489] Shei S-A, Langdon TG. The mechanical properties of a superplastic quasi-single phase copper alloy. Acta Metall 1978;26:639–46.
[490] Watanabe H, Fukusumi M. Mechanical properties and texture of a superplastically deformed AZ31 magnesium alloy. Mater Sci Eng A 2008;477:153–61.
[491] Olguín-González ML, Hernández-Silva D, García-Bernal MA, Sauce-Rangel VM. Hot deformation behavior of hot-rolled AZ31 and AZ61 magnesium alloys. Mater Sci Eng A 2014;597:82–8.
[492] Watanabe H, Tsutsui H, Mukai T, Kohzu M, Tanabe S, Higashi K. Deformation mechanism in a coarse-grained Mg–Al–Zn alloy at elevated temperatures. Int J Plast 2001;17:387–97.
[493] Curtin WA, Olmsted DL, Hector LG. A predictive mechanism for dynamic strain ageing in aluminium–magnesium alloys. Nat Mater 2006;5:875–80.
[494] George EP, Curtin WA, Tasan CC. High entropy alloys: A focused review of mechanical properties and deformation mechanisms. Acta Mater 2020;188:435–74.
[495] Coury FG, Clarke KD, Kiminami CS, Kaufman MJ, Clarke AJ. High throughput discovery and design of strong multicomponent metallic solid solutions. Sci Rep 2018;8:8600.
[496] Toda-Caraballo I. A general formulation for solid solution hardening effect in multicomponent alloys. Scr Mater 2017;127:113–7.